

UNIVERSIDAD TECNICA
FEDERICO SANTA MARIA

Wide operation range DC-DC converter for electric vehicle charger

Tesis de grado presentada por
Alvaro Daniel Pesántez Alvarado
como requisito parcial para optar al grado de
Doctor en Ingeniería Electrónica

Profesor Guía
Dr. Samir Kouro Renaer

Agosto, 2024, Valparaíso, Chile

RESUMEN

CADA vez es más común el uso y desarrollo de vehículos eléctricos (EV), principalmente debido a que estos son considerados como la principal alternativa para reemplazar a los vehículos convencionales de combustión interna tradicionalmente empleados. El avance en las tecnologías de EV, especialmente en el campo de las baterías, ha generado nuevas necesidades relacionadas con los cargadores. Existen varias arquitecturas de sistemas de carga, que pueden clasificarse según la ubicación de los componentes del cargador. Los sistemas a bordo se caracterizan por tener los componentes dentro del EV, mientras que los cargadores fuera de bordo tienen todos sus componentes fuera del EV. Esta propiedad permite que las limitaciones de tamaño y peso no sean un problema al alcanzar altos valores de potencia, lo que permite menores tiempos de carga. Dentro de los sistemas de carga fuera de bordo se han estudiado varias topologías, destacándose por un lado las que presentan aislación galvánica mediante un transformador de baja frecuencia y, por otro, las que usan un transformador de alta frecuencia dentro de un convertidor DC-DC. Esta tesis presenta un análisis de posibles opciones de convertidores DC-DC sin aislación galvánica basados en el concepto de convertidores de potencia parcial. Este tipo de convertidores permiten dividir la potencia total que se inyecta a la batería en una parte procesada por el convertidor y otra que se inyecta directamente a la batería. Sobre este tipo de convertidores, y aprovechando la presencia de una etapa previa de aislación en baja o alta frecuencia, se analizan mediante pruebas experimentales y de simulación dos topologías que reemplazan el uso de transformadores de alta frecuencia por una red de impedancia, también conocidas como enlaces AC. Estas topologías son opciones válidas para ser usadas como convertidores DC-DC dentro de una estación de carga, permitiendo además obtener un amplio rango de voltaje en su salida para adaptarse a las diferentes configuraciones de voltaje en las baterías existentes.

Palabras Claves

- Cargador rápido
- Convertidor DC-DC

- Convertidores de potencia parcial
- Red de impedancia
- Vehículo eléctrico

ABSTRACT

THE use and development of electric vehicles (EV) is becoming increasingly common, mainly because they are considered the primary alternative to replace traditionally used internal combustion vehicles. Advances in EV technologies, especially in the field of batteries, have created new needs related to chargers. There are several charging system architectures, which can be classified according to the location of the charger components. On-board systems are characterized by having the components within the EV, while off-board chargers have all their components outside the EV. This property allows size and weight limitations to not be an issue when achieving high power values, thus allowing shorter charging times.

Within off-board charging systems, several topologies have been studied, with notable examples including those that present galvanic isolation through a low-frequency transformer and those that use a high-frequency transformer within a DC-DC converter. This thesis presents an analysis of possible DC-DC converter options without galvanic isolation based on the concept of partial power converters. These converters allow dividing the total power injected into the battery into a part processed by the converter and another part that is injected directly into the battery.

Focusing on these converters and taking advantage of a prior isolation stage, whether in low or high frequency, two topologies are analyzed through experimental and simulation tests. These topologies replace the use of high-frequency transformers with an impedance network, also known as AC links. These topologies are valid options to be used as DC-DC converters within a charging station, also allowing for a wide voltage range at their output to adapt to different battery voltage configurations.

Keywords

- DC-DC converter
- Electric vehicle
- Fast charger
- Impedance network

- Partial power converters

ACKNOWLEDGMENTS

ESTE largo proceso de formación finalmente concluye , y es que todo este fuerzo y horas de dedicación hubiese sido imposible si no contara con todo el apoyo y la ayuda de todas las personas que siempre estuvieron conmigo. Es por esto que en este pequeño espacio aprovecho para agradecer en primer lugar a Jehová el creador de todo quien sin duda fue la mayor fuente de energía que me impulso en todo este camino, a mi amada esposa Daniela, quien con su paciencia, su calma y su amor no supo más que apoysarme y darme todas las fuerzas necesarias en los momentos buenos y malos de todo este proceso, agradezco a mis padres y hermanos quienes desde la distancia siempre estuvieron junto a mi dándome toda la ayuda el apoyo que requería y siendo los que siempre estuvieron para apoyarme de toda manera sin duda sin ustedes este trabajo hubiese sido imposible, agradezco también al Dr. Samir Kouro quien el profesor guía a lo largo de este camino compartiendo todos sus conocimientos y su don de persona, al Dr. Hugues Renaudineau por todo el soporte y dirección que le dio a este proyecto desde el principio hasta el fin del mismo, agredezco también al Dr. sebastián Rivera por su gran aporte a mi foramación. Finalmente a todo el grupo de compañeros y amigos que de varias formas lograron que esta experiencia haya tenido todo el sentido, muchas gracias a todos.

CONTENTS

RESUMEN i

ABSTRACT iii

ACKNOWLEDGMENTS v

LIST OF FIGURES viii

LIST OF TABLES xii

NOMENCLATURE xiii

LIST OF SYMBOLS xv

1 INTRODUCTION 1
- 1.1 Context, motivation and problem statement . . . 2
- 1.2 Hypothesis . . . 6
- 1.3 Objectives of the thesis . . . 6
  - 1.3.1 General objective . . . 6
  - 1.3.2 Specific objectives . . . 7
- 1.4 Contributions . . . 7
- 1.5 Outline of the thesis . . . 7

2 ELECTRIC VEHICLE BATTERY CHARGERS 9
- 2.1 On-board charging . . . 13
  - 2.1.1 Dedicated chargers . . . 14
  - 2.1.2 Integrated chargers . . . 19
- 2.2 Off-board charging . . . 21
  - 2.2.1 Off-board DC-fast charger configurations . . . 24
- 2.3 Charging standards . . . 26
- 2.4 Conclusion . . . 27

3 PROPOSED DC-DC STAGES FOR FAST CHARGERS 29
3.1 Introduction to partial power converters . . . 29
3.1.1 Classification . . . 30
3.1.2 Principal PPC architectures for EV chargers . . . 31
3.2 Proposed impedance network type I partial power converter . . . 33
3.2.1 Topology description . . . 34
3.2.2 Operation principle . . . 35
3.2.3 Converter modeling . . . 39
3.2.4 Partial power operation analysis . . . 42
3.3 Proposed wide output range buck-boost impedance network converter 43
3.3.1 Topology description . . . 44
3.3.2 Operation principle . . . 47
3.3.3 Converter modeling . . . 51
3.3.3.1 Buck mode . . . 52
3.3.3.2 Boost mode . . . 54
3.4 Conclusion . . . 55

4 SIMULATION RESULTS 56
4.1 Impedance network type I partial power converter . . . 56
4.1.1 Component sizing . . . 56
4.1.2 Control scheme . . . 58
4.1.2.1 Controllers design . . . 58
4.1.2.2 Stability analysis . . . 59
4.1.3 Simulation results . . . 62
4.2 Wide output range buck-boost impedance network converter . . . 66
4.2.1 Component sizing . . . 66
4.2.2 Control scheme . . . 68
4.2.3 Simulation results . . . 72
4.3 Conclusion . . . 76

5 EXPERIMENTAL RESULTS 77
5.1 Impedance network type I partial power converter . . . 77
5.2 Wide output range buck-boost impedance network converter . . . 81
5.3 Conclusion . . . 86

6 CONCLUSIONS 87

REFERENCES 90

List of Figures

1.1 Global greenhouse gas emissions by sector [1]. 1
1.2 Effect of the current reduction on the cross-section of the wire [2]. . 3
1.3 Simplified battery configurations systems for: a) 400 V; b) 800 V [2]. 4
1.4 Comparison of the charging time between 800 V systems at 250 kW and 400 V systems at 150kW, for a battery capacity of 60 kWh [2]. 4

2.1 Average energy losses from grid to battery for the tested SoC areas in BMW i3 [3]. 10
2.2 Classification of different structures for EV battery chargers [4]: a)Battery swapping; b) HF isolated off-board charger; c) LF isolated off-board charger; d) Wireless charger; e) On-board integrated charger; f) On-board dedicated charger. 11
2.3 Off-board configurations whit HF isolation architectures: a) With regulated HF isolation; b) With unregulated HF isolation and post-regulation. 13
2.4 EV power system and typical charging modes. 14
2.5 On-board charger: a) Unidirectional; b) Bidirectional. 15
2.6 Second-generation Chevrolet Volt on-board charger. 16
2.7 Unidirectional on-board charger cell rated 3.5 kW. 16
2.8 Matrix-type Hella converter. 17
2.9 Texas 6.6 kW bidirectional on-board charger. 17
2.10 Power pulsating buffer topology. 18
2.11 Hyundai On-board bi-directional converter. 18
2.12 Single-phase integrated on-board charger. 19
2.13 On-board charger fully integrated with 6-phase traction motor drives. 20
2.14 Nine-switch integrated on-board charger converter. 21
2.15 Integrated DC on-board charger. 21
2.16 Fast charging station architectures: a) AC-bus with LF isolation; b) AC-bus with HF isolation; c) DC-bus with HF isolation. . . . 23
2.17 LLC resonant HB with reconfigurable output converter for the ABB Terra 53/54 50 kW fast charger. 25

2.18 Modular PS FB DC-DC converter for the Tesla Supercharger V2. . 25
2.19 DC-DC 3-channel buck interleave converter for the ABB Terra HP 150 kW series. 26
2.20 Porsche modular fast charging park version A. 26
2.21 Porsche modular fast charging park version B. 27

3.1 Different PPCs architectures: a) IPOS step-up; b) ISOP step-down; c) ISOP step-u;. d) IPOS step-down. 30
3.2 General structure of an ideal PPC DC-DC regulation converter: a) Type I PPC; b) Type II PPC. 31
3.3 Partial power ratio converter of Type I and Type II PPC. . . . 32
3.4 Step-up PPC Type I topologies: a) FB topology with transformer; b) Proposed impendance network PPC. 34
3.5 Switching states: a) State I (Sa, Sc) = (1, 0); b) State II (Sa, Sc) = (1, 1); c) State III (Sa, Sc) = (0, 1); d) State IV (Sa, Sc) = (0, 0). . 35
3.6 Steady-state operation waveforms: a) S_a switching signal; b) S_c switching signal; c) S_a switch voltage; d) C_1 capacitor voltage; e) C_2 capacitor voltage; f) L_1 inductor voltage; g) L_1 inductor current; h) S_a MOSFET current; i) D_a diode curren;. j) Output converter current; k) Input and output converter voltages. 38
3.7 Gain of the proposed converter as a function of the phase shift α. . 41
3.8 Partial power operation in Type I and Type II PPCs for G_v in the range 1.5 - 2. 43
3.9 Proposed dual impedance network buck-boost DC-DC converter. . 44
3.10 Steady-state operation waveforms of the proposed converter in buck mode: a) S_a switching signal; b) S_b switching signal; c) V_o output voltage; d) L inductor current; e) C_1 capacitor voltage; f) C_1 capacitor current. 46
3.11 Steady-state operation waveforms of the proposed converter in boost mode: a) S_c switching signal; b) S_d switching signal; c) V_o output voltage; d) L inductor current; e) C_2 capacitor voltage; f) C_2 capacitor current. 47
3.12 Switching states: a) Buck mode state I (Sa, Sb, Sc, Sd) = (0, 0, 0, 0); b) Buck mode state II (Sa, Sb, Sc, Sd) = (0, 1, 0, 0); c) Buck mode state III (Sa, Sb, Sc, Sd) = (1, 0, 0, 0); d) Boost mode state I (Sa, Sb, Sc, Sd) = (1, 1, 0, 0); e) Boost mode state II (Sa, Sb, Sc, Sd) = (1, 1, 0, 1); f) Boost mode state III (Sa, Sb, Sc, Sd) = (1, 1, 1, 0). 49

4.1 Output inductor waveform 57
4.2 L1 inductor waveform 58
4.3 CC-CV control scheme. 58
4.4 Uncompensated close-loop $\Upsilon_u(s)$ Bode plot 61

4.5 Compensated close-loop $\Upsilon(s)$ Bode plot 62
4.6 Main simulated waveforms of the impedance network type I PPC: a) S_a switch voltage; b) S_c switch voltage; c) C_1 capacitor voltage; d)C_2 capacitor voltage; e) L_1 inductor current; f) L inductor current; g) Converter output voltage 63
4.7 Battery charging process for a 400 V system; a) Output voltage. b) Output current. 64
4.8 Battery charging process for a 800 V system; a) Output voltage. b) Output current. 65
4.9 Efficiency comparison between impedance network type I PPC (blue) and HF isolated type I PPC (red). 66
4.10 Waveform of the inductor converter 67
4.11 Control scheme for the wide range impedance network converter. . 68
4.12 Uncompensated close-loop $\Upsilon_{ubu}(s)$ bode plot. 69
4.13 Complete closed-loop transfer function Bode plot of the compensated system in buck operation mode. 70
4.14 Uncompensated close-loop $\Upsilon_{ubo}(s)$ bode plot. 71
4.15 Complete closed-loop transfer function Bode plot of the compensated system in boost operation mode. 72
4.16 Behavior of the converter in operating modes: a) Buck; b) Boost. . 73
4.17 Battery charging process for: a) LV battery configuration; b) HV battery configuration. 74
4.18 Estimated efficiency of the wide output range buck-boost impedance network converter. 75

5.1 Experimental setup for the impedance network type I PPC. . . . 77
5.2 Experimental validation of the transfer funcion of the type I impedance network converter. 79
5.3 Experimental results with resistive load and $\alpha = 0.5$: a) Ch1: Output voltage V_o, Ch2: Capacitor voltage V_{C_1}, Ch3: Output current i_L, Ch4: Input current i_{in}; b) Ch1: Output voltage V_o, Ch2: Impedance network inductor voltage V_{L_1}, Ch3: switch Sb drain-source voltage. . 79
5.4 Experimental results during battery charging cycle. Ch1: Output voltage V_o, Ch2: Impedance network capacitor voltage V_{C_1}, Ch3: switch S_b voltage, Ch4: Output current i_L. 80
5.5 Experimental measurements. a) Over 01 kW to 0.5 kW range; b) Measured input and output powers, voltages, currents, and global efficiency of the proposed PPC at 1.6 kW. 81
5.6 Experimental setup for the wide output range buck-boost impedance network converter. 82

5.7 Experimental validation of the wide output range buck-boost impedance network converter: a) Buck operation mode; b) Boost operation mode. 82
5.8 Experimental results for the boost operation mode. (a) Ch1: Output voltage V_o, Ch2: Switch S_c drain-source voltage, Ch3: Switch S_d drain-source voltage, Ch4: Capacitor voltage V_{C_2}; (b) Ch1: Output voltage V_o, Ch2: Output inductor current i_o, Ch3: Input inductor current i_L, Ch4: Capacitor voltage V_{C_2}. 83
5.9 Experimental efficiency measurement of the wide output range buck-boost impedance network converter, boost operation mode: a) Efficiency plot over a 0.5 kW power range; (b) Measured input and output powers, voltages, currents, and global efficiency of the converter at 0.5 kW. 84
5.10 Experimental results for the buck operation mode. Ch1: Output voltage V_o, Ch2: Output current i_L, Switch S_a drain-source voltage, Ch4: Capacitor voltage V_{C_1}. 85
5.11 Experimental efficiency measurement of the wide output range buck-boost impedance network converter, buck operation mode: a) Efficiency plot over a 0.1 kW to 0.5 kW power range; (b) Measured input and output powers, voltages, currents, and global efficiency of the converter at 0.4 kW. 86

List of Tables

1.1 Li-ion battery capacity, driving range and nominal voltage of some EVs on the market (data accessed within first semester 2024). . . 3

2.1 Specifications of commercial DC off-board fast chargers. 24
2.2 DC CHARGING STANDARDS [5] 28

3.1 Type I impedance network PPC switching states. 38
3.2 Wide output voltage range DC-DC converters. 44
3.3 Wide output range dual impedance network converter switching states. 51

4.1 Design parameters 60
4.2 Design parameters for wide range impedance network converter. . . 67

5.1 Experimental parameters for impedance network type I PPC. . . 78
5.2 Experimental parameters for wide output range buck-boost impedance network converter in boost operation mode. 82
5.3 Experimental parameters for wide output range buck-boost impedance network converter in buck operation mode. 85

NOMENCLATURE

Abbreviations

AC	Alternating Current
BMS	Battery Management System
CC	Constant Current
CCS	Combined Charge System
CV	Constant Voltage
DAB	Double Active Bridge
DC	Direct Current
DPC	Differential Power Converter
EMI	Electromagnetic Interference
EMI	Energy Storage Systems
EV	Electric Vehicle
FB	Full Bridge
HB	Half Bridge
HF	High Frequency
IOBC	Integrated On-board Charger
IPOS	Input-Parallel Output-Series
ISOP	Input-Series Output-Parallel
LF	Low Frequency
LV	Low Voltage
Li-ion	Ion-lithium
MF	Medium Frequency
MV	Medium Voltage
PFC	Power Factor Correction
PI	Proportional Integrator
PPC	Partial Power Converter
PPP	Partial Power Processing
PS	Phase-Shift
PSM	Phase Shift Modulation
PMSM	Permanent Magnet Synchronous Motor
PWM	Pulse Width Modulation

RHP	Right Hand Pole
SoC	State of Charge
SST	Solid State Transformer
ZCS	Zero Current Switching
ZVS	Zero Voltage Switching

LIST OF SYMBOLS

A	Exponential zone voltage amplitude	V
B	Exponential zone time constant	Ah^{-1}
C_1	First impedance network capacitor	mF
C_2	Second impedance network capacitor	mF
d	Duty cycle for the boost operation mode	–
D_a	Diode a of the outpur diode-bridge	–
D_b	Diode b of the outpur diode-bridge	–
D_c	Diode c of the outpur diode-bridge	–
D_a	Diode d of the outpur diode-bridge	–
E_o	Battery constant voltage	V
G_c	Compensator transfer function	–
G_{in}	Output to input transfer function	–
G_v	Global voltage gain	–
G_{vd}	Output to control transfer function	–
H	Sensor gain	–
i_{in}	Input current of the converter	A
i_L	Output inductor current	A
i_o	Output current of the converter	A
it	Actual battery charge	Ah
K_{ap}	Polarizing voltage	V
K_{pr}	Partial power ratio	%
L	Output inductor filter	mH
L_1	Impedance network inductor	mH
N	Transformer turn ratio	–
n_1	Number of turns of the low-voltage side of the transformer	–
n_1	Number of turns of the high-voltage side of the transformer	–

P_{bat}	Total power delivery to the battery	W
P_{dir}	Power direct to the battery	W
P_{in}	Input power of the converter	W
P_{pc}	Power of partial converter	W
Q	Battery capacity	Ah
R_{eq}	Equivalent output load	Ω
S_a	Semiconductor a of the impedance network converter	–
S_b	Semiconductor b of the impedance network converter	–
S_c	Semiconductor c of the impedance network converter	–
S_d	Semiconductor d of the impedance network converter	–
T	Close loop gain transfer function	–
T_u	uncompensated close loop gain transfer function	–
v_1	Voltage of the low-voltage side of the transformer	V
v_2	Voltage of the high-voltage side of the transformer	V
V_c	Voltage compensate signal	V
V_{C1}	Voltage in the C_1 capacitor of impedance network	V
V_{C2}	Voltage in the C_2 capacitor of impedance network	V
V_e	Voltage error signal	V
V_{in}	Input voltage of the converter	V
V_L	Output inductor voltage	V
V_M	Modulation signal amplitude	V
V_o	Output voltage of the converter	V
V_{pc}	Voltage in the partial power converter	V
V_{ref}	Voltage reference signal	V
$\hat{x}(t)$	Small disturbance added to the signal $X(t)$	–
$\bar{x}(t)$	Average value of $x(t)$ over a switching period T	–
Z_{iL}	Output to impedance transfer function	–
δ	Duty cycle for the buck operation mode	–
φ_m	Phase margin	$\circ$

Chapter 1

INTRODUCTION

HUMAN activity is the main reason for most environmental problems, principally due to greenhouse gas emissions. It is estimated that around 80% of the carbon dioxide present in the atmosphere is produced by the burning of fossil fuels [2, 6, 7]. In the world it is estimated that around 50 billion tonnes of greenhouse gases are emitted each year [1]; emissions come from many sectors: waste, industrial processes, energy, agriculture. Figure 1.1 shows the percentage of emissions according to each sector mentioned above.

The energy sector is the main responsible for the global greenhouse gas emissions with 73 % of the total. This percentage can be subdivided into sub-sectors: energy use the industry, buildings, transport and other energy uses. Transport includes all direct emissions from fossil fuels in transport activities like road transport, avi-

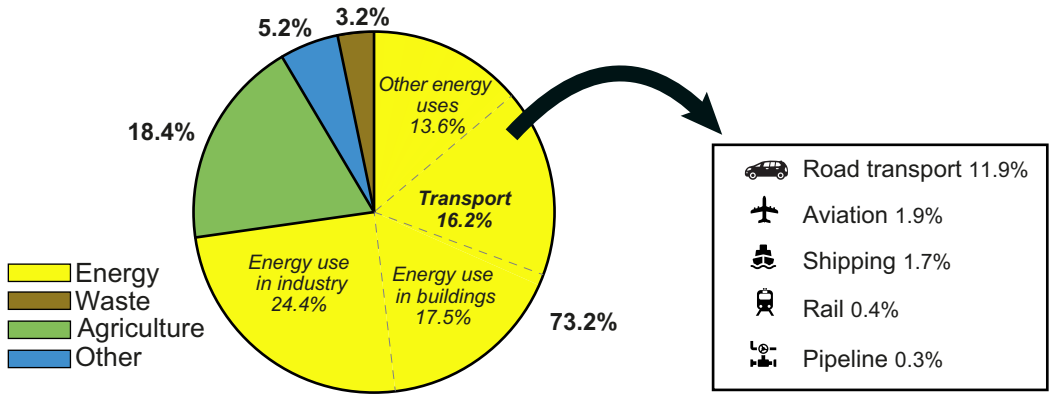

Figure 1.1: Global greenhouse gas emissions by sector [1].

ation, rail, pipeline, and shipping, as shown in Figure 1.1. It is precisely in the transport sector where electric vehicles (EV) technology has emerged as one of the most promising alternatives to replace conventional combustion engine vehicles [8,9].

One of the most critical components in moving towards electric transportation is the battery, which must be capable of supplying the energy (range and autonomy) and power (capabilities and performance) demands of the EV. The advancements in Ion-lithium (Li-ion) battery technology has made EVs the preferred choice among manufacturers, making them more cost-effective and functional in recent years. The price of Li-ion batteries has fallen by 89%, from more than $1100/kWh in 2010 to $133/kWh in 2023. By 2025, prices are expected to be close to $110/kWh [10–12]. However, battery degradation, charging rate limitations, and limited energy density still pose challenges to more widespread EV adoption [13].

1.1 Context, motivation and problem statement

Restricted driving range and lengthy battery charging times are the primary obstacles for the adoption of EVs by consumers [14]. Table 1.1 shows the capacity of the batteries and the driving range of some of the EVs on the market. For the the majority of the models, the battery energy capacity is usually between 60 kWh and 100 kWh. With a fast charging technology rated at 50 kW, it would take between 35 and 120 minutes to recharge the battery [15]. However, by increasing the charging power level to 150 kW, the charging time could be reduced by two-thirds.

Over the past decade, most EVs have used battery configurations in the range of 150 V to 450 V; this voltage configuration is often called the 400 V system. Increasing the charging power in fast chargers translates into higher current ratings, increasing the cable size, making both the charger and the power train of the EV bulkier. In addition, a more capable cooling system is required [15].

In order to offer potential savings in cable weight and an improvement in the power rating and charging times, the 800 V system has been proposed. For example, concerning the charging time, for a vehicle with 400 km driving range, it can be reduced from 29 minutes for the 400 V system to less than 15 minutes for the 800 V system [2].

In [2] an analysis of the effect of current reduction on the required cross-section of the wire is presented. For a constant power at a voltage level of 800 V and 400 V, the current required is reduced by half for the 800 V system compared to the 400 V system. Figure 1.2 shows how reducing the current reduces the cross-section of the wire.

Table 1.1: Li-ion battery capacity, driving range and nominal voltage of some EVs on the market (data accessed within first semester 2024).

EV Model	Range(km)	Capacity (kWh)	Voltage (V)
Chevrolet Bolt EV 2LT 2023	416	65	350
Audi Q4 e-tron50 2022	460	82	400
BMX iX M60 2024	563	111.5	330
Honda e:Ny1 2023	412	68.8	370
Mazda MX-30 2021	265	35.5	355
Tesla Model Y 2023	514	82.1	360
Kia EV6 2023	424	77.4	697
Mercedez AM6 EQS53 2022	583	107.8	500
Tesla Cybertruck 2024	556	123	816
Lucid Air Touring 2023	717	112	900
Porsche Macan 2024	784	100	800

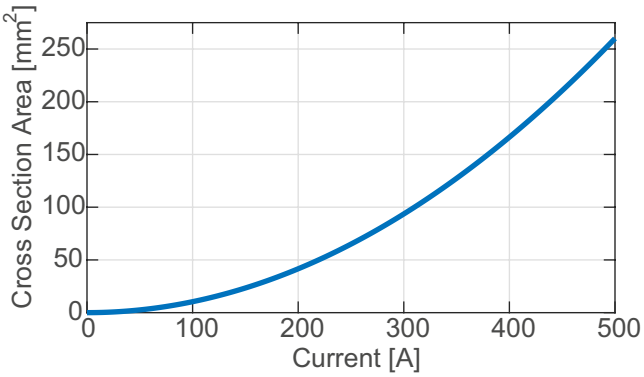

Figure 1.2: Effect of the current reduction on the cross-section of the wire [2].

EV batteries are made by the series and parallel connection of individual battery cells, to achieve the nominal characteristics for which they are designed. Each cell has a voltage value, which varies according to the technology used in its manufacture. For instance, a typical 60 kWh, Li-ion 400 V EV battery configuration comprises 400 cells, each with a nominal voltage of 3.7 V and a variation between 2.8 V to 4.2 V, distributed in four parallel-connected strings of 100 cells each. This results in a voltage range of 300 V to 420 V, as shown in 1.3 a). In order to upgrade to an 800 V system while keeping the EV battery pack energy capacity and the cell count constant, a rearrangement of the cell array is carried out. The 800 V system

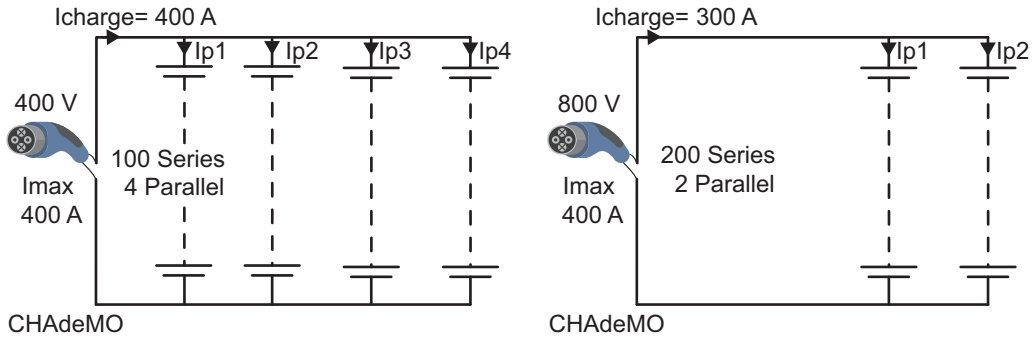

(a) (b)

Figure 1.3: Simplified battery configurations systems for: a) 400 V; b) 800 V [2].

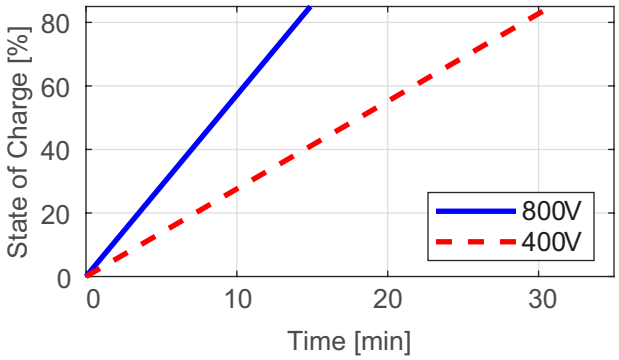

Figure 1.4: Comparison of the charging time between 800 V systems at 250 kW and 400 V systems at 150kW, for a battery capacity of 60 kWh [2].

involves configuring the EV battery with two sets of 200 series connected cells in parallel [15], as illustrated in Figure 1.3 b).

Considering a typical Li-ion cell maximum charge current rate of 150 A and voltage of 4.15 V per Li-ion cell, a 400 V system with 4-parallel and 100-series connected cells, as shown in Figure 1.3 a), results in a pack voltage of 415 V. To charge the cells to their maximum current range, and given the connection of four groups of cells in parallel, a charging current of 600 A would be necessary. However, the maximum charging current is limited by the charging standard; considering CHAdeMO, the limit will be 400 A [5], resulting in a 166 kW charging station, where the current that flows through the cells reach only 100 A.

On the other hand, with the 800 V system (2-parallel strings, 200-series cells), shown in Figure 1.3 b), the maximum current required to charge the battery pack is

300 A and the current is no longer limited by the standard but by the construction characteristics of the battery cells. Thus, the cells are charged at a higher current (150 A versus 100 A). The 800 V maximum voltage with the 300 A current rating results in a 250 kW charging station. Figure 1.4 shows a comparison between the 400 V and 800 V systems, where the charging time for each voltage system is appreciated. The time it takes for the battery to reach 80%, which is the traditional state of charge (SoC) level employed by manufacturers to test the charging time [3], of SoC is of 29 minutes for the 400 V systems, while 14 minutes for the 800 V system, due to the increase in the power of the charger. Based on all the advantages described for the 800 V systems, several manufacturers are developing their latest versions of EV with the 800 V system.

In some scenarios, the use of high-power chargers might not be feasible, especially for residential installations or locations where the property infrastructure or the local power grid cannot support them. In such cases, it is important to note that 400 V systems continue to stand as the mainstream solution in the EV market. In [15], a comprehensive analysis and comparison are conducted between the two types of systems, focusing on assessing their respective advantages and disadvantages. Therefore, the two systems coexist, making it necessary to have fast and efficient charging infrastructure capable of catering to both battery pack voltages. This can be evidenced by the companies specializing in EV development are continuously introducing new models that utilize different voltage levels for their batteries. Table 1.1 displays a range of battery pack voltages of the latest EV models. The initial section of the table features models operating at low voltage (LV), specifically within the 330 V-400 V range. In contrast, the latter part of Table 1.1 showcases vehicle models that operate at high voltage (HV), within the 500 V-900 V range.

The wide voltage range charging issue has been already addressed in literature. There are several types of chargers that allow charging 400 V and 800 V battery systems. For example, in [16] an reconfigurable converter topology for HV battery systems is propposed. Nevertheless, this converter functions by reconfiguring the battery and the battery management system (BMS), which makes it a costly and complex solution to deploy. In [17,18], solutions are presented that modify chargers designed for 400 V systems using a battery selection circuit. However, these topologies have a limited charging range that does not support batteries with nominal voltages significantly different from 400 V or 800 V, such as the Kia EV6 battery, shown in Table 1.1. In [19] another reconfigurable topolgy is proposed, this DC-DC converter is composed of an active full bridge (FB) connected to a high-frequency (HF) three winding transformer, the output voltage varies in the range of 250 V to 1000 V, however, the output voltage for this converter should be in the range between 640 V to 840 V. The work presented in [20] introduces a reconfigurable battery charger with a wide output range, whos key feature is its buck-boost topology

on the grid side, allowing for an output range from 120 V to 900 V. This converter is notable for providing a continuous voltage range at its output.

Another research trend in EV chargers is the use of partial power converters (PPC) for the DC-DC stage because of their high efficiency. One notable feature of these converters is their capacity to control only a fraction of the total power delivered to the battery, while the rest of the power is passed directly [21–23]. PPCs are classified mainly according to how they connect to the system. Various topologies exist, but for EV battery charging applications, the input-parallel output-series (IPOS) and input-series output-parallel (ISOP) topologies are of significant interest. The IPOS step-up topology is termed Type I PPC, whereas the ISOP step-down topology is designated as Type II PPC [24].

To the best of the authors knowledge, no research has been conducted on the application of PPC for wide range EV charging stations. Therefore, this thesis presents the following hypotheses.

1.2 Hypothesis

The following are the hypothesis that will guide the research work through this project.

1. *Substituting the HF transformer of a partial power converter with an impedance network will still preserving its partial capacity and effectively manage voltage and current regulation within the DC-DC stage of a fast charger.*

2. *Replacing a high-frequency transformer with an impedance network will enhance the overall efficiency of the system by reducing the transformer core and winding losses, thereby optimizing power transfer and minimizing energy dissipation.*

3. *A buck-boost converter with impedance network can achieve the necessary output voltage range to charge both 400 V and 800 V battery pack systems.*

1.3 Objectives of the thesis

1.3.1 General objective

Propose, analyze and develop a transformerless impedance network PPC for the DC-DC stage of an EV battery charger to increase EV charging efficiency and output voltage range.

1.3.2 Specific objectives

- Propose and analyze an impendance network DC-DC power converters based on the PPC concept to achieve an efficient charging process.
- Adapt suitable existing control and modulation strategies for the proposed converters.
- Modeling and simulation of the proposed converters and control systems.
- Design and construction of experimental prototypes.
- Experimental validation of theoretical and simulation results.
- Dissemination of results.

1.4 Contributions

The contributions of the thesis are listed as follows:

- Enhance the efficiency of the transformerless regulated DC-DC stage in a fast charging station by substantially decreasing the power handled by the DC-DC stage, while maintaining the functionality and partiality features of the converter.
- Determination of the most suitable impedance network based dc-dc converter configuration for each battery voltage system. The first converter introduced in this thesis features an impedance network composed of two capacitors and an inductor, which substitutes the commonly used HF transformer. The second configuration derives from the traditional topology of buck-boost converters, the midpoint between the two switches is connected via a capacitive impedance network to the midpoint of a half-bridge diodes.
- An in-depth theoretical analysis and mathematical model of the proposed impedance network converters.
- The development, implementation and evaluation of laboratory prototypes of the impedance network converters which validate the theoretical analysis of the proposed converters.

1.5 Outline of the thesis

Chapter 2 presents the state-of-the-art of EV battery chargers, from on-board systems to external chargers. The chapter also discusses the various converter topologies utilized in charging systems.

In Chapter 3, two new impedance network PPCs are presented, detailing their topology, operating principles and mathematical models.

Chapter 4 provides an in-depth description of the controller design, simulation results and an efficiency analysis.

In Chapter 5, the experimental prototypes for the proposed DC-DC converters are described. Models for both converters are detailed. The analysis of the experimental results and the efficiency measurements for each prototype are provided.

Finally in Chapter 6, the main conclusions and future research lines are discussed.

Chapter 2

ELECTRIC VEHICLE BATTERY CHARGERS

IN the last five years, the adoption of EVs has been growing at a rate of more than 35% per year. As a result, EVs accounted for 18% of global sales in 2023 and made up 2.1% of the total car stock worldwide [25]. This increase in adoption can be attributed to various factors including environmental concerns, decreasing costs of EVs, government incentives, and advancements in battery technology such as improved range and lifespan [5, 26]. However, the widespread adoption of EVs has been hindered by the presence of multiple and constantly changing charging standards, as well as a lack of fast charging infrastructure deployed at a global scale.

The progress in Li-ion battery technology has established it as the preferred option for EV manufacturers, making EVs more economically viable [5,11,26–28]. The industry has made significant advancements in the nominal voltage of EV batteries, transitioning from the typical 400 V configuration to 800 V. This increase in voltage allows for higher efficiency in the powertrain and in the battery charging process. The development of EV batteries has progressed alongside improvements in battery chargers [5, 26]. Currently, fast charging stations available on the market can reach charging rates of up to 600 kW, and it is projected that this charging power will continue to increase as the market expands [29].

The constant battery capacity improvement has imposed substantial challenges on battery chargers and available charging rates [5]. For instance, with a conventional 7 kW home alternating current (AC) charger, the 100 kWh Tesla Model S requires over 15 hours to complete the charge from empty to full. Otherwise, a public 150 kW DC fast charging station can bring the Model S from 20% to 80%

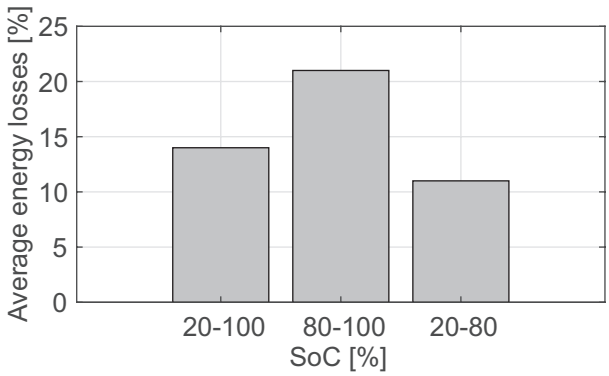

Figure 2.1: Average energy losses from grid to battery for the tested SoC areas in BMW i3 [3].

SoC in about 30 minutes [30]. As an additional illustration, the Hyundai Ioniq 5 with a battery capacity of 77.4 kWh can be fully charged in approximately 25 hours or replenished from 20% to 80% SoC in around 20 minutes using the aforementioned charging methods [31].

In several publications, the operation of EVs is recommended to be within a safety SoC range, typically from 20% to 80%. The works in [32] and [33] establish that, when the battery operates outside the safe range, the fastest capacity fade occurs by increasing the internal resistance of the battery; while operating within the suggested range, the battery presents excellent cycling performance with essentially reduced capacity degradation. In [3] a study to experimentally investigate EVs battery behavior during charging and to quantitatively define potential energy losses, based on the commercial model BMW i3, is presented. Figure 2.1 shows the results for the average energy losses of the complete charging processes, for different SoC scenarios, where it is observed that the average energy losses are lower for the operating range 20% to 80%. Among the different factors contributing to these losses, the most significant include the charger losses in both its AC-DC and DC-DC stages,wiring losses, undesired electrochemical reactions occurring within the battery, and other related factors.

In order to further support a potential large-scale adoption of EVs, the development and improvement of charging stations are crucial. One of the main challenges that charging stations must overcome are achieving adaptability for both old LV and new HV systems, complying with local power system regulations, maintaining adequate safety measures, and allowing charging of batteries regardless of their SoC.

As shown in Figure 2.2, the power electronics of the charging station, can be classiffied into two groups depending on their location, on-board and off-board charg-

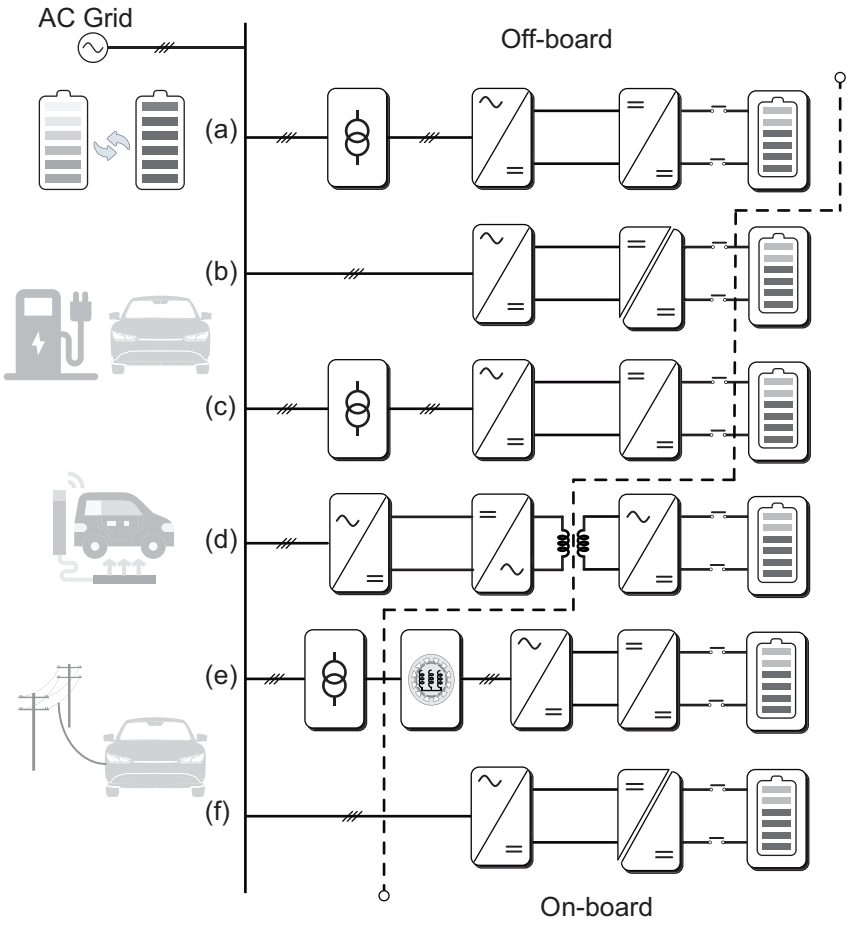

Figure 2.2: Classification of different structures for EV battery chargers [4]: a)Battery swapping; b) HF isolated off-board charger; c) LF isolated off-board charger; d) Wireless charger; e) On-board integrated charger; f) On-board dedicated charger.

ers, which are subdivided according some characteristics [5]. Several possible power electronics configurations for EVs chargers are shown in Figure 2.2. Figure 2.2 a) illustrates the charging architecture for battery swapping, battery swapping is a method where a depleted vehicle battery is exchanged with another one that has already been fully charged. One of the benefits of this approach is the short charging time for the vehicle battery, which is comparable to the time spent refueling at a gas station [34–36]. In addition, EV owners do not need to be concerned about setting up a battery charger at their location. However, battery transportation, charging centers, and all related logistics are a challenge for this method [37, 38]. Figure 2.2 d) represents wireless or inductive charging methods [39] highlights it as

a method safe, convenient hazardous-free. Different topologies and advantages of this method are analyzed in [40–45]. For the purpose of this thesis both battery swapping and wirless charging are not further addressed since their applicability is not mainstream and falls out of the scope of the thesis.

Figures 2.2 b) and 2.2 c) depict the architecture for off-board charging stations where batteries are not swapped. In Figure b), galvanic isolation is integrated into the DC-DC converter, eliminating the need for an low-frequency (LF) transformer. In contrast, in Figure c), galvanic isolation is provided through an LF transformer, allowing the use of transformerless configurations in the DC-DC converter. Figures 2.2 e) and 2.2 f) present on-board charging configurations where the charging process occurs within the electric vehicle. Two configurations are illustrated: figure e) features integrated chargers that utilize the existing EV power train for charging, while figure f) details the setup for dedicated chargers, where the power electronics is exclusively dedicated to charging functions.

At present, the dominant approach for EV fast chargers involves a power conversion system consisting of two stages: an AC-DC conversion stage followed by a DC-DC conversion stage. This system utilizes fully rated power converters [5,46–48]. In the case of traditional 400 V battery configurations, a standard approach for connecting to a 400 VAC grid would involve the use of a step-down DC-DC stage to control the battery charging process. However, in the case of newer EVs that utilize 800 V configuration battery systems, the DC-link voltage is often lower than the battery voltage. As a result, a DC-DC converter is required to increase the voltage in order to facilitate the charging process. Various boost converter topologies for charging stations can be found in existing literature [49–53].

For off-board chargers, the galvanic isolation can be fulfilled by implementing either LF isolation transformer at the grid side or HF isolation transformer as a component of the DC-DC stage [5, 26, 27]. Referring to Figure 2.2 b), where an HF transformer is employed, the literature identifies two distinct subdivisions, illustrated in Figure 2.3 a) and Figure 2.3 b). Common topologies for these chargers include regulated DC-DC converters with HF isolation transformers, such as the dual active bridge configuration [54], shown in Figure 2.3 a), and unregulated soft-switched resonant converters followed by a post-regulation DC-DC stage, as depicted in Figure 2.3 b). In all of these solutions, the DC-DC stage connects the DC bus, which is the output of the AC-DC converter, to the battery and is responsible for controlling the current supplied to the battery based on the charging profile.

One benefit of employing a HF isolation stage without regulation and incorporating a post-regulation DC-DC converter, as shown in Figure 2.3 b), is that it enables the isolation transformer to operate at a fixed input-output voltage, leading to in-

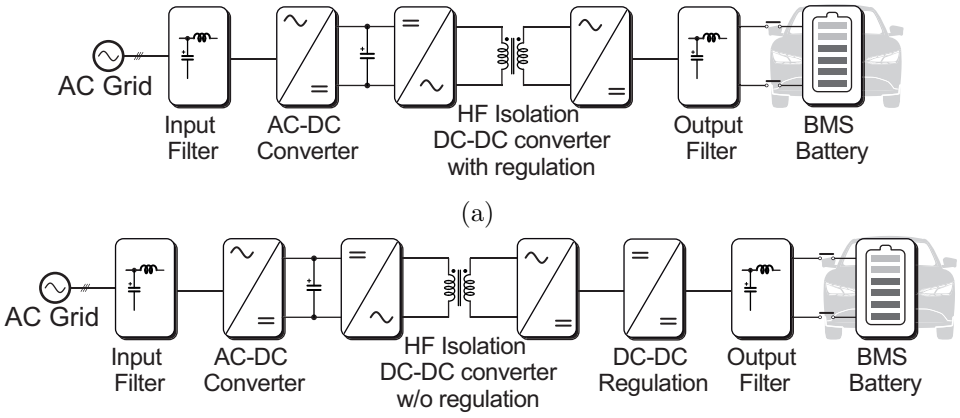

Figure 2.3: Off-board configurations whit HF isolation architectures: a) With regulated HF isolation; b) With unregulated HF isolation and post-regulation.

creased efficiencies. When the input voltage of a transformer varies, the magnetic flux in its core changes accordingly, resulting in a variation in the output voltage. This voltage fluctuation leads to losses in the transformer core due to hysteresis and the induced eddy currents [55]. LLC resonant converters are extensively utilized in a range of applications, particularly for battery charging, because of their simple design and excellent efficiency achieved by employing zero voltage switching (ZVS) and zero current switching (ZCS) operation. However, this efficiency drops significantly when the input and output voltages vary, causing the converter to operate far from its resonant frequency. To achieve optimal efficiency in the operation of the converter, it is possible to maintain the input and output voltages at the converter optimal operation point. Additionally, an extra regulation stage, without isolation, can be included to enable output voltage regulation. The overall efficiency of a two-stage FB LLC converter and an HF isolation converter without regulation, which incorporates a post-regulation DC-DC converter stage, is compared in [56].

2.1 On-board charging

Early EVs were charged with power levels around 3.3 kW [57, 58], however, the increase in battery capacities has led to a growing demand for higher power on-board chargers. Presently, almost all new EVs are equipped with options for 7.4 kW, 11 kW, and 22 kW chargers [59, 60]. Nevertheless, to support charging at these power levels, residences or the locations they are connected require a three-phase connection.

There are principally two types of on-board chargers: integrated and dedicated

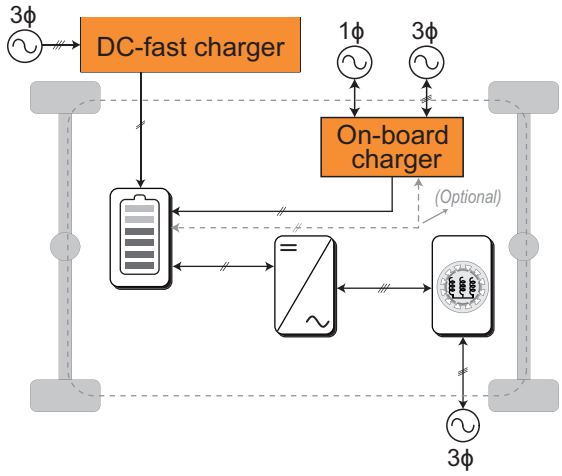

Figure 2.4: EV power system and typical charging modes.

chargers. A dedicated charger is a standalone unit with a single functionality to serve as EV charger. On the other hand, the integrated systems exploit existing power electronics components available in the power train of the EV, specially in the electric motor and the inverter, that are used as the battery charger instead of a separate charging system. The motor windings can be used as filter inductances while the drive inverter is used as a DC-AC bidirectional converter connected to the battery. Figure 2.4 shows an illustration of the typical EV power train. The battery is responsible for feeding both the propulsion system and a LV battery, used for the auxiliary services through the auxiliary power module. In addition, the main charging methods are highlighted, on-board and off-board chargers.

2.1.1 Dedicated chargers

In general, an EV can be charged using a dedicated on-board charger that is compatible with standard domestic outlets. Since the on-board charger is contained within the vehicle, manufacturers are constrained by size and weight limitations when designing them. However, on-board chargers offer significant flexibility, as they can be used with regular power outlets without the need for any additional equipment [60, 61].

Hence, it can be concluded that a primary goal in the development of on-board chargers is to achieve a high maximum power while maintaining a small power density [61, 62]. In addition, a significant drawback of the on-board chargers is related to the outlets to which they are connected. In order to ensure satisfactory power quality, an on-board charger must be capable of meeting the requirements of various

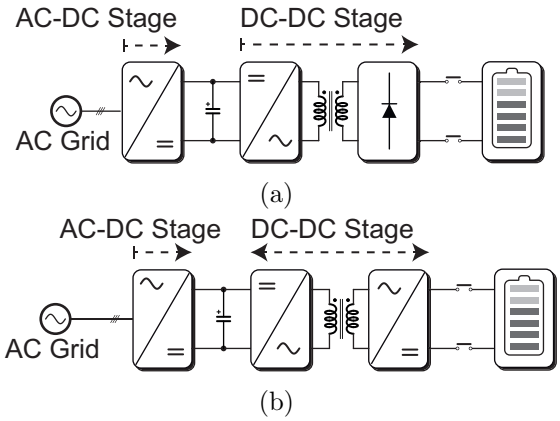

Figure 2.5: On-board charger: a) Unidirectional; b) Bidirectional.

AC grid standards [5]. The International Electrotechnical Commission, IEEE 519, Society Automotive Engineers (SAE) J2894, and Guobiao recommended standards (GB/T) 14549 address the standards related to harmonic injection for EV chargers during the charging process. IEC61851-22-23, GB/T20234-2, and SAE J1772-2017 are additional standards concerning connector types, voltage and current specifications, and phase numbers for on-board chargers [63, 64].

On-board chargers may be designed to operate in either unidirectional or bidirectional modes, as illustrated in Figure 2.5. The general structure of a unidirectional on-board charger is presented in Figure 2.5 a). The system consists of a rectifier stage, which is then followed by an AC-DC converter, and a DC-DC stage, that adjusts the intermediate DC voltage to the necessary voltage levels to control the charging process [58, 65]. Diode bridges are commonly employed on the secondary side of the DC-DC converter to simplify the system. By implementing HF isolation, the battery is effectively separated from the AC grid to ensure safety. [66]. On the other hand, Figure 2.5 b) depicts the setup of a bidirectional on-board charger, which possesses the capability to transfer power from the vehicle to the grid (V2G), vehicle to home (V2H), vehicle to external loads (V2L), and vehicle to vehicle (V2V). Consequently, an active stage is required on the secondary side of the DC-DC converter and in the grid rectifier [67–70]. These services enabled by bidirectional on-board chargers are therefore also comonly refered to as V2X where X stands for Grid, Home, Load, Vehicle, or any other recepient of the power.

On-board chargers are available in various power ratings including 1.7 kW, 6.6 kW, 11 kW, 22 kW, and even to 40 kW. Single-phase on-board chargers topologies are commonly used for power ratings of 3.3 kW and 6.6 kW. However, the presence of a high-power pulsation at twice the frequency could introduce relia-

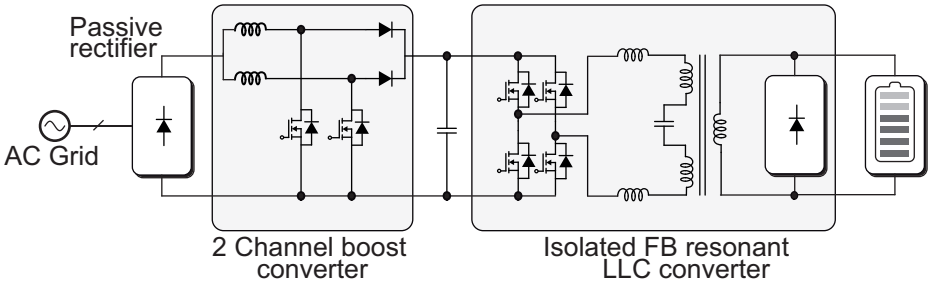

Figure 2.6: Second-generation Chevrolet Volt on-board charger.

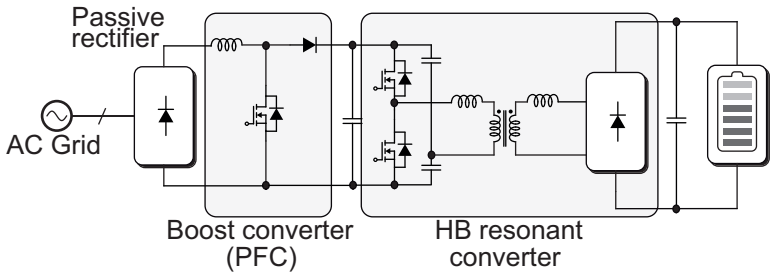

Figure 2.7: Unidirectional on-board charger cell rated 3.5 kW.

bility concerns in this charger design [71]. To avoid the necessity for a large DC capacitor, which could result in a low-power density, several control strategies have been proposed to mitigate the distortion in the output current [72, 73]. To support higher power ratings, researchers have developed a three-phase topology capable of operating in two modes. The first mode is a modular configuration composed of three separate single-phase on-board chargers, while the second mode involves a direct three-phase input topology [71]. The modular three-phase topology provides better reliability and efficiency than the direct topology [74]. However, the primary disadvantage of the modular setup is the need for additional power transistors and sensors [75].

Various types of on-board chargers can be found in industry and literature. For instance, the second-generation for the Chevrolet Volt, show in Figure 2.6. The Chevrolet Volt charger includes two stages; the first, through a passive rectifier transforms AC voltage to DC pulsating voltage and boosts immediately to a typical value of 400 V, followed by a two-channel interleaved boost converter. This topology doubles the current ripple frequency, reducing the size of the components in the input filter. Next, a DC capacitor, required to filter the double frequency component of the rectified AC grid frequency, connects the second stage, composed of a resonant LLC DC-DC converter. The latter can eliminate the switching losses by using ZVS and ZCS. Operating at 400 V and rated 3.6 kW, this on-board charger

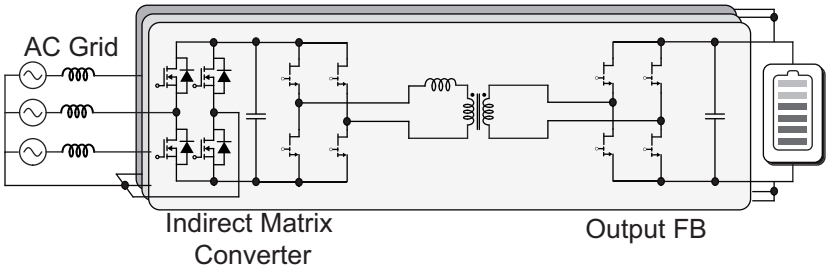

Figure 2.8: Matrix-type Hella converter.

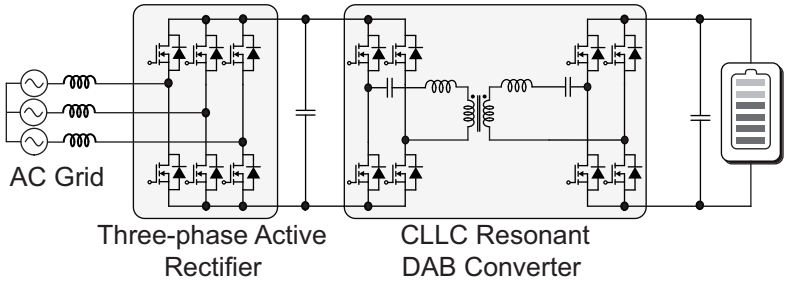

Figure 2.9: Texas 6.6 kW bidirectional on-board charger.

reports 93% efficiency [76].

In [79], the authors developed a 10.5 kW unidirectional on-board charger shown in Figure 2.7. This charger consists of three single-phase cells, each with a power rating of 3.5 kW. These cells are connected to the grid through a diode bridge rectifier. After the rectifier, a boost converter is used for power factor correction (PFC) and to regulate the voltage in the DC-link capacitor. The half-bridge (HB) resonant converter combines the DC-DC stage, which controls the output voltage and current needed for the BMS. A reported efficiency of 95.6% is observed. Nevertheless, the resonant capacitors experience significant stress.

In [77], the so-called indirect matrix converter shown in Figure 2.8, transforms the frequency of the grid into an intermediate frequency. Up to 98% efficiency can be attained when operating this converter in a single-phase mode with a power of 7.2 kW.

Texas Instruments has designed a bidirectional on-board charger with a power rating of 6.6 kW, which is illustrated in Figure 2.9. The topology consists of a three-phase active rectifier that helps to minimize the fluctuation in the inductor current. It is combined with a resonant CLLC DC-DC converter. By connecting them in interleaved mode, the power level can be increased, and power losses can

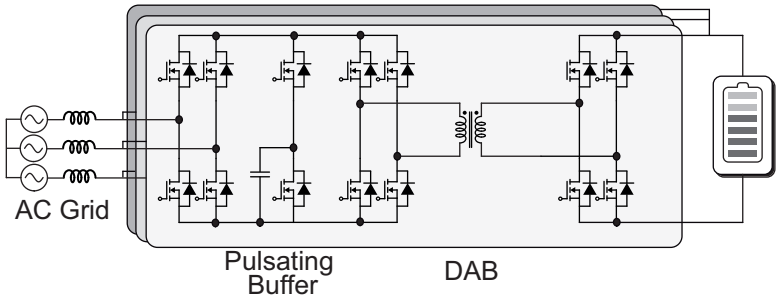

Figure 2.10: Power pulsating buffer topology.

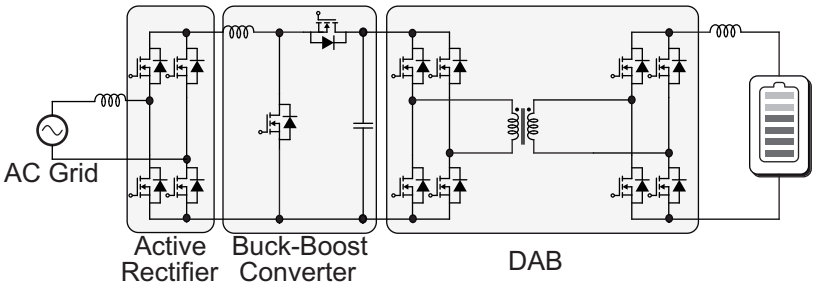

Figure 2.11: Hyundai On-board bi-directional converter.

be reduced. The output voltage can be adjusted between 250 V and 450 V, with a maximum efficiency of 97% at light load conditions [78].

In [80] a high-power density pulsating buffer on-board dedicated charger is presented. This converter, shown in Figure 2.10, is based in a power pulsating topology, aiming to achieve a high-power density, as well as high efficiency. The article emphasizes that the overall effectiveness decreases by slightly less than 1% with the incorporation of the extra power pulsating buffer.

Figure 2.11 illustrates another bidirectional converter, which is capable of converting power in both directions. This converter topology is specifically attributed to Hyundai's bidirectional on-board charger. It incorporates an active front-end converter that is controlled by PWM to establish a connection with the grid, followed by the PFC circuit unit, composed of a buck-boost converter. In a standard battery charging procedure, this circuit acts as a boost converter, increasing the voltage transferred from the rectifier stage. Conversely, when the battery is used as a power source, the converter operates as a buck converter, decreasing the voltage from the battery. The DC-DC stage is formed by a dual active bridge converter, which enables the injection of voltage and current into the battery during the charging process [81].

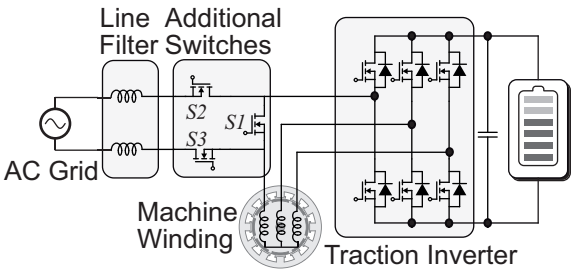

Figure 2.12: Single-phase integrated on-board charger.

There are several other topologies proposed for on-board chargers, both in the literature and by industry [75, 82–84].

2.1.2 Integrated chargers

One of the primary drawbacks of dedicated on-board chargers is the limited space and weight constraints in EVs [58]. This is because these chargers are only used when the vehicle is stationary and serve no other purpose than charging. As an alternative, integrated on-board chargers have been proposed. These chargers make use of the existing components of the EV power train, such as the electric motor and the inverter, for the additional purpose of charging the battery. Furthermore, the majority of the latest EV traction systems have a power ratings exceeding 50 kW and remain inactive while being charged. As a result, these systems can be utilized as integral components of high-power on-board chargers [5].

Additionally, some technical requirements are necessary for the correct operation. For instance, zero average torque and torque ripple are required during the charging process. The integrated on-board charger characteristics will highly depend on the motor type, number of phases, and power converter [85].

Integrated on-board chargers must have the capability to be reconfigured in terms of hardware to switch between the modes of traction and charging. These chargers have the capability to be reconfigured either to single-phase or three-phase systems connected to the grid. In particular, when connected to a three-phase system, the stator windings will experience three-phase currents, resulting in the generation of an average torque. Consequently, a mechanical lock is necessary, which significantly impacts the efficiency of the system due to the increased losses in the rotor copper and core [86].

In [87] a solution consisting in a single-phase integrated charger is presented. The topology consists of a three-phase induction motor and a conventional three-phase

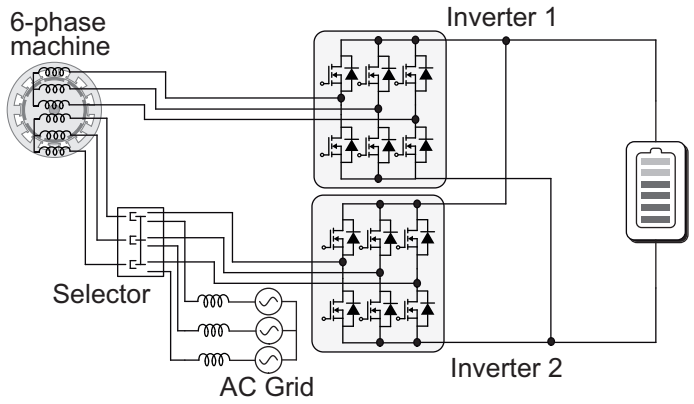

Figure 2.13: On-board charger fully integrated with 6-phase traction motor drives.

inverter, in association with three additional switches, as is shown in Figure 2.12. S1, S2, and S3 allow motor reconfiguration during both modes of operation. In traction mode, S1 is closed while S2 and S3 are open, resulting in a three-phase motor drive system. For charging mode, S1, S2, and S3 inverse their operation mode, in such a way that the motor leakage inductances together with two legs of the inverter operate as a boost converter. The line filter is used to minimize line current harmonic distortion. The main disadvantage of this topology is the presence of additional switches, which increase the conduction losses.

Figure 2.13 illustrates a charger that can be adjusted for a system featuring a 6-phase motor. The goal is to improve energy density by combining the vehicle charger with the traction system, thereby minimizing the required components. The system can be reconfigured by switching between the drive and charge modes using a selector, and can reach overall efficiency of 93% [88].

A novel topology, illustrated in Figure 2.14, utilizes a balanced six-phase machine that does not generate any torque during the charging mode as described in [89], also achieving unity power operation at the grid side. During the traction mode, the six-phase machine is powered by the battery through a bidirectional boost converter and a nine-switch converter. The nine-switch converter functions as a six-phase converter in this mode. It is necessary for the reconfigurable switches S1 and S2 to remain closed, while S3 should be open. In order to enable battery charging, the converter operation mode needs to be modified. This requires changing the state of S1, S2, and S3, which in turn causes the converter to function as an active rectifier. Additionally, the six-phase windings are utilized as filters on the grid side. In addition, several other topologies and control techniques based on three-phase charging and multi-phase machines are described in [90–95].

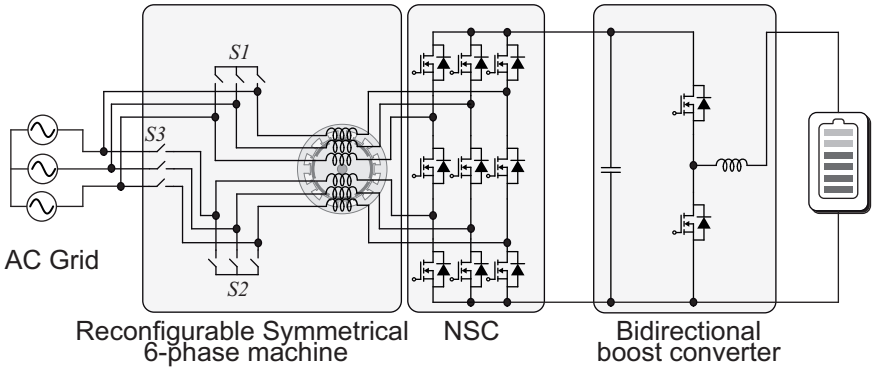

Figure 2.14: Nine-switch integrated on-board charger converter.

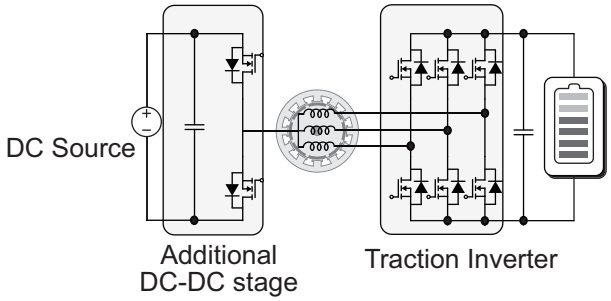

Figure 2.15: Integrated DC on-board charger.

An integrated DC charger is proposed in [96] and shown in Figure 2.15. The purpose of this topology is to offer numerous functionalities. For example, it integrates the traction inverter with the charging system, utilizes the motor winding inductances as the filter for the charging system, allows bidirectional fault block capabilities, enables charging at different voltage levels based on the battery voltage. The only addition to a typical EV drivetrain is the DC-DC stage shown in Figure 2.15. However, a disadvantage is the need to have a DC source that allows fast charging, also; for the simultaneous traction-charging operation; there must be a mobile source to provide the charging power, for instance, a roof top solar panels or wireless power transfer roads, which would significantly limit the charging power.

2.2 Off-board charging

The previous section showed that weight and volume limitations of on-board chargers leads them to operate with reduced power ratings, slowing down the charging process; aimed at over night charging and domestic use. An alternative is through DC fast chargers, typically rated between 50 kW to 350 kW. Unlike on-board charg-

ers, a domestic infrastructure cannot manage the fast charger power ratings, giving birth to the concept of fast-charging stations.

The primary goal of a fast charging station is to enable an EV battery to be fully charged within a few minutes, similar to conventional gas stations. Typically, a fast charging station is a public facility that houses multiple fast chargers, allowing multiple batteries to be charged simultaneously. To ensure drivers have sufficient range, fast charging stations should be strategically placed throughout the operating region. Numerous studies in the literature examine the impact of fast charging stations on the public power grid and investigate their optimal placement, operation, and management [47, 97–99].

A DC fast charger is responsible for converting the three-phase AC voltage into the required DC voltage. The typical configurations involve two stages of conversion. The first stage is an AC-DC rectification stage with PFC, which converts the AC voltage from the grid into an intermediate DC voltage. The second stage is a DC-DC converter, which transforms the intermediate DC voltage into a regulated DC voltage that is necessary for the BMS to charge the battery. In some instances, the DC-DC stage is split into two DC-DC substages. The first substage provides the required galvanic isolation without regulating voltage and current, while the subsequent substage focuses on voltage and current regulation but lacks galvanic isolation.

Three different architectures have been developed for connecting multiple chargers within the same station, as illustrated in Figure 2.16. In the first case, depicted in Figure 2.16 a), a standard three-phase AC bus is formed by utilizing a step-down transformer that is linked to the MV grid. Each battery charger in the station is connected to the AC bus via separate AC-DC converters. One of the benefits of utilizing this design is that each charger operates autonomously, enhancing the stability of the system. Additionally, there are protection devices and established standards and practices for both the AC grid and EV charging stations [100]. Nevertheless, the number of stages involved in converting the grid power to battery power experiences a notable increase. This increase in semiconductors leads to a greater level of complexity and cost for the system, while also causing a decrease in overall efficiency [101]. Figure 2.16 b) shows the same AC bus configuration, but takes into account the galvanic isolation within each DC-DC converter.

On the other hand, the DC common bus architecture Figure 2.16 c) requires a high-power AC-DC main converter that generates the DC common bus. To carry out the charging process, the EVs batteries are connected to the DC bus using individual DC-DC converters, as depicted in Figure 2.16 c). The flexibility of the system is enhanced by this architecture, as it enables the seamless integration of extra stages like renewable energy generation sources or energy storage devices, due

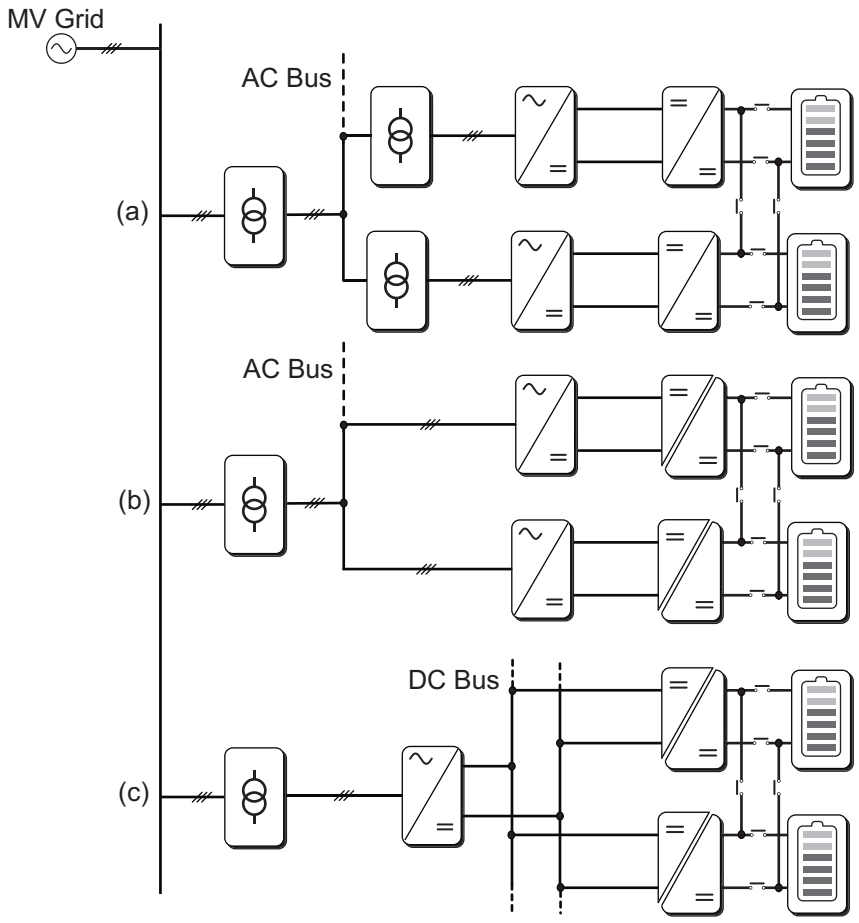

Figure 2.16: Fast charging station architectures: a) AC-bus with LF isolation; b) AC-bus with HF isolation; c) DC-bus with HF isolation.

to the available DC bus, where DC systems ca be directly coupled.

One of the drawbacks of the DC architecture is that when only a few vehicles are charging, the AC-DC converter, designed for the total power assuming that all vehicles are charging, will operate at a lower power level, far from its optimal value. This results in low efficiency. Hence, DC architecture is more suitable for fleet charging stations, such as those for buses and trucks, where there are usually numerous charging stations for vehicles.

A different approach mentioned in the academic literature to eliminate the requirement of using a large and heavy LF MV-LV transformer is the utilization of a power electronics-based as solid state transformer (SST) that can directly connect with the MV grid. Compared with a traditional line-frequency transformer, the

Table 2.1: Specifications of commercial DC off-board fast chargers.

	ABB	**Phihong**	**Tesla**	**ABB**	**Hyundai**
Model	Terra 360	Integrated	Supercharger	Terra HP	E-Pit
Power	360 kW	120 kW	135 kW	350 kW	350 kW
Vout	120-920 V	200-750 V	50-410 V	120-920 V	800 V
Iout	360 A	240 A	330 A	500 A	400 A
Efficiency	-	93.5%	91%	95%	-
Add 320 km	10 min	30 min	27 min	10 min	10 min

SST has better controllability, current limiting capabilities [102]. Several studies have suggested the utilization of a SST to establish a DC bus that can connect with various DC sources and loads [103, 104]. In [105–109] different MV fast chargers developed based on SST are shown.

DC systems face various challenges, including DC protection and DC metering. Safeguarding a DC-connected system involves coordinating multiple factors, such as grounding configuration, fault type, and topology, among others [110].

2.2.1 Off-board DC-fast charger configurations

The current market trend focuses on the advancement of high-power off-board DC fast chargers or ultra-fast chargers. Examples of such chargers include the ABB Terra HP and Hyundai E-Pit, which are capable of supplying up to 350 kW of power to the battery, Table 2.1 lists some of the DC off-board fast chargers available on the market. Based on the charger design and the chosen topologies or circuits, various configurations can be achieved. This section will introduce some of these configurations.

An LLC resonant HB with reconfigurable output converter used for the ABB Terra 53 is depicted in Figure 2.17. This converter is designed in a modular way, with several stages of the circuit connected in parallel. Depending on the desired output, different stages can be turned on or off. The adaptable rectifier enables connection to both 400 V and 800 V vehicles. It has been reported to achieve a peak efficiency of 95% [111].

Another featured charger on the market is the Tesla Supercharger V2, shown in Figure 2.18, which is composed of two power stages. The first one corresponds to a passive rectifier with a boost PFC, followed by a phase-shift (PS) FB DC-DC

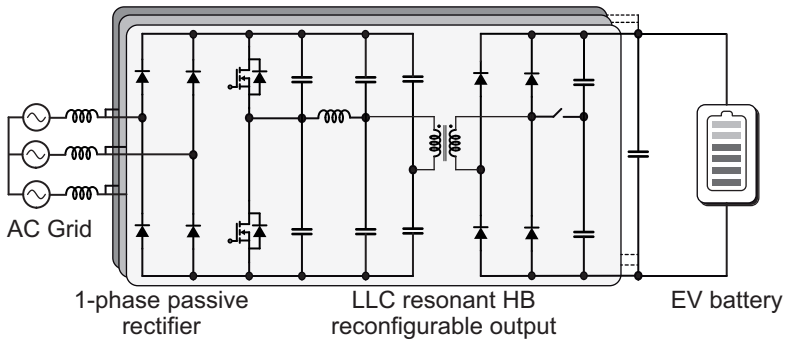

Figure 2.17: LLC resonant HB with reconfigurable output converter for the ABB Terra 53/54 50 kW fast charger.

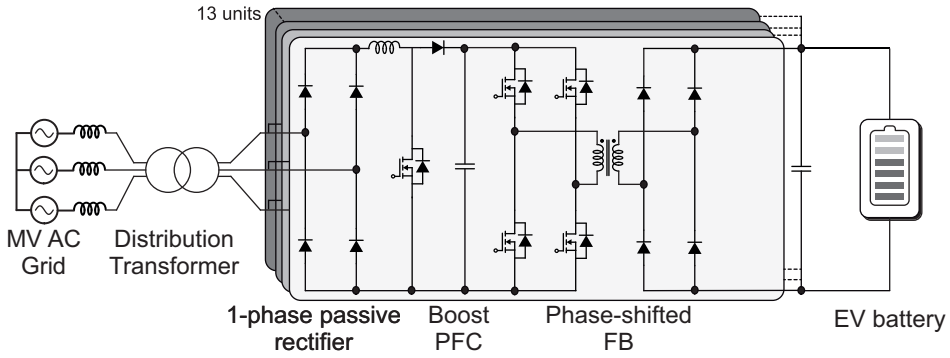

Figure 2.18: Modular PS FB DC-DC converter for the Tesla Supercharger V2.

converter to charge the battery. Like Terra 53/54, Tesla Supercharger is built in a modular way; 13 units are able to charge a single vehicle up to 150 kW. A 92% efficiency is reported [112].

Figure 2.19 depicts the topology of the Terra High Power (HP) series. These chargers can deliver up to 150 kW by interleaving three 50 kW modules. The Terra HP 150 series achieves low-frequency isolation via a transformer connected to the MV-AC grid, the transformer output is connected through an input filter to an active rectifier, followed by the DC-DC stage, which is composed of a 3-channel interleaved buck converter. When the charger operates at full capacity, it achieves a peak efficiency of 94%. If higher power levels are needed, multiple units can be combined, allowing a peak power of up to 600 kW.

Porsche stands out as another company that has developed its own off-board fast chargers, as shown in Figures 2.20 and 2.20. In both topologies, galvanic isolation is provided by a phase-shifting transformer connected to the MV-AC network. In

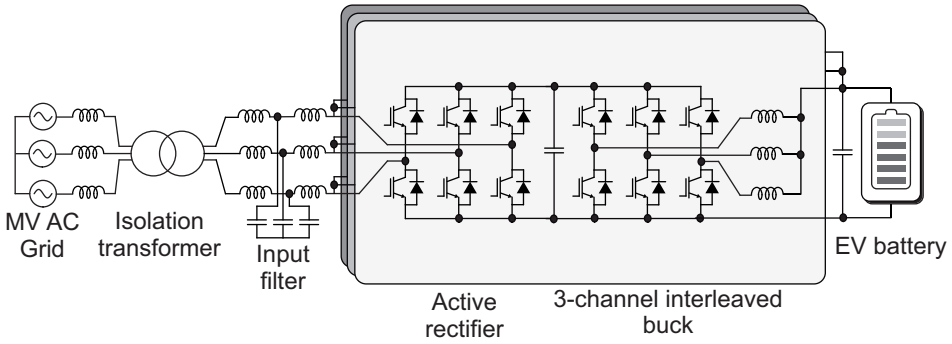

Figure 2.19: DC-DC 3-channel buck interleave converter for the ABB Terra HP 150 kW series.

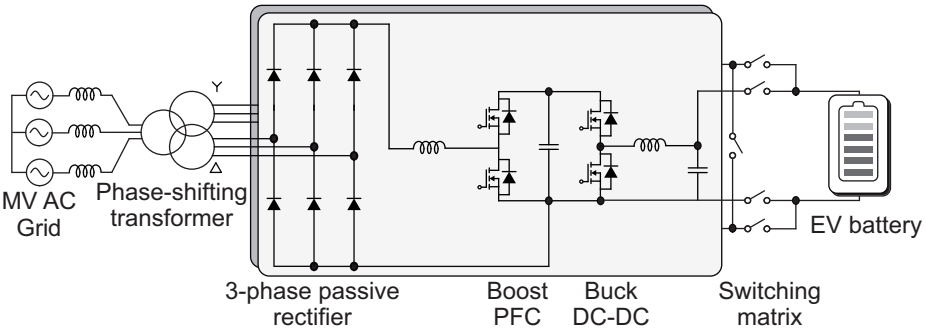

Figure 2.20: Porsche modular fast charging park version A.

version A of the Porsche modular fast charging park [113], illustrated in Figure 2.20, a 3-phase passive rectifier followed by a PFC booster establishes a DC link, which is then connected to a DC-DC buck converter to regulate the voltage and current injected into the battery. In [114] introduces the version B of the Porsche modular fast charging park, Figure 2.20, where the 3-phase passive rectifier is replaced by a Vienna rectifier, and the DC-DC converter is substituted with an interleaved three-leg buck, thus enhancing the output current ripple.

In [115–119] different topologies of chargers used in fast-charging stations around the world are presented and analyzed.

2.3 Charging standards

Industry, regulations and academia establish that AC charging solutions cover the lower end of the power ratings of battery chargers up to 25 kW, while DC solutions cover the remaining part up to 400 kW, with projections up to 900 kW [5]. All the

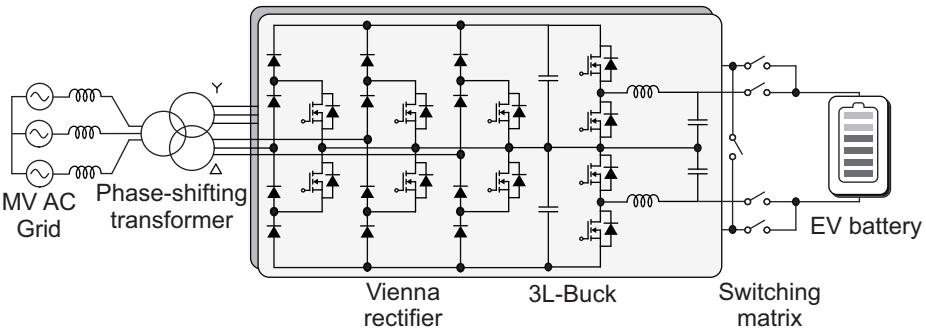

Figure 2.21: Porsche modular fast charging park version B.

charging options make it clear that EVs have a much larger power requirement, and the methods for supplying this power needs to be standardized.

An example of a charging standard is the Japanese CHAdeMO, initially with a power of up to 50 kW. However, with battery technology development, the standard updated their specification up to 100 kW, and in 2018 a new update was made with CHAdeMO 2.0 with a maximum power rating of 400 kW. The latest version released in 2020 provides a rate of 900 kW, mainly thinking about reducing charging times. Another option is provided by Tesla, company that developed its own standard dedicated to their vehicles. Current Tesla chargers are capable of delivering between 250 kW to 350 kW [120].

The GB/T standard, developed by Chinese and Indian EV manufactures, supports a maximum power rating of 237 kW.

In 2014 the CharIn organization tried to deal with the incompatibilities between EV estandards, by developing the Comnined Charge System (CCS). This solution covers AC charging and DC fast-charging, in both US (Type 1) and Europe (Type 2). CCS supports a maximum power of 400 kW [5].

Table 2.2 summarizes the main features of DC charging standards.

2.4 Conclusion

This chapter has provided an in-depth examination of the current advancements in utilizing DC-DC converters for EV battery chargers, encompassing their use in on-board chargers, whether dedicated or integrated, as well as external chargers, accommodating both low-power slow chargers and high-power fast chargers. These systems exist side by side because of their distinct uses and applications.

Table 2.2: DC CHARGING STANDARDS [5]

	CHAdeMO 2.0	**CCS-**1	**CCS-2**	**GB/T**
Max Power	400 kW	350 kW	350 kW	237 kW
Market Power	50 kW	312 kW	350 kW	60 kW
Output Voltage	50-1000 V	200-1000 V	200-1000 V	250-950 V
Max Current	400 A	500 A	500 A	400 A
Region	Global	US-S.Korea	Europe	India
Time per 100 km	13.73 min	4.4 min	1.96 min	11.44 min

Various topologies are utilized for both AC-DC and DC-DC converters in charging stations. The particular topology used is determined by the station design, as galvanic isolation might be necessary at different stages. Furthermore, the voltage levels might require boosting or reduction based on the battery type, along with other conditions that affect the selection of the circuit design. The technical specifications for the circuits differ on the basis of their application. For example, on-board chargers require a higher power density, while off-board chargers focus on increasing power output and supporting a wider range of output voltages.

A noticeable trend towards modularity using interleaved designs has emerged, as this method improves power quality, diminishes the size of magnetic components, and grants greater flexibility in designing charging stations across different power levels. It is necessary to explore DC-DC converter topologies that can modify existing 400 V charging stations to be compatible with 800 V EV batteries, or to develop charging stations that can support the entire voltage range.

Chapter 3

PROPOSED DC-DC STAGES FOR FAST CHARGERS

THE DC-DC conversion stage plays a vital role in the EV charging process, as it is responsible for regulating both voltage and current. DC-DC converters are required to meet modern charging demands for both 400 V and 800 V battery configurations. As shown in the previous section,DC-DC converters are available in configurations with or without galvanic isolation. DC-DC converters that do not incorporate an HF transformer take advantage of the existence of galvanic isolation in a previous stage, either through an LF transformer in the AC-DC conversion phase or in a prior DC-DC conversion phase without regulation (refer to Figure 2.3), concerning the architecture that was last mentioned, it is important for the DC-DC converter to minimize the losses related to the two implemented DC-DC stages. In the upcoming sections of this chapter, two proposals for transformerless DC-DC converters are formulated, utilizing the concept of partial power processing.

3.1 Introduction to partial power converters

PPCs emerged to reduce the power rating of the power converter used in the DC-DC stage of PV systems, and potentially reduce the size, cost and losses associated to the dc-dc stage [121]. This idea has evolved to encompass a wider range of applications over time, including wind power systems, energy storage systems (ESS), and EV chargers [23, 122, 123]. The basis of PPCs lies in the notion of partial power processing (PPP), where the converter handles only a portion of the power supplied from the source to the load, while the rest is transferred without processing. This approach helps to reduce the losses associated with the converter. The authors in [124] suggest a categorization of these converters exclusively based on their

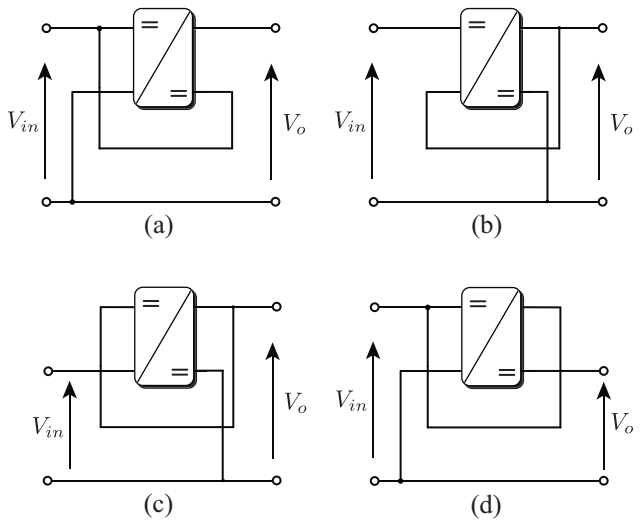

Figure 3.1: Different PPCs architectures: a) IPOS step-up; b) ISOP step-down; c) ISOP step-u;. d) IPOS step-down.

intended applications, resulting in three categories: differential power converters (DPC), PPC, and mixed strategies.

3.1.1 Classification

The initial set of converters that function on the basis of the PPP principle, referred to as DPC, is distinguished by their purpose to balance current disparities among multiple elements connected in series. Hence, it can be affirmed that DPC addresses this imbalance rather than the overall power provided by the combined elements [125]. In the literature, DPCs are commonly used in current balance systems within ESS and photovoltaic systems [126, 127]. These applications can be further divided into two groups based on how energy is transferred: element by element, where energy is exchanged between adjacent elements, and bus to element, where power is distributed from a common DC link to individual elements.

On the other hand, PPCs are characterized as topologies that prioritize regulating the current and voltage levels at the output of the converter, over the current balance between different elements. This characteristic makes these topologies ideal for charging electric vehicle batteries [124].

Various architectures, with or without galvanic isolation, can be identified in the literature depending on the PPCs applications. The key distinction among these architectures lies in how the PPC is integrated into the system, emphasizing config-

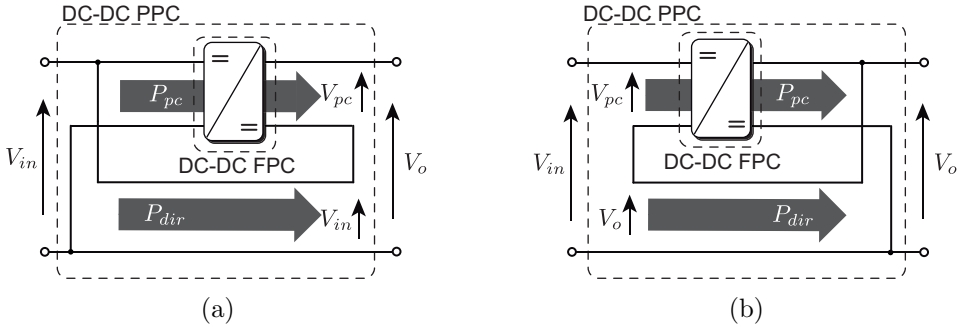

Figure 3.2: General structure of an ideal PPC DC-DC regulation converter: a) Type I PPC; b) Type II PPC.

urations such as input-parallel output-series (IPOS) and input-series output-parallel (ISOP). Figure 3.1 illustrates the diverse PPC architectures employed in different applications.

3.1.2 Principal PPC architectures for EV chargers

PPC have emerged as a compelling option for deployment as DC-DC converters in fast charging stations for EVs. PPCs can reduce losses, size, weight and the cost of the converter [24, 128]. PPCs are characterized by using topologies that process a fraction of the total power, thus allowing a reduction in power losses and converter size without sacrificing functionality.

Based on Figure 3.1, two variants are applicable for EV charging stations, which are shown in Figure 3.2, IPOS step-up and ISOP step-down, also known as Type I and Type II PPC respectively. In these configurations, P_{pc} represents the power handled by the full power converter (FPC), P_{dir} represents the power that goes directly to the battery, and P_o represents the total power delivered to the battery, *i.e.*, $P_o = P_{pc} + P_{dir}$. The voltage withstood by the converter is denoted as V_{pc}, while the input and output voltage of the DC-DC regulation stage are represented by V_{in} and V_o, respectively.

The voltage V_{pc} of Type I converters is determined by subtracting the input voltage V_{in} from the output voltage V_o. Type I PPCs connect the voltage V_{pc} in series with the output, making it more suitable for voltage step-up applications (resulting in a positive V_{pc}), since it only requires a unidirectional converter. On the other hand, Type II PPCs localize the voltage V_{pc} at the input, leading to a change in V_{pc} polarity. In this case, these converters are better for step-down processing with a unidirectional converter. Note that, it is also possible to implement step-down

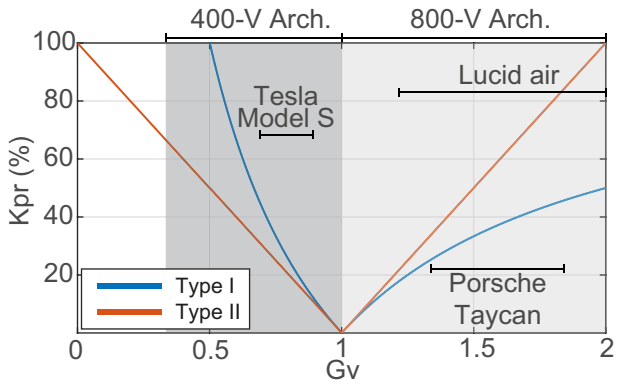

Figure 3.3: Partial power ratio converter of Type I and Type II PPC.

Type I or step-up Type II PPCs; however, the need for bidirectional converters diminishes their appeal for such applications. In order to analyze the partiality of the PPCs, a partial power ratio K_{pr} is defined, as the ratio between the power handled by the PPC in relation to the input power P_{in} of the whole DC-DC stage:

$$K_{pr} = \frac{|P_{pc}|}{P_{in}}, \tag{3.1}$$

In addition the converter voltage gain G_v can be defined as the ratio between the output and input voltage:

$$G_v = \frac{V_o}{V_{in}}. \tag{3.2}$$

For a Type I PPC, considering ideal components, the partial power ratio is given by [24, 128]:

$$K_{pr} = 1 - \frac{1}{G_v}. \tag{3.3}$$

On the other hand, the ideal partial power ratio for a Type II PPC is given by [24, 128]:

$$K_{pr} = G_v - 1. \tag{3.4}$$

A comparison of the partial power ratio variation is presented in Figure 3.3. Assuming a voltage gain G_v within the range 0 - 2 both types of PPC are compared, since this is the typical gain of converters used in EV charging applications for either 400 V and 800 V architectures. Note that in both cases an input voltage of 400 V is employed. Figure 3.3 illustrates that for 400 V systems, such as those employed in Tesla models, the converters must perform a reduction of the voltage. For step-down operations, Type II converters are favored because they can function as partial converters over a wider range, and the amount of power they manage is less than

that of Type I converters. However, for 800 V architectures found in newer models such as the Porsche Taycan or Lucid Air models, step-up operation is required from the same input. Hence, for this mode of operation, a better performance of Type I converters is clearly shown, since for a step-up operation they require to process less power than Type II converters. Then, if the converter operating in boost mode, the advantages of Type I over Type II converters can be explained as follows. As displayed in Figure 3.3, Type II converters gradually increase the power they handle to the point of no longer operating as PPC. In contrast, Type I PPCs do not face operating limits, because they keep operating in partial power mode despite increasing the converter gain. Furthermore, Type I PPCs in boost mode process a lower fraction of the power delivered to the battery compared to Type II PPCs [124, 129].

Conventional PPC configurations are characterized by including a HF transformer in their topology [24, 129]. However, the HF transformer does not provide galvanic isolation to the system since the PPCs have a bypass connection between the primary and secondary of the transformer. This connection allows part of the power to pass directly without being handled by the converter, but disables the isolation, hence the autotransformer nature of such PPCs.

In order to meet the isolation requirements, LF transformer is typically employed or by using an unregulated HF transformer or DCX. The HF transformer used in the PPC is there to provide a functional task, which is to inject a series voltage at the output ($V_o = V_{in} + V_{pc}$ for Type I PPC), or at the input ($V_{in} = V_o + V_{pc}$ for Type II PPC). The transformer does provide an extra degree of freedom in terms of turn-ratio design ($n_1 : n_2$) that along with the PS operation of the converter can give more flexibility to the input or output voltage gain. However, it comes at expense of extra losses, size and cost, without benefits of galvanic isolation. According to [130–132], by comparing isolated and non-isolated DC-DC converters that feature the same number of semiconductors, transformerless options can lead to a cost reduction between 51% and 57%.

3.2 Proposed impedance network type I partial power converter

In this chapter a new transformerless step-up Type I PPC topology for EV battery fast chargers is presented. The typically HF transformer of type I PPC is replaced by an impedance network. In the literature, these topologies are referred to as AC-link converters, nevertheless, they will consistently be referred to as impedance network converters in this thesis. This change makes the proposed converter lose the extra degree of freedom by not being able to design the turns ratio of the transformer. However, the PSM employed, generates a duty cycle, which is sufficient to regulate the battery charging process. Furthermore, the elimination of the transformer increases efficiency and power density, while reducing cost.

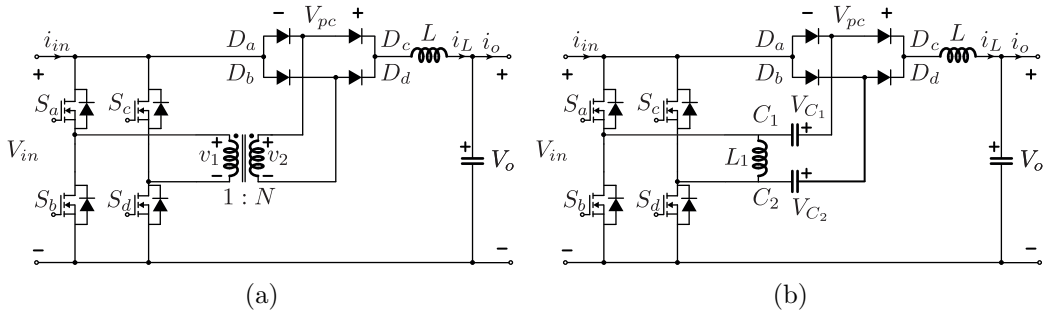

Figure 3.4: Step-up PPC Type I topologies: a) FB topology with transformer; b) Proposed impendance network PPC.

3.2.1 Topology description

The new transformerless Type I DC-DC PPC is designed to operate as the regulation DC-DC converter of a EV battery fast charging station. A conventional Type I PPC is presented in Figure 3.4 a). It uses a FB connected via a HF transformer to the output rectifier bridge [133,134]. Note that this HF transformer does not provide galvanic isolation because there is an electrical connection between the primary and secondary windings. This motivates the proposed converter shown in Figure 3.4 b), where the transformer has been replaced by an impedance network, this network is composed of an arrangement of two capacitors and an inductor in order to avoid the HF transformer losses, extra size and cost. Considering Figure 3.2 a), it can be seen that the proposed converter configuration corresponds to a series-connected Type I PPC. The input voltage V_{in} is connected in series to the partial voltage V_{pc} on the output of the secondary side of the converter.

The proposed converter considers the FB configuration at the input and a diode-bridge in series to the output, producing a series voltage between the input DC-link and the battery. Depending on the switching state of the semiconductors, the voltage across capacitors C_1 or C_2 is connected in series with the input voltage and the inductive output filter L. PSM has been employed to generate the switching states. This technique introduces a phase-shift α between the voltages generated by the legs of the FB in order to regulate the voltage rectified by the output diode bridge. This phase-shift varies within the range 0 - 0.5, corresponding to a displacement from 0° to 180°. Depending on the output requirements, the switching signals of S_a and S_c are phase shifted accordingly. Then, since signals S_b and S_d are the binary complement of S_a and S_c respectively, exhibit the same phase delay.

The two topologies in Figure 3.4 use the output inductor L to control both the

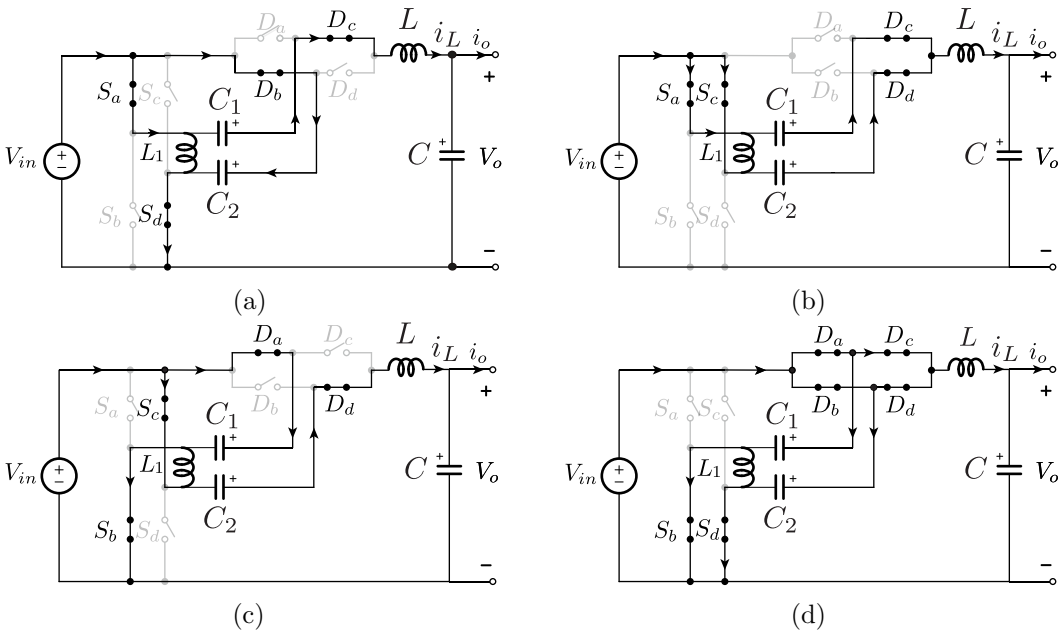

Figure 3.5: Switching states: a) State I (Sa, Sc) = (1, 0); b) State II (Sa, Sc) = (1, 1); c) State III (Sa, Sc) = (0, 1); d) State IV (Sa, Sc) = (0, 0).

output voltage and current, allowing the converter to perform the charging process according to the charging profile imposed by the BMS.

3.2.2 Operation principle

The proposed converter has four switching states obtained by the switching signals in the active bridge.

Switching state I (Sa, Sb, Sc, Sd) = (1, 0, 0, 1)

In state I, corresponding to Figure 3.5 a), the capacitor C_1 is connected in series with the input voltage and the voltage in the inductor L to the output. Considering Figure 3.5 a), the state variables equations can be obtained for the switching state I. Considering T as the switching period, the state duration $(0.5 - \alpha)\,T$ and the

switching states (S_a, S_c) = (1, 0), yields:

$$\begin{aligned} L_1\frac{di_1}{dt} &= V_{in} \\ V_{C_2} &= V_{in} \\ C_1\frac{dV_{C_1}}{dt} &= -i_L \\ L\frac{di_L}{dt} &= V_{in} + V_{C_1} - V_o \\ C\frac{dV_o}{dt} &= i_L - i_o \end{aligned} \tag{3.5}$$

Switching state II (Sa, Sb, Sc, Sd) = (1, 0, 1, 0)

For switching state II shown in Figure 3.5 b), the two capacitors C_1 and C_2 are connected in parallel and, at the same time, this arrangement is connected in series with the input voltage and output inductor voltage to the output. Considering Figure 3.5 b), the state variables equations can be obtained for the switching state II. Considering T as the switching period, the state duration αT and the switching states (S_a, S_c) = (1, 1), yields:

$$\begin{aligned} L_1\frac{di_1}{dt} &= 0 \\ V_{C_1} &= V_{C_2}, \\ C_1\frac{dV_{C_1}}{dt} + C_2\frac{dV_{C_2}}{dt} &= -i_L \\ L\frac{di_L}{dt} &= V_{in} + V_{C_1} - V_o \\ C\frac{dV_o}{dt} &= i_L - i_o \end{aligned} \tag{3.6}$$

Switching state III (Sa, Sb, Sc, Sd) = (0, 1, 1, 0)

In state III, capacitor C_2 is connected in series with the input voltage and the voltage in the inductor L to and the output, as displayed in Figure 3.5 c). Considering Figure 3.5 c), the state variables equations can be obtained for the switching state II. Considering T as the switching period, the state duration $(0.5 - \alpha)\,T$ and the switching states (S_a, S_c) = (0, 1), yields:

$$\begin{aligned} L_1\frac{di_1}{dt} &= -V_{in} \\ V_{C_1} &= V_{in} \\ C_2\frac{dV_{C_2}}{dt} &= -i_L \\ L\frac{di_L}{dt} &= V_{in} + V_{C_2} - V_o \\ C\frac{dV_o}{dt} &= i_L - i_o \end{aligned} \tag{3.7}$$

Switching state IV (Sa, Sb, Sc, Sd) = (0, 1, 0, 1)

State IV depicted in Figure 3.5 d), the capacitors of the impedance network are connected in parallel with the input of the converter, making the voltage V_{pc} equal to zero. Considering Figure 3.5 d), the state variables equations can be obtained for the switching state II. Considering T as the switching period, the state duration αT and the switching states (S_a, S_c) = (0, 0), yields:

$$\begin{aligned} L_1\frac{di_1}{dt} &= 0 \\ V_{C_1} &= V_{in} \\ V_{C_2} &= V_{in} \\ L\frac{di_L}{dt} &= V_{in} - V_o \\ C\frac{dV_o}{dt} &= i_L - i_o \end{aligned} \tag{3.8}$$

Note that the switching states connecting the capacitors of the impedance network in series with the input voltage of the converter define the step-up nature of the converter. Table 3.1 shows the voltage value of the semiconductor and the converter passive elements for each switching state.

To better explain its operation, the steady-state waveforms of the converter are shown in Figure 3.6. Figure 3.6 a) and Figure 3.6 b) show the gating signals of semiconductors S_a and S_c. Additionally, the theoretical waveforms of some signals of the proposed converter are displayed throughout a switching cycle. Figure 3.6 c) presents the drain to source voltage of the switch S_a over the course of an operation cycle. Then, Figures 3.6 d) and 3.6 e) show the voltages in the capacitors of the impedance network. Note that in steady-state these capacitors are charged to a voltage level equal to the input. In state I, the capacitor C_1 is connected in series with the input, which in turn results in a fraction of the input current circulating

Table 3.1: Type I impedance network PPC switching states.

S_a	S_b	S_c	S_d	V_{S_a}	V_{S_b}	V_{S_c}	V_{S_d}	V_{C_1}	V_{C_2}	V_{L_1}	V_L
1	0	0	1	0	V_{in}	V_{in}	0	V_{in}	V_{in}	V_{in}	$2V_{in} - V_o$
1	0	1	0	0	V_{in}	0	V_{in}	V_{in}	V_{in}	0	$2V_{in} - V_o$
0	1	1	0	V_{in}	0	0	V_{in}	V_{in}	V_{in}	$-V_{in}$	$2V_{in} - V_o$
0	1	0	1	V_{in}	0	V_{in}	0	V_{in}	V_{in}	0	$V_{in} - V_o$

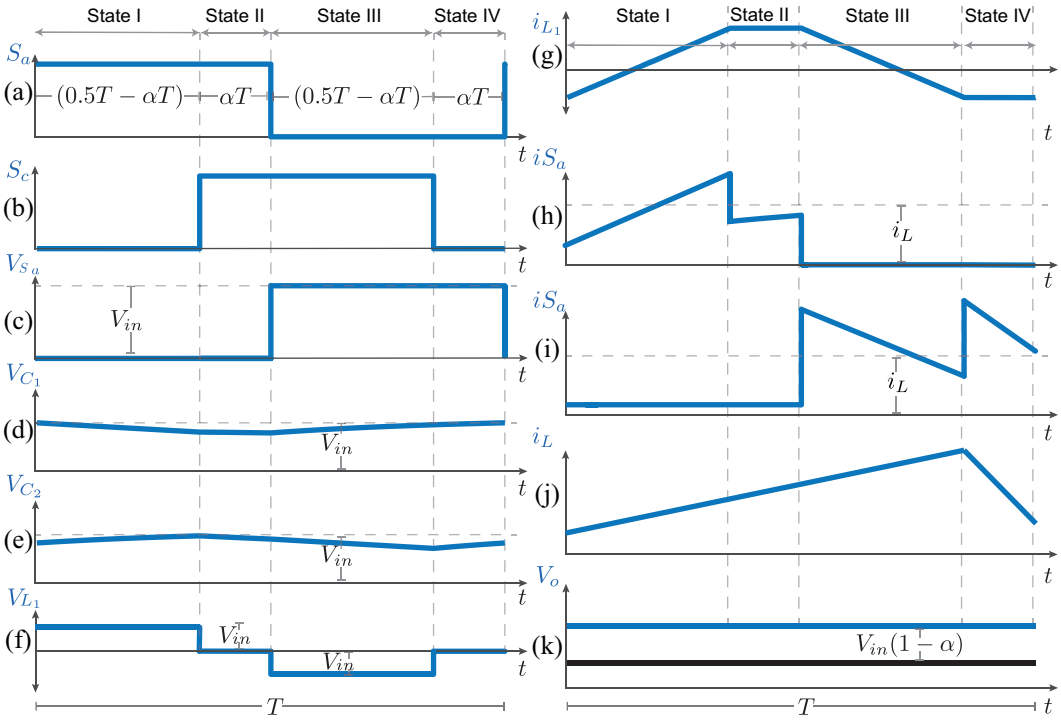

Figure 3.6: Steady-state operation waveforms: a) S_a switching signal; b) S_c switching signal; c) S_a switch voltage; d) C_1 capacitor voltage; e) C_2 capacitor voltage; f) L_1 inductor voltage; g) L_1 inductor current; h) S_a MOSFET current; i) D_a diode curren;. j) Output converter current; k) Input and output converter voltages.

in the direction of its voltage as displayed in Figure 3.6 d), hence leading to its discharge. On the other hand, the capacitor C_2 is connected in parallel with the input voltage, and its voltage increases in this state. Next, during state II, both capacitors are connected in parallel, and this arrangement is also connected in

series with the input. Since the input current is divided through these capacitors, during this state both capacitors reduce their voltages. When state III is generated, the capacitor C_1 is charged while the capacitor C_2 is discharged, which is the opposite operation of the aforementioned state I. Finally, state IV connects the input source and both capacitors in parallel, resulting in both increasing their voltage. Conversely, Figures. 3.6 f) and 3.6 g) show the voltage and current in the impedance network inductor L_1 respectively. It can be observed that for state I, the voltage applied is the same as the input voltage V_{in}, making its current to increase during this interval. Then, the generation of states II and IV result in a zero voltage applied to L_1 and thus its current will be kept constant. Then, during state III, the voltage applied is the negative of the input voltage V_{in}, making its current to decrease accordingly. Following that, Figure 3.6 h) displays the current flowing through the MOSFET S_a. It can be seen that it is conducting in both states in which its gate signal is on. MOSFETs must be able to handle a current that is larger than the output current of the converter, which is determined by the alpha displacement factor. The other MOSFETs drive a similar current with the corresponding phase shift according to the operation of a voltage-fed FB. Now, the current driven by the diodes of the system is represented in Figure 3.6 i), which displays the current through the diode D_a. The operation of the converter will lead to the output current converter measured at the output inductor L, presented in Figure 3.6 j). An important detail to consider is that, despite the similarity with conventional PPCs, the output signals do not have twice the switching frequency. Finally, Figure 3.6 k) shows the input voltage and output voltage of the converter, where the boost property of the converter can be observed.

3.2.3 Converter modeling

The state space equations of the system are shown in equations (3.22) to (3.24). However, this model has the problem of being a non-linear and time-varying system, which makes its analysis complex. In order to perform an easier analysis of the system the state-space averaging is used, this basic approximation allows to remove the HF switching ripple by averaging over one switching period. Nevertheless, the average value can vary from one switching period to the next, such that LF variations are modeled. Therefore, HF information such as ripple and switching transients is lost using the averaged model, but LF dynamic information is preserved, which is useful for designing the control of the converter. Another advantage of the average state-space model is a time invariant system which allows it to be linearized at a operation point. To facilitate obtaining each of the equations in the four states of operation.

The switching ripples in the inductor current and capacitor voltage waveforms are removed by averaging over one switching period. The LF components of the inductor and capacitor waveforms are modeled, calculating the average value over

a switching period, according to:

$$\bar{x}(t) = \frac{1}{T}\int_{t}^{t+T} x(\tau)\cdot d\tau, \tag{3.9}$$

where $\bar{x}(t)$ is the average of $x(t)$ over a switching period T.

Grouping the state-equations equations for the voltage in the inductor L results:

$$V_L = L\frac{di_L}{dt}\begin{cases} V_{in}+V_{C_1}-V_o & \text{Switching state I} \\ V_{in}+V_{C_1}-V_o & \text{Switching state II} \\ V_{in}+V_{C_2}-V_o & \text{Switching state III} \\ V_{in}-V_o & \text{Switching state IV} \end{cases} \tag{3.10}$$

The state-space large-signal average equation for the output inductor voltage can be derived as:

$$\begin{aligned} L\frac{d\bar{i}_L}{dt} &= (0.5-\alpha)(\bar{V}_o-\bar{V}_{C_1}-V_{in})+\alpha(\bar{V}_o-\bar{V}_{C_1}-V_{in}) \\ &\quad +(0.5-\alpha)(\bar{V}_o-\bar{V}_{C_2}-V_{in})+\alpha(\bar{V}_o-\bar{V}_{C_1}) \end{aligned} \tag{3.11}$$

The output capacitor current state-space average equation is:

$$C_o\frac{d\bar{V}_o}{dt} = \bar{i}_L - \bar{i}_o \tag{3.12}$$

For simplification purposes, the following hypothesis is considered:

$$\bar{V}_{C_1} = \bar{V}_{C_2} = V_{in}. \tag{3.13}$$

Rewriting (3.11) results in:

$$L\frac{d\bar{i}_L}{dt} = \alpha(\bar{V}_o - V_{in}) + (\bar{V}_o - 2V_{in})(1-\alpha) \tag{3.14}$$

Considering the system in steady-state operation, i.e. $\dfrac{d\bar{i}_L}{dt} = 0$, the input-to-output transfer function of the system is obtained, as follows:

$$\frac{\bar{V}_o}{V_{in}} = 2-\alpha \tag{3.15}$$

From (3.15) it is clear that the converter is capable of boosting the voltage between a factor of 1.5 and 2 depending on the phase shift α. The converter gain as

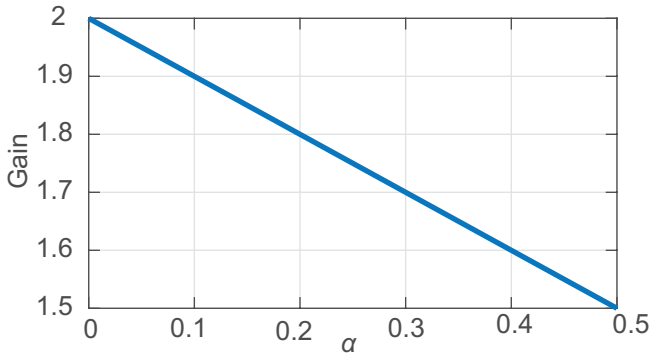

Figure 3.7: Gain of the proposed converter as a function of the phase shift α.

a function of the phase shift α is shown in Figure 3.7.

From (3.11) and (3.12) it is possible to develop a model that allows the design the converter controllers by linearizing them. A small-signal model around a quiescent operating point can be obtained through the perturb and observe technique. This approach was chosen due to its simplicity, which enabled the development of a mathematical model that accurately reflects the converter [55]. As a result, designing controllers becomes simpler, enhancing the system ability to withstand noise or disturbances. It is worth noting that there are a variety of linearization techniques that are also effective for this purpose.

A small disturbance $\hat{x}(t)$ is added to the input signals V_{in} and α, expecting that the other variables also present a small variation. Obtaining mainly the following equations:

$$\begin{aligned} \bar{V}_{in}(t) &= V_{in} + \hat{v}_{in}(t) \\ \alpha(t) &= A + \hat{\alpha}(t) \\ \bar{i}_L(t) &= I_{in} + \hat{i}_L(t) \\ \bar{V}_o(t) &= V_o + \hat{v}_o(t) \end{aligned} \tag{3.16}$$

Considering that the disturbances are very small compared to the signals, i.e., $|\hat{v}_{in}(t)| << |V_{in}|$, $|\hat{\alpha}(t)| << |A|$, $|\hat{i}_L(t)| << |i_L|$ and $|\hat{v}_o(t)| << |V_o|$, equation (3.14) and (3.12) can be written as follows:

$$\begin{aligned} L\frac{d\hat{i}_L(t)}{dt} = &\Big(A + \hat{\alpha}(t)\Big)\Big(V_o + \hat{v}_o(t) - \big(V_{in} + \hat{v}_{in}(t)\big)\Big) \\ &+ \Big(A' - \hat{\alpha}(t)\Big)\Big(V_o + \hat{v}_o(t) - 2\big(V_{in} + \hat{v}_{in}(t)\big)\Big) \end{aligned} \tag{3.17}$$

$$C\frac{d\hat{V}_o(t)}{dt} = \big(I_L + \hat{i}_L(t)\big) - \frac{\big(V_o + \hat{v}_o(t)\big)}{R_{eq}}, \tag{3.18}$$

where $A' = (1 - A)$ and R_{eq} represents the equivalent output load.

Simplifying (3.17) and (3.18), three types of terms are distinguished. The first corresponds to multiplications of the constant terms, which equals zero around the quiescent operating point. The seconds correspond to the second-order terms, composed by multiplying the small disturbance signals among themselves; these being very small, can be neglected. These assumptions reduce the aforementioned equations to only their linear terms, resulting in the following.

$$L\frac{d\hat{i}_L(t)}{dt} = \hat{\alpha}V_{in} + (A - 2)V_{in} + V_o \tag{3.19}$$

For the output capacitor:

$$C\frac{d\hat{V}_o(t)}{dt} = \hat{i}_L(t) - \frac{\hat{v}_o(t)}{R_{eq}} \tag{3.20}$$

Solving equations (3.19) and (3.20) using Laplace transform, and the parameters obtained of the pasive components sizing of the converter (refer to Table 4.1 in Chapter 4), the resulting output to control transfer function is obtained:

$$\frac{V_o}{\alpha} = \frac{1.558s + 24.34}{0.7303s^2 + 23.1s - 38950} \cdot 10^5 \tag{3.21}$$

This equation is a transfer function used to design the controller for the proposed impedance network PPC in the next chapter.

3.2.4 Partial power operation analysis

The partial power ratio K_{pr} of the proposed converter varies depending on the voltage gain G_v of the converter, as shown in Figure 3.8. This value shows the proportion of power handled by the converter, the remaining fraction is directly supplied to the battery. Figure 3.8 shows the particular case for the converter proposed in this article; the maximum gain value of the converter corresponds to $G_v = 2$, a value for which the partial power ratio reaches 50%, for Type I PPC, for the minimum gain value of the converter, $G_v = 1.5$ the partial power ratio reaches 33%. Hence, the proposed converter is capable of feeding the load with full power, while processing

only a fraction of it. Several PPC applications have operating points at which the level of the bias ratio is in similar ranges [24, 135–137]. Figure 3.8 also shows the behavior of a Type II PPC in the same operating range. It can be seen that within the entire operating range the partial power ratio for a Type II PPC is higher than for a Type I PPC, that is, the power that the Type II converter will handle is higher, so choosing a Type I converter is better suited for this application.

3.3 Proposed wide output range buck-boost impedance network converter

As the EV sector progresses, there is a trend towards utilizing HV battery systems in new car models. Presently, a variety of EV models are available with batteries operating at diverse voltage levels (refer to Table 1.1). Consequently, the demand for chargers that can accommodate the various voltage requirements of EV batteries has led to the creation of wide output voltage chargers.

Various wide output voltage EV battery charger topologies can be found in the literature. However, some of these configurations are designed to allow battery charging within the voltage range of 100 V to 500 V, which in this study are referred to as LV systems [140, 141]. These chargers are primarily designed for on-board use, which enables the manufacturer to select a battery with a voltage level within the specified range. On the other hand, some topologies have a broader voltage range at their output; for instance, the topology described in [139] enables battery charging within a range of 100 V to 1100 V. Among the commonly employed DC-DC converter configurations to achieve a wide voltage range, those that utilize LLC resonant converters are notable [139, 144, 145]. Table 3.2 provides a summary and comparison of various wide-range chargers identified in the literature.

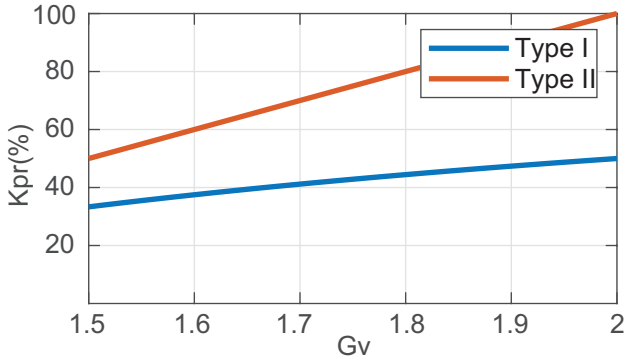

Figure 3.8: Partial power operation in Type I and Type II PPCs for G_v in the range 1.5 - 2.

Table 3.2: Wide output voltage range DC-DC converters.

Topology	Power (kW)	Range(V)	Efficiency(%)	Reference
Buck-Boost	100	400-1000	–	[138]
LLC Resonant	33	100-1100	–	[139]
DAB	11	260-460	96.4	[140]
H-bridge	12	120-450	95.8	[141]
LLC Resonant	11	150-1000	97.6	[142]
LLC Resonant	2	400-800	90.2	[143]
LLC Resonant	10	200-1000	97.95	[144]
LLC Resonant	20	50-650	97	[145]

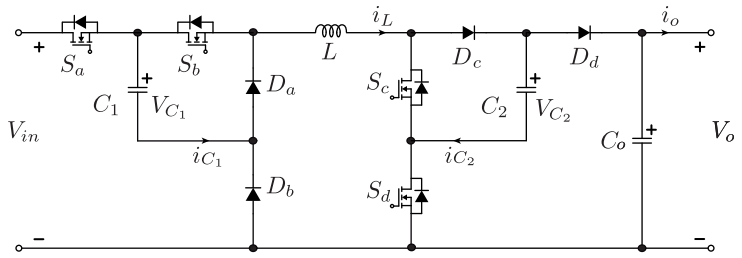

Figure 3.9: Proposed dual impedance network buck-boost DC-DC converter.

This segment introduces a novel dual impedance network buck-boost DC-DC converter designed for a wide output voltage range. The converter is also highly efficient, and it can operate in both step-up and step-down voltage modes, utilizing fewer semiconductors than other step-up and step-down configurations [146].

3.3.1 Topology description

The proposed dual impedance network buck-boost DC-DC converter is designed to operate as a transformerless DC-DC regulation stage for a fast charging station for EV batteries. The converter is based on the conventional topology of buck and boost converters. However, in each scenario, the central point between the two switches is connected through a capacitive impedance network to the central point of the diodes, as illustrated in Figure 3.9. The two configurations are interconnected via a single inductor. A key advantage of this novel converter is that it preserves the linear attributes of conventional boost and buck converters, meaning, the voltage at their output is directly proportional to the variations of the duty cycle in the

switching signals of active semiconductors.

Depending on the operational status, whether it is in boost or buck mode, the voltages V_{C1} and V_{C2} across the capacitors C_1 and C_2 respectively are connected in series with both the input voltage and the voltage across the inductor L. The converter employs pulse width modulation (PWM) to manage the active semiconductors switching. The duty cycle has the capacity to fluctuate within the operational range from 0 to 1. When the converter operatre in buck mode, the duty cycle in the semiconductors S_a and S_b fluctuates, which enables the control of voltage and current at its output, In this operating state, the semiconductors S_c and S_d stay deactivated, meaning, they do not permit any current to pass through them. For operation in boost mode, the variation in the duty cycle, which enables the management of the converter output signals, affects the semiconductors S_c and S_d, however, the semiconductors S_a and S_c remain constantly active. The converter utilizes the inductor L to regulate the voltage and current at its output, regardless of the operating state, thus facilitating the implementation of the charging algorithm employed by the BMS.

Figure 3.10 show the main steady-state operation waveforms of the proposed converter for the buck operation mode through a switching cycle. Variation in the duty cycle leads to the creation of three distinct operational states within each switching cycle, thus partitioning the waveform analysis into an equivalent number of segments. The switching signals for the semiconductors S_a and S_b are depicted in subfigures a) and b) respectively, corresponding to a specific duty cycle δ. Subfigure b) illustrates the signal waveform for the output voltage of the converter.

The current waveform of the inductor is displayed in subfigure d), the inductor is charged when either signal, S_a or S_b is set in on position. Finally, subfigures e) and f) depict the current and voltage waveforms in the capacitor C_1. In a steady state, the voltage of the capacitor always equals half the input voltage value. It is also observed that each time the semiconductor S_a is activated, the capacitor charges as the current flows from the positive to the negative terminal. In contrast, when the semiconductor S_b is activated, the current flows in the opposite direction, causing the capacitor to discharge.

The similar set of operational states waveforms of the proposed converter through a switching cycle, in boost mode operation, are shown in Figure 3.11. The switching signals for semiconductors S_c and S_d are depicted in subfigures a) and b), this signals change in response to variations in the duty cycle d in the boost operation mode. The waveform of the output voltage, depicted in subfigure c).

The current waveform of the inductor is depicted in Subfigure d). The other

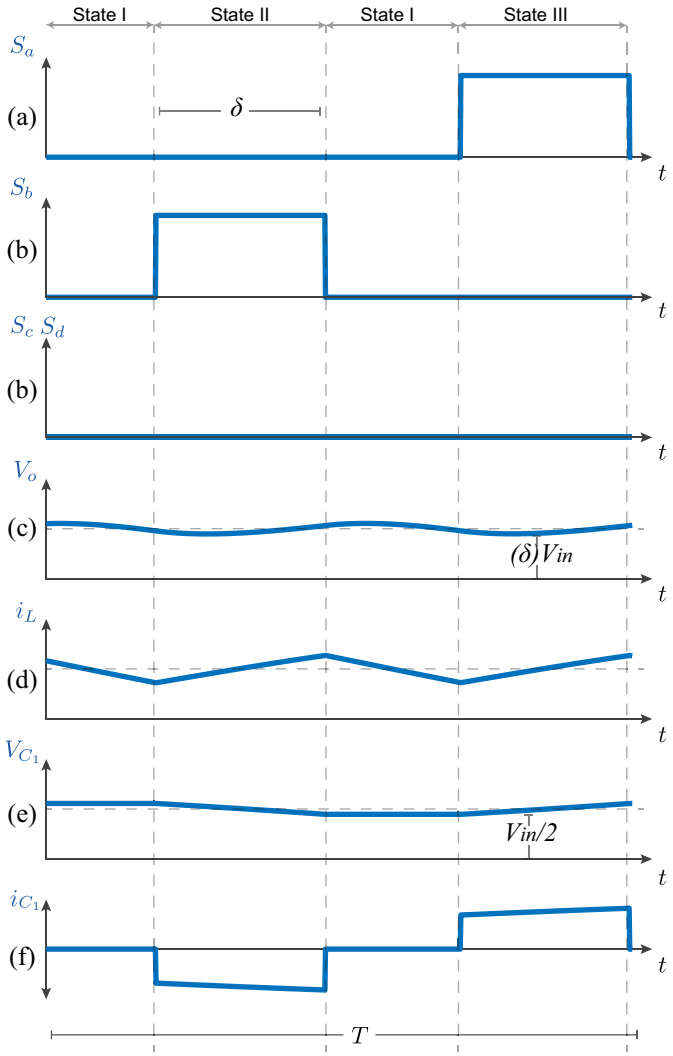

Figure 3.10: Steady-state operation waveforms of the proposed converter in buck mode: a) S_a switching signal; b) S_b switching signal; c) V_o output voltage; d) L inductor current; e) C_1 capacitor voltage; f) C_1 capacitor current.

two signals, shown in subfigures e) and f), represent the voltage and current in the capacitor C_2 respectively.The capacitor voltage is always set to a level that is equal to half of the output voltage. The capacitor is charged when the semiconductor S_d is activated and discharges when S_c is left activated, the flow of the current is a result of the capacitor going through cycles of charging and discharging.

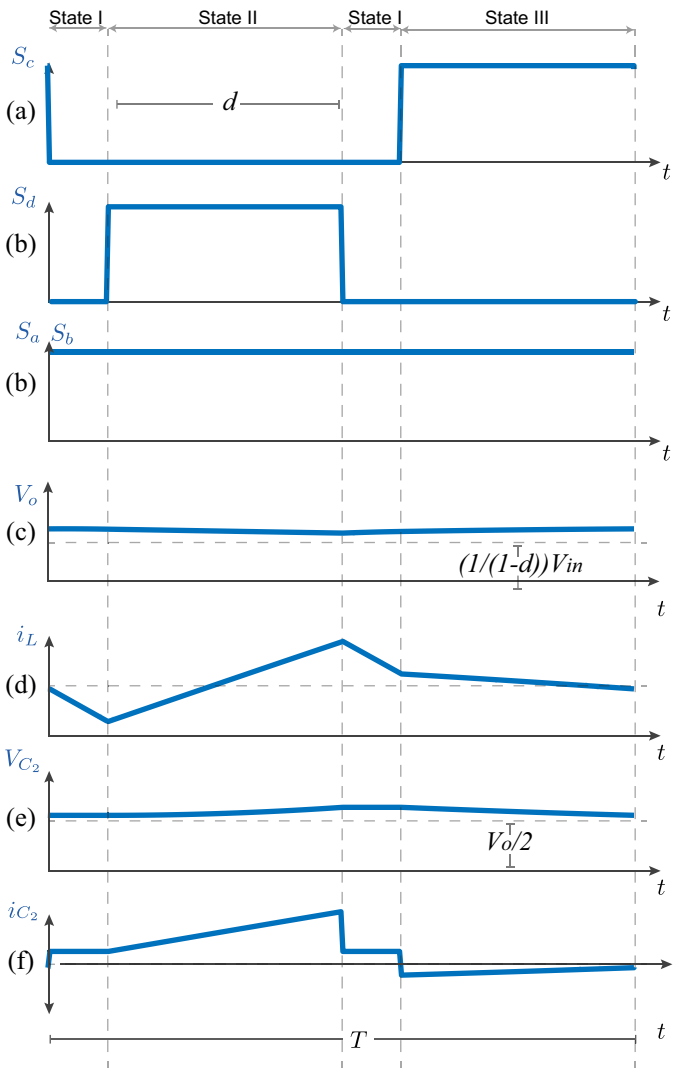

Figure 3.11: Steady-state operation waveforms of the proposed converter in boost mode: a) S_c switching signal; b) S_d switching signal; c) V_o output voltage; d) L inductor current; e) C_2 capacitor voltage; f) C_2 capacitor current.

3.3.2 Operation principle

The proposed converter has a total of six switching states, three in buck mode and three in boost mode, this switching states are obtained by the switching signals in the semiconductors.

Buck operation mode, switching state I (Sa, Sb, Sc, Sd) = (0, 0, 0, 0)

During the buck operation mode switching state I, as depicted in Figure 3.12 a), both switches S_a and S_b remain deactivated, preventing any current from passing through the capacitor C_1 and also disconnect the input voltage. The current flow occurs through diodes D_a and D_b . According to Figure 3.12(a), the state variables equations that can be derived for the third state are:

$$\begin{aligned} C_1\frac{dV_{C_1}}{dt} &= 0 \\ C_2\frac{dV_{C_2}}{dt} &= 0 \\ L\frac{di_L}{dt} &= -V_o \\ C\frac{dV_o}{dt} &= i_L - i_o \end{aligned} \tag{3.22}$$

Buck operation mode, switching state II (Sa, Sb, Sc, Sd) = (0, 1, 0, 0)

During the buck operation mode switching state II, when the control signal at S_a is equal to 0, the input voltage gets cut off, leading to the discharge of the capacitor C_1 through the inductor L in the direction of the output. The functioning of the converter in this state is depicted in Figure 3.12 b). According to this figure, the operation state II of the converter is represented by the following state variable equations:

$$\begin{aligned} C_1\frac{dV_{C_1}}{dt} &= -i_L \\ C_2\frac{dV_{C_2}}{dt} &= 0 \\ L\frac{di_L}{dt} &= V_{C_1} - V_o \\ C\frac{dV_o}{dt} &= i_L - i_o \end{aligned} \tag{3.23}$$

Buck operation mode, switching state III (Sa, Sb, Sc, Sd) = (1, 0, 0, 0)

In the buck operation mode switching state III, depicted in Figure 3.12 c), which corresponds to the buck operation mode, the switches S_c and S_d remain consistently off. Conversely, the activation signals on switches S_a and S_b are $(S_a, S_b) = (1, 0)$. The arrangement of the switches results in the capacitor C_1 being serially connected with the voltages at the input, the inductor L, and the output. According to Figure 3.12 c), the state variable equations for this state are:

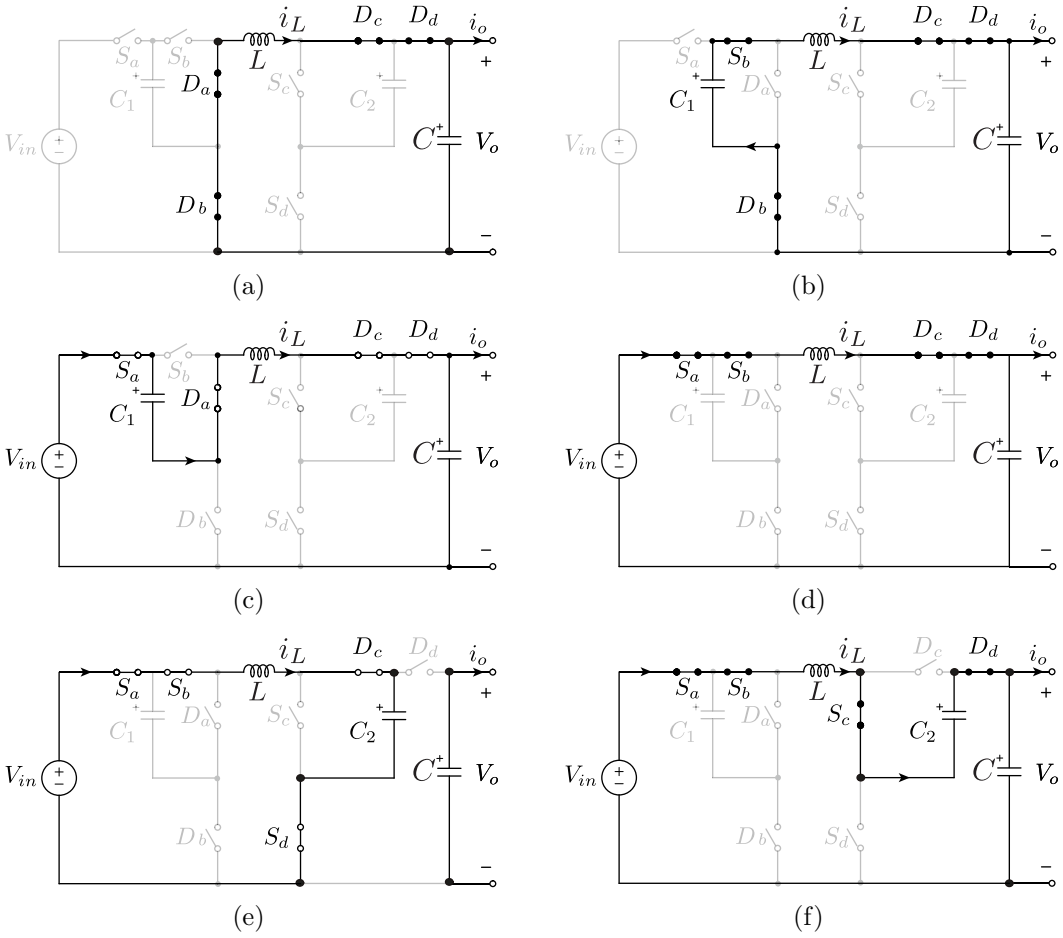

Figure 3.12: Switching states: a) Buck mode state I (Sa, Sb, Sc, Sd) = (0, 0, 0, 0); b) Buck mode state II (Sa, Sb, Sc, Sd) = (0, 1, 0, 0); c) Buck mode state III (Sa, Sb, Sc, Sd) = (1, 0, 0, 0); d) Boost mode state I (Sa, Sb, Sc, Sd) = (1, 1, 0, 0); e) Boost mode state II (Sa, Sb, Sc, Sd) = (1, 1, 0, 1); f) Boost mode state III (Sa, Sb, Sc, Sd) = (1, 1, 1, 0).

$$\begin{aligned} C_1\frac{dV_{C_1}}{dt} &= i_L \\ C_2\frac{dV_{C_2}}{dt} &= 0 \\ L\frac{di_L}{dt} &= V_{in} - V_{C_1} - V_o \\ C\frac{dV_o}{dt} &= i_L - i_o \end{aligned} \tag{3.24}$$

Boost operation mode, switching state I (Sa, Sb, Sc, Sd) = (1, 1, 0, 0)

From this switching state to state VIII, the analysis aligns with the boost operation mode, where switches S_a and S_b are consistently maintained in the on position.

During the Boost operation mode, switching state I, as depicted in Figure 3.12 d), both switches S_c and S_d remain deactivated, preventing any current from passing through the capacitor C_2. The input voltage is connected in a series configuration with the output, through the voltage of the inductor L. According to Figure 3.12 d), the state variables equations that can be derived for the fifth state are:

$$\begin{aligned} C_1\frac{dV_{C_1}}{dt} &= 0 \\ C_2\frac{dV_{C_2}}{dt} &= 0 \\ L\frac{di_L}{dt} &= V_{in} - V_o \\ C\frac{dV_o}{dt} &= i_L - i_o \end{aligned} \tag{3.25}$$

Boost operation mode, switching state II (Sa, Sb, Sc, Sd) = (1, 1, 0, 1)

During Boost operation mode, switching state II, as depicted in Figure 3.12 e), the switch S_c is setting in the off position. This leads to the current in the capacitor C_2 flowing in a positive direction, thereby charging it. Additionally, it can be seen that the input voltage is in series with the voltage on the inductor L and the voltage on the capacitor C_2. The operation state VI of the converter is represented by the following state variable equations:

$$\begin{aligned} C_1\frac{dV_{C_1}}{dt} &= 0 \\ C_2\frac{dV_{C_2}}{dt} &= i_L \\ L\frac{di_L}{dt} &= V_{in} - V_{C_2} \\ C\frac{dV_o}{dt} &= -i_o \end{aligned} \tag{3.26}$$

Boost operation mode, switching state III (Sa, Sb, Sc, Sd) = (1, 1, 1, 0)

The final switching state examined is when switch S_c is activated and switch S_d is deactivated. This setup enables the series connection of the converter input voltage, the inductor L voltage, the capacitor C_2 voltage, and the converter output.

Table 3.3: Wide output range dual impedance network converter switching states.

S_a	S_b	S_c	S_d	V_{S_a}	V_{S_b}	V_{S_c}	V_{S_d}	V_{C_1}	V_{C_2}	V_L
0	0	0	0	$V_{in}/2$	$V_{in}/2$	$V_o/2$	$V_o/2$	$V_{in}/2$	$V_o/2$	$-V_o$
0	1	0	0	$V_{in}/2$	0	$V_o/2$	$V_o/2$	$V_{in}/2$	$V_o/2$	$V_{in}/2 - V_o$
1	0	0	0	0	$V_{in}/2$	$V_o/2$	$V_o/2$	$V_{in}/2$	$V_o/2$	$V_{in}/2 - V_o$
1	1	0	0	0	0	$V_o/2$	$V_o/2$	$V_{in}/2$	$V_o/2$	$V_{in} - V_o$
1	1	0	1	0	0	$V_o/2$	0	$V_{in}/2$	$V_o/2$	$V_{in} - V_o/2$
1	1	1	0	0	0	0	$V_o/2$	$V_{in}/2$	$V_o/2$	$V_{in} - V_o/2$

The converter operating in this switching state is depicted in Figure 3.12 f). The operation state VIII of the converter is represented by the following state variable equations:

$$\begin{aligned} C_1\frac{dV_{C_1}}{dt} &= 0 \\ C_2\frac{dV_{C_2}}{dt} &= -i_L \\ L\frac{di_L}{dt} &= V_{in} + V_{C_2} - V_o \\ C\frac{dV_o}{dt} &= i_L - i_o \end{aligned} \tag{3.27}$$

The state equation found in each switching state is then used to obtain the mathematical model of the converter. Table 3.3 shows the voltage value of the semiconductor and the converter passive elements for each switching state for both, buck and boost operation modes.

3.3.3 Converter modeling

For the mathematical modeling of the proposed converter, the identical method outlined in section 3.2.3 is employed, utilizing state-space averaging. This method allows us to overlook of HF information by averaging the signal over a switching period, while preserving the LF information that is crucial for the design of the control. The subsequent analysis is conducted for both modes of operation. Initially, the converter model is introduced in the buck mode, and then the model of the converter in the boost mode is detailed.

3.3.3.1 Buck mode

As per the equation (3.9), $\bar{x}(t)$ is characterized as the mean value of the signal $x(t)$ throughout a switching interval T. By grouping the state equations for the voltage at L during the initial four switching states, which are associated with the buck mode, we derive:

$$V_L = L\frac{di_L}{dt}\begin{cases} -V_o & \text{Switching state I} \\ V_{C_1} - V_o & \text{Switchingstate II} \\ V_{in} - V_{C1} - V_o & \text{Switching state III} \end{cases} \tag{3.28}$$

Taking into account the duration of each switching state within a period T, where δ signifies the duty cycle of the converter operating in buck mode, it follows that:

$$L\frac{d\bar{i}_L}{dt} = (1-2\delta)(-\bar{V}_o) + \delta(\bar{V}_{C_1} - V_o) + (\delta)(\bar{V}_{in} - \bar{V}_{C_1} - \bar{V}_o) \tag{3.29}$$

The output capacitor current state-space average equation is:

$$C_o\frac{d\bar{V}_o}{dt} = \bar{i}_L - \bar{i}_o \tag{3.30}$$

For simplification purposes, the following hypothesis is considered:

$$\bar{V}_{C_1} = \frac{V_{in}}{2} \tag{3.31}$$

Rewriting (3.29) results in:

$$L\frac{d\bar{i}_L}{dt} = (2\delta - 1)(\bar{V}_o) + (2\delta)\Big(\frac{V_{in}}{2} - \bar{V}_o\Big) \tag{3.32}$$

Considering the system in steady-state operation, i.e. $\dfrac{d\bar{i}_L}{dt} = 0$, the input-to-output transfer function of the system is obtained, as follows:

$$\frac{\bar{V}_o}{V_{in}} = \delta \tag{3.33}$$

In an examination of equation (3.33), it can be discerned that the output voltage of the converter in buck mode is proportionally affected by changes in the duty cycle. The development of a model that enables the precise sizing of current and voltage controllers can be derived from equations (3.29) and (3.30). Nonetheless,

before this can be accomplished, it is imperative to linearize the model, a process in which the perturb and observe method is once again employed.

A small perturbation $\hat{x}(t)$ is introduced to the input signals V_{in} and δ, with the anticipation that the remaining variables will exhibit a slight change. This primarily results in the following equations:

$$\begin{aligned} \bar{V}_{in}(t) &= V_{in} + \hat{v}_{in}(t) \\ \alpha(t) &= \Delta + \hat{\delta}(t) \\ \bar{i}_L(t) &= I_{in} + \hat{i}_L(t) \\ \bar{V}_o(t) &= V_o + \hat{v}_o(t) \end{aligned} \tag{3.34}$$

Given that the perturbations are significantly smaller than the signals, that is, $|\hat{v}_{in}(t)| << |V_{in}|$, $|\hat{\delta}(t)| << |\Delta|$, $|\hat{i}_L(t)| << |i_L|$ and $|\hat{v}_o(t)| << |V_o|$, the equations (3.32) and (3.30) can be expressed in the following manner:

$$\begin{aligned} L\frac{d\hat{i}_L(t)}{dt} = &\Big(2\big(\Delta + \hat{\delta}(t)\big) - 1\Big)\Big(V_o + \hat{v}_o(t)\Big) \\ &+ \Big(\Delta + \hat{\delta}(t)\Big)\Big(\big(V_{in} + \hat{v}_{in}(t)\big) - 2\big(V_o + \hat{v}_o(t)\big)\Big) \end{aligned} \tag{3.35}$$

$$C\frac{d\hat{V}_o(t)}{dt} = \big(I_L + \hat{i}_L(t)\big) - \frac{\big(V_o + \hat{v}_o(t)\big)}{R_{eq}}, \tag{3.36}$$

where R_{eq} represents the equivalent output load.

As previously mentioned, terms composed solely of constants equate to zero at the quiescent operating point. Due to their minimal value, second order terms are disregarded, resulting in the following expression upon simplifying (3.35) and (3.36).

$$L\frac{d\hat{i}_L(t)}{dt} = \hat{v}_o(t) + \hat{\delta}(t)(V_{in}) + \Delta(\hat{v}_{in}(t)) \tag{3.37}$$

For the output capacitor:

$$C\frac{d\hat{V}_o(t)}{dt} = \hat{i}_L(t) - \frac{\hat{v}_o(t)}{R_{eq}} \tag{3.38}$$

Solving equations (3.37) and (3.38) using Laplace transform, and the parameters obtained of the pasive components sizing of the converter (refer to Table 4.2 in Chapter 4), the resulting output to control transfer function is obtained:

$$\frac{V_o}{\alpha} = \frac{1}{7.4e^{-11}s^2 + 2.89e^{-8}s - 1.8e^{-3}} \tag{3.39}$$

Equation (3.39) is the transfer function used in the following chapter for the converter control design, in the buck operation mode.

3.3.3.2 Boost mode

Grouping the state equations for the voltage at L during the final four switching states, which are associated with the boost mode, we derive:

$$V_L = L\frac{di_L}{dt} \begin{cases} -V_o & \text{Switching state I} \\ V_{in} - V_{C2} & \text{Switching state II} \\ V_{in} + V_{C2} - V_o & \text{Switching state III} \end{cases} \tag{3.40}$$

Taking into account the duration of each switching state within a period T, where γ signifies the duty cycle of the converter operating in boost mode, results:

$$L\frac{d\bar{i}_L}{dt} = (1-2\gamma)(-\bar{V}_o) + d(\bar{V}_{in} - V_{C2}) + \gamma(\bar{V}_{in} - \bar{V}_{C_2} - \bar{V}_o) \tag{3.41}$$

The output capacitor current state-space average equation is (3.30). For simplification purposes, the following hypothesis is considered:

$$\bar{V}_{C2} = \frac{V_o}{2} \tag{3.42}$$

From (3.41) the resulting input to output transfer function in steady-state operation is:

$$\frac{\bar{V}_o}{V_{in}} = \frac{1}{1-\gamma} \tag{3.43}$$

Utilizing the identical perturb and observe method, the computation of the linear model of the converter in its boost mode continues. This process, similar to the one demonstrated for the buck scenario, the following signals altered by a small disturbance are obtained:

$$\begin{aligned} \bar{V}_{in}(t) &= V_{in} + \hat{v}_{in}(t) \\ \gamma(t) &= \gamma + \hat{\Gamma}(t) \\ \bar{i}_L(t) &= I_{in} + \hat{i}_L(t) \\ \bar{V}_o(t) &= V_o + \hat{v}_o(t) \end{aligned} \tag{3.44}$$

The resulting equations are obtained:

$$L\frac{d\hat{i}_L(t)}{dt} = \big(\Gamma - 1\big)\hat{v}_o(t) + \hat{\gamma}(t)\big(V_o + 2V_{in}\big) + 2\Gamma\big(\hat{v}_{in}(t)\big) \tag{3.45}$$

$$C\frac{d\hat{V}_o(t)}{dt} = \big(I_L + \hat{i}_L(t)\big) - \frac{\big(V_o + \hat{v}_o(t)\big)}{R_{eq}} \tag{3.46}$$

Solving equations (3.45) and (3.46), using Laplace transform, and the parameters obtained of the components sizing of the converter (refer to Table 4.2 in Chapter 4), the resulting output to control transfer function is obtained:

$$\frac{V_o}{\gamma} = \frac{1}{1.90e^{-11}s^2 + 7.51e^{-9}s} \tag{3.47}$$

Equation (3.47) is the transfer function used in the following chapter for the converter control design, in the boost operation mode.

3.4 Conclusion

This chapter introduced two new impedance network PPCs, through a mathematical development of each of the operating states of each converter. The deductions were made through an analysis using the state-space averaging technique, obtaining the output to input transfer functions, and the output-control transfer function. The latter function will facilitate the control design that will be discussed in the next chapter. Additionally, the dimensions of the passive components for both converters will be outlined below, accompanied by the simulation results for each proposed converter.

Chapter 4

SIMULATION RESULTS

FOLLOWING the introduction of the theoretical analysis of the converters presented in the previous chapter, the following sections provide an analysis of the sizing of the passive components for each converter, along with a comprehensive overview of the controllers employed in each topology. The validation of the converters through simulation is presented in the end of each section.

4.1 Impedance network type I partial power converter

4.1.1 Component sizing

The capacitor charge balance is used to determine the size of capacitors C_1 and C_2 on the impedance network of the DC-DC converter. The defining equation of a capacitor, where $i_c(t)$ and $v_c(t)$ are the current and voltage of the capacitor, is:

$$i_c(t) = C\frac{dv_c(t)}{dt} \tag{4.1}$$

Integration of this equation over one switching period T yields:

$$v_c(T) - v_c(0) = \frac{1}{C}\int_0^T i_c(t)dt \tag{4.2}$$

In steady state, the net change over one switching period of the capacitor voltage must be zero, so that the left-hand side of equation (4.2) is equal to zero. Therefore, in equilibrium the integral of the capacitor current over one switching period should be zero. Considering a steady-state analysis and establishing the principle of load balance, the following equation can be reached:

$$C = \frac{V_{CX}}{2\Delta vR}\alpha_{max}T, \tag{4.3}$$

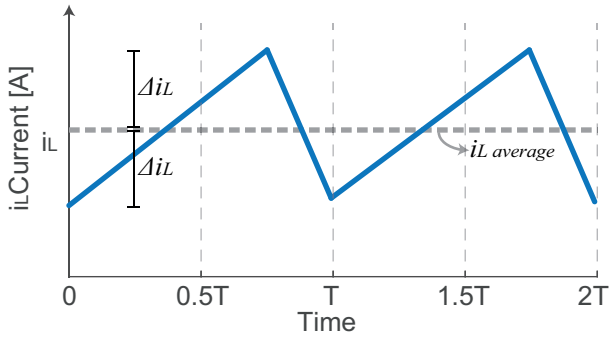

Figure 4.1: Output inductor waveform

where V_{CX} is the voltage in capacitors C_1 or C_2, $2\Delta v$ is the capacitor ripple, and α_{max} is the maximum PS, R represents the equivalent load resistance, and T is the switching period.

Considering a ripple of 1% of the total capacitor voltage, the maximum PS $\alpha = 0.5$, the capacitor voltage equal to the input voltage (400 V), a switching frequency of 20 kHz, and an 64 Ω equivalent resistance, considering a 10 kW station, results:

$$C_X = 78.1\ \mu F \tag{4.4}$$

In order to determine the size of the output inductor L [55], the waveform of the converter output current is taken into account, as depicted in Figure 4.1.

According to equations (3.22), (3.23), (3.7) and without considering the internal dynamics of the converter, the slope of the output inductor current is the same for the first three operating states, i.e, for $0 < t < T - \alpha$. In this time interval the amplitude of the current changes by a value of $2\Delta i_L$, expressed in the equation (4.5).

$$2\Delta i_L = \frac{V_{in} + V_{C1} - V_o}{L}(1 - \alpha)T \tag{4.5}$$

For values of $V_{in} = 400$ V, $\alpha = 0.25$, $\Delta i_L = 1$ A, $V_o = 700$ V and the switching frequency 20 kHz, it results:

$$L = 1800\ \mu H, \tag{4.6}$$

For L_1 considering the wave form shown in Figure 4.2.

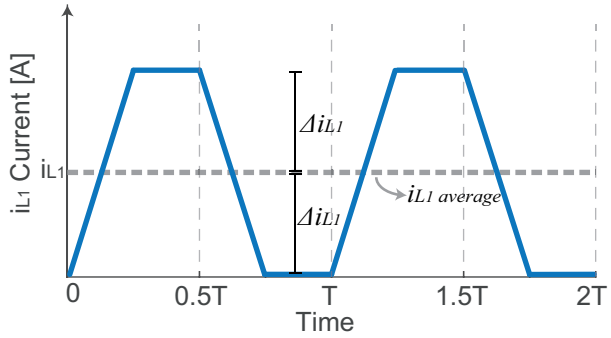

Figure 4.2: L1 inductor waveform

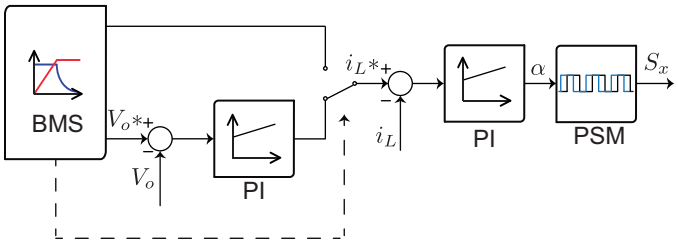

Figure 4.3: CC-CV control scheme.

With an analysis similar to that carried out in (4.5), the equation 4.7 is obtained for L_1.

$$2\Delta i_{L_1} = \frac{V_{in}}{L_1}(0.5 - \alpha)T, \tag{4.7}$$

for the same values used for L, and $\Delta i_{L_1} = 1$ A results:

$$L_1 = 2500\ \mu H \tag{4.8}$$

4.1.2 Control scheme

4.1.2.1 Controllers design

A conventional cascaded control scheme is used to regulate the charging process of the battery, as shown in Figure 4.3. The external proportional integrator (PI) controller is responsible for regulating the output voltage of the converter, while the internal PI controller is used to regulate the output current. The cascade control scheme can be bypassed to a single output current control loop to implement the CC-CV charging algorithm [147]. During the first stage of the charging process, the reference for the internal current controller is set to a constant value indicated

by the BMS, so that the charging station can operate at battery nominal current, hence no external voltage control loop is needed and is therefore bypassed. As soon as the battery voltage reaches a value predetermined by the BMS (usually a value associated with a range between 80% - 90% of the SoC of the battery), the current reference changes, from the constant value to the output of the PI voltage controller, for which the outer control loop is engaged. During this stage of the charging process, the battery itself determines how much current is required to complete the charge without incurring in damaging over-voltages. Regardless of the operating mode, the output of the current controller corresponds to the phase shift α, the same one that, through a PSM, generates the gating signals for the semiconductors of the proposed converter.

Let $\Upsilon(s)$ be the total transfer function through the system, also known as the close loop gain, where $G_c(S)$ is the transfer function of the compensator, $1/V_M$ is the PSM amplitude, $G_{vd}(s)$ is the output to control transfer function and $H(s)$ is the voltage sensor gain. The compensator design should allow strict control of the output voltage, i.e., the system must have the ability to maintain a stable voltage reference even in the presence of static or dynamic disturbances. The main cause of these disturbances are fluctuations in the input voltage and output current.

$$\Upsilon(s) = H(s)G_c(s)(1/V_M)G_{vd}(s) \tag{4.9}$$

It can be stated that the design of $\Upsilon(s)$ must be as large as possible. However, the design of $\Upsilon(s)$ is limited by the criteria of stability and quality of the closed loop response.

4.1.2.2 Stability analysis

An special case of the Nyquist criterion stability, know as *Phase Margin Test*. It enables to assess the stability of a closed loop system, as well as to determine its proximity to instability, by analyzing the magnitude and phase response of the close loop gain $\Upsilon(s)$ shown in (4.9).

The phase margin test focuses mainly on three criteria:

- Identify the crossover frequency f_c, which corresponds to the point where the magnitude of $\Upsilon(s)$ equals 1 or 0 dB.
- Identify the phase margin φ_m from $\Upsilon(s)$ as follow:

$$\varphi_m = 180^\circ + \angle T(s) \tag{4.10}$$

Table 4.1: Design parameters

Parmeter	Values	Unit
Input Voltage	200/400	V
Nominal Power	40/160	kW
CC mode	100/200	A
Output Inductor	1800	uH
L1 Inductor	2500	uH
C1 and C2	80	uF
Switching Frequency	20	kHz

- If $\Upsilon(s)$ contains no right hand poles (RHP) and there is exactly one crossover frequency, then $\Upsilon/(1+\Upsilon)$ contains no RHP if the phase margin is positive.

The phase margin test therefore establishes that if:

$$\begin{aligned} \varphi_m > 0^\circ \quad & \text{Stable system} \\ \varphi_m < 0^\circ \quad & \text{Unstable system} \end{aligned}$$

Therefore, the design of the compensator must ensure a positive phase margin for $\Upsilon(s)$. In [55], there is a detailed analysis in which it is established that an acceptable value of φ_m is between 52° and 76°. Furthermore, it should facilitate the reduction of steady state error and enhance the system ability to respond to dynamic changes in input voltage and output current, aiming to achieve the maximum bandwidth possible.

Considering the dimensioning of the components presented in the previous section and the parameters in Table 4.1, the compensator design is carried out. Equation 4.14 is calculated for the proposed converter, taking into account the following:

$$H(s) = 1 \tag{4.11}$$

$$V_M = 1 \tag{4.12}$$

$$G_c(s) = 1 \tag{4.13}$$

On the other hand, the output to control transfer function value for the proposed converter was previously calculated in (3.21). By setting the compensator function $G_c(s) = 1$, the uncompensated closed-loop transfer function, defined as $\Upsilon_u(s)$, is obtained.

$$\Upsilon_u(s) = G_{vd}(s) \tag{4.14}$$

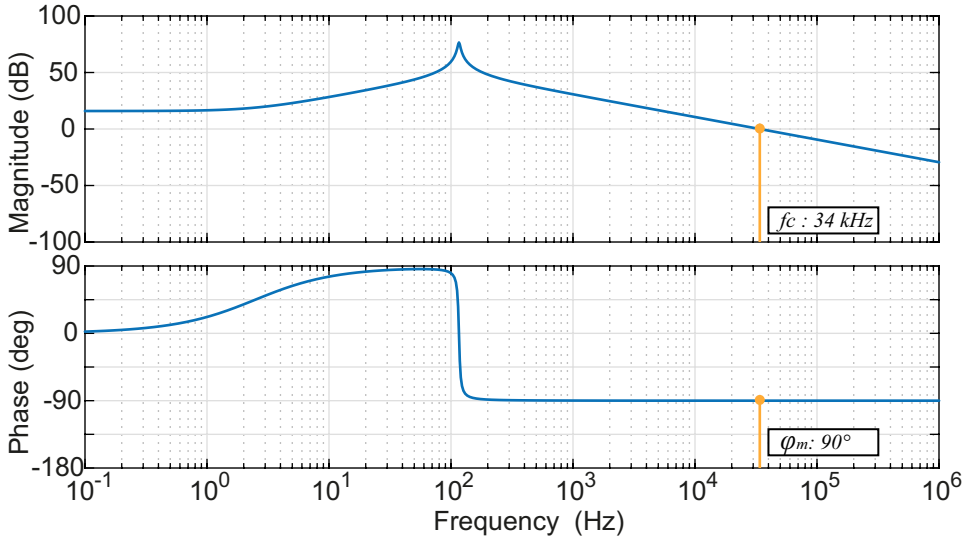

Figure 4.4: Uncompensated close-loop $\Upsilon_u(s)$ Bode plot

$$T_u(s) = \frac{1.558s + 24.34}{0.7303s^2 + 23.1s - 38950} \cdot 10^5 \tag{4.15}$$

According to Figure 4.4, where the magnitude and phase in the Bode plots of $\Upsilon_u(s)$ are shown, the crossover frequency of $\Upsilon_u(s)$ is 34 kHz, a value that is higher than the switching frequency. At this frequency, the phase margin is 90°. However, it is important to note that this value falls outside the recommended range for the phase margin, which may have an impact on the stability of the system [55].

Hence, it is necessary to appropriately dimension the compensator in order to rectify the output of $\Upsilon_u(s)$, leading to the attainment of the ultimate closed-loop transfer function $\Upsilon(s)$:

$$\Upsilon(s) = G_c(s)G_{vd}(s) \tag{4.16}$$

By utilizing the MATLAB SISOTOOL, we determine the desired parameters for the function $\Upsilon(s)$, specifically a crossover frequency of one-tenth the switching frequency and a phase margin of 52°. The equation 4.18 represents the transfer function of the compensator, which is indicative of a PI controller.

$$G_c(s) = 0.0469(1 + \frac{9490}{s}) \tag{4.17}$$

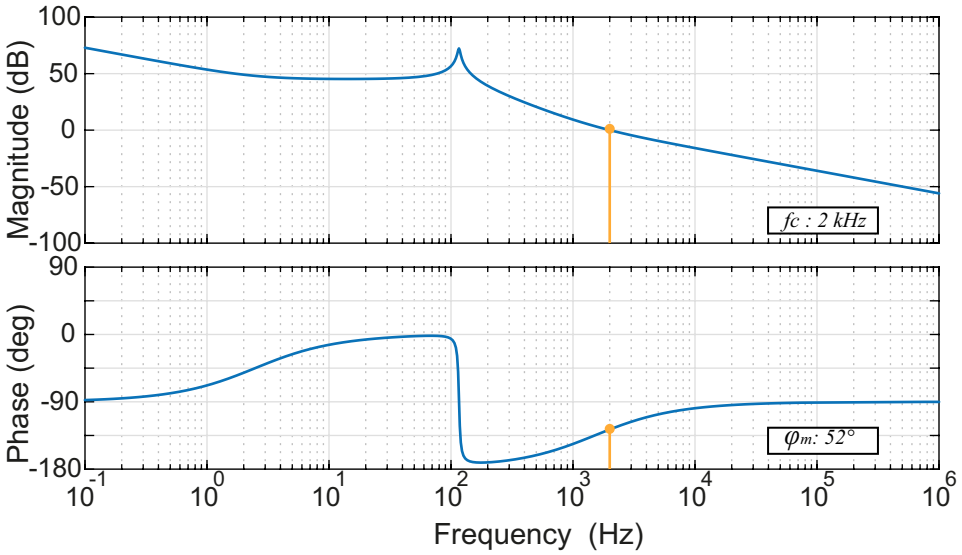

Figure 4.5: Compensated close-loop $\Upsilon(s)$ Bode plot

The bode graph of the closed-loop transfer function of the system, including the PI controller, is depicted in Figure 4.5. The graph illustrates the new crossover frequency point at 2 kHz, which corresponds to one tenth of the switching frequency. Additionally, the phase margin is set at 52°. These values ensure that the system output only responds to changes in the reference voltage and that it remains stable. On the other hand, the PI controller causes a noticeable increase in the function magnitude at LFs, which effectively reduces the steady state error.

A comparable analysis enables the determination of the size of the external voltage PI controller illustrated in Figure 4.3. However, this controller is sized with a bandwidth that is 10 times smaller than the one achieved for the internal PI controller. The resulting equation is presented below:

$$G_{ce}(s) = 2.4937(1 + \frac{23809}{s}) \tag{4.18}$$

4.1.3 Simulation results

Initially, validation of the main waveforms of the converter is introduced for an 800 V charging system, aligned with the designated nominal power of 160 kW, yielding an output current of 200 A and an inputo voltage of 400 V. Figure 4.6 illustrates the main waveforms of the converter, simulated using the PLECS software. The figure

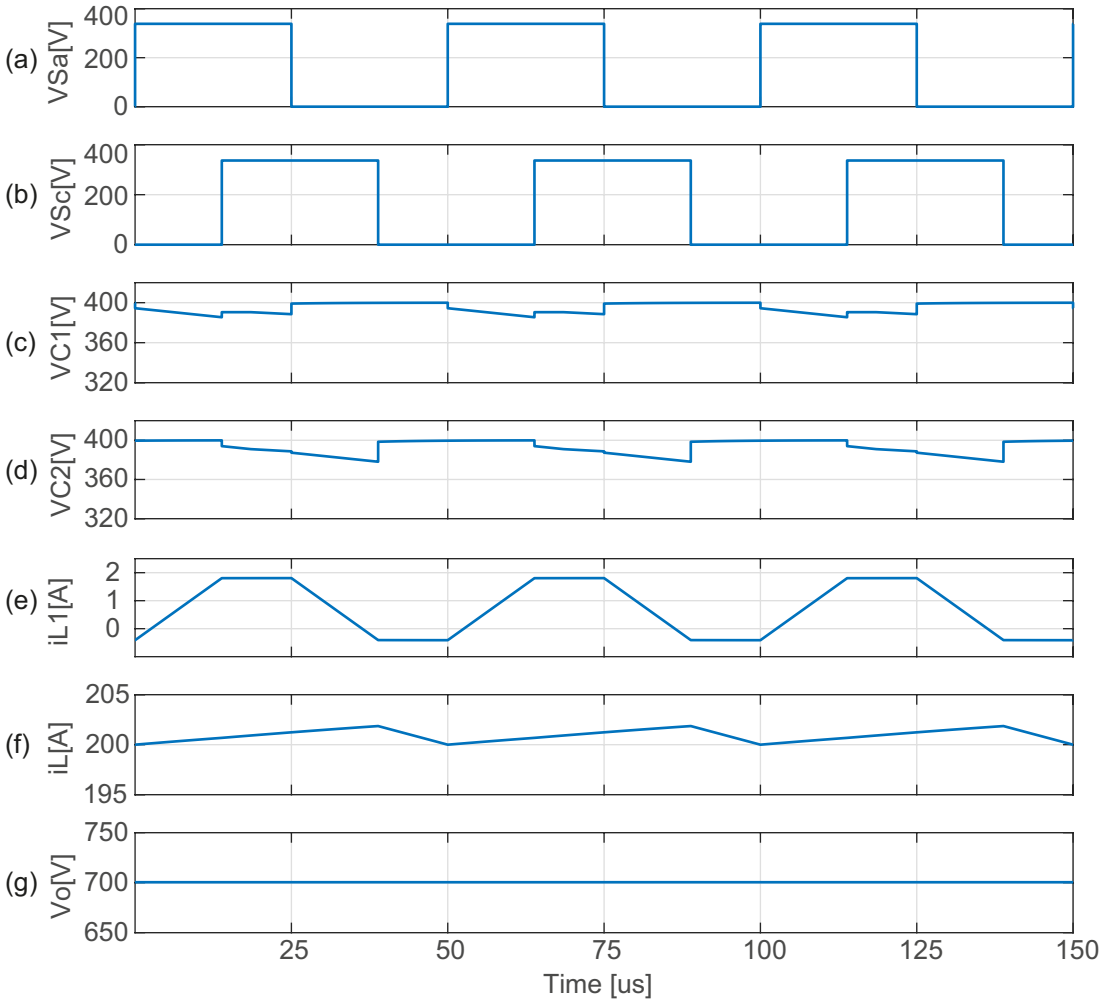

Figure 4.6: Main simulated waveforms of the impedance network type I PPC: a) S_a switch voltage; b) S_c switch voltage; c) C_1 capacitor voltage; d)C_2 capacitor voltage; e) L_1 inductor current; f) L inductor current; g) Converter output voltage

shows the voltage across the semiconductors S_a and S_c, which corresponds to the input voltage in all operational states of the converter. It also emphasizes that the voltage across the capacitors in the impedance network, C_1 and C_2, remains constant at the input voltage level, 400 V for this particular simulation. Additionally, the current waveform through the impedance network inductor L_1 and the output inductor L is depicted, aligning with the waveforms discussed in the preceding chapter. Lastly, the diagram displays the output voltage, which is equivalent to the voltage across a battery connected to the converter.

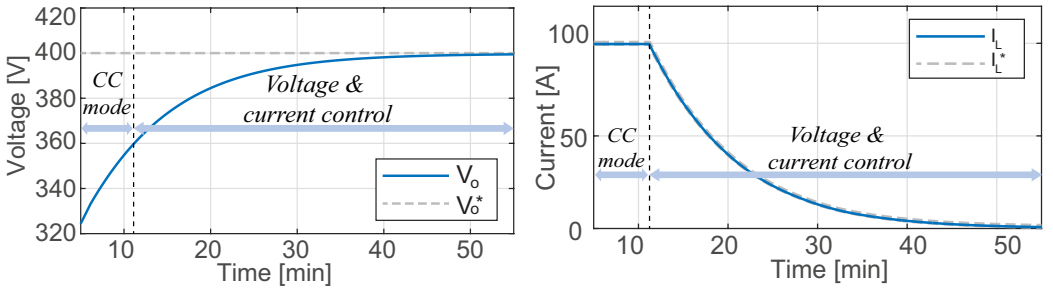

(a) (b)

Figure 4.7: Battery charging process for a 400 V system; a) Output voltage. b) Output current.

In order to perform the charger simulation, a Li-ion battery based on a resistor-only electrical model [148] is used. Where the voltage of the battery V_o is determined as a function of SoC according to equation 4.19.

$$V_o = E_o - K_{ap}(\frac{Q}{Q - it}) + Ae^{-Bit} \tag{4.19}$$

A model of a 60 kWh Li-ion battery is used to simulate the proposed converter as part of a fast charging station for both 400 V and 800 V systems. Table 4.1 shows the parameters used to simulate the DC-DC converter as part of the fast charging station.

Figure 4.7 shows the simulation results for the converter operating as the DC-DC converter of a 400 V fast charging stations. The behavior of the converter is observed according to the CC-CV charging algorithm, this consists of two main stages, the first called CC, where current is supplied steadily until the battery voltage reaches a preset level. The CV stage allows the battery to reach 100% of its capacity without damaging it. In this stage, a voltage is applied between the battery terminals equal to the nominal voltage of the battery. As the battery reaches the desired voltage level, the current gradually decreases to a minimum value.
The battery reaches the 80% of the SoC after around 13 min from the beginning of the charging process at 20% of the SoC. It can also be seen that the charging current follows the CC-CV algorithm. In the CC stage, a current of 100 A is injected into the battery until the battery reaches 80% of its SoC, at which time the algorithm switches to CV mode, where the current gradually decreases to allow the battery to reach its maximum charging voltage.

A simulation over a whole battery charging cycle of a 800 V fast charging station is shown in Figure 4.8. It can be seen that the behavior of the converter follows the

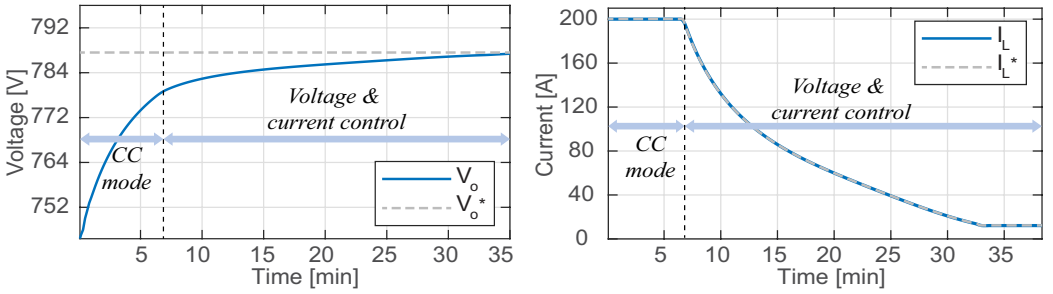

(a) (b)

Figure 4.8: Battery charging process for a 800 V system; a) Output voltage. b) Output current.

CC-CV charging algorithm. Figure 4.16a shows the current injected into the battery during the first five minutes when the charging station is in CC mode. When the battery reaches 80% of its SoC, the BMS changes the current reference so that it is now set by the voltage controller. It can be seen that the CC follows the nominal current of the charger until around 6.5 minutes, the instant in which the current injected into the battery begins to reduce gradually. The charging process continues in a controlled manner until the battery reaches its maximum charge value indicated by the voltage reference of the external CV controller, as shown in Figure 4.16b.

To carry out the efficiency analysis of the converter, the thermal modeling tool of PLECS was used for the C3M0025065D MOSFET and the GD2X20MPS12D diode. Usually, fast charging stations, in order to achieve a higher power rating, implement the DC-DC converter as an interleaved connection of several modules rated somewhere between 10 kW to 30 kW. In this simulation a 10 kW rated converter modules has been considered for the efficiency analysis. The study was carried out considering an operating power range between 1 kW - 10 kW for a 800 V nominal output voltage battery, obtaining the results shown in Figure 4.9. As with other DC-DC converters, the proposed topology can be implemented in an interleaved connection mode across multiple modules to reach higher power levels. This approach not only enhances power quality and reduces inductor sizes but also facilitates scalability to achieve battery chargers with higher power ratings. The interleaved connection can also further increase efficiency.

The estimated efficiency of the proposed converter is quite flat over the tested power range, particularly from half to rated power, and goes from a minimum 97% achieved at low capacity to a peak efficiency of 97.9% when operating at the highest power level. The efficiency of the converter is determined when it is running with a gain of $G_v = 2$, as discussed in earlier sections. This gain results in the converter operating at a 50% of partiality. The flat efficiency curve of the proposed converter

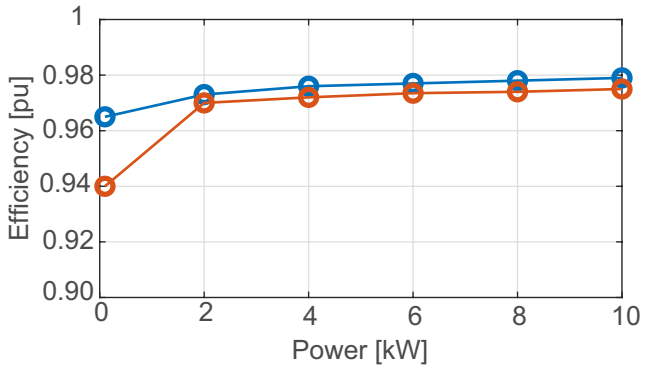

Figure 4.9: Efficiency comparison between impedance network type I PPC (blue) and HF isolated type I PPC (red).

makes it very attractive, since usually only high-peak efficiencies are achieved for a narrow operating range in conventional charging stations. This can have an important impact over the global efficiency over the whole charging process, since usually peak efficiencies are only achieved through brief periods of time.

A comparison of the efficiency between the proposed impedance network type I PPC and the HF isolated type I PPC is illustrated in Figure 4.9. For this comparison, both topologies were evaluated using identical simulation parameters and the PLECS thermal model described previously for the semiconductors. The HF isolated converter achieves a peak efficiency of 97.5% at an operating power of 10 kW, which is less than the 97.9% efficiency of the proposed converter.

4.2 Wide output range buck-boost impedance network converter

4.2.1 Component sizing

In the same way that the value of the capacitors was sized in the impedance network type I PPC, the charge balance capacitor is employed.The relationship between current and voltage in a capacitor is shown in (4.2). Using the same methodology as in section 4.1.1, during steady state, the total variation in the capacitors voltage, throughout a switching cycle, amounts to zero, leading to the subsequent formula for the buck operation mode.

$$C_X = \frac{V_{C1}}{2\Delta v R}\delta_{max} T \tag{4.20}$$

In this context, Δv signifies the maximum expected ripple in the voltage of the capacitor, R stands for the load equivalent resistance, δ_{max} denotes the highest duty cycle, T is a commutation period, and C_{CX} represents the capacitance determined

Table 4.2: Design parameters for wide range impedance network converter.

Parmeter	Values	Unit
Input Voltage	400	V
Nominal Power	160	kW
Nominal current	200	A
Switching Frequency	20	kHz
γ_{max}	1	–
Equivalent resistance	64	Ω
Voltage ripple	1	%
Current ripple	1	%

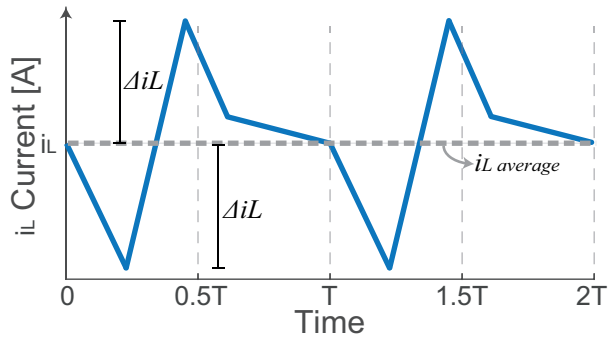

Figure 4.10: Waveform of the inductor converter

for the capacitor under analysis. The parameters values utilized in the computation of the capacitance of C_1 are displayed in Table 4.2. As examined in the previous chapter, the voltage value assigned to V_{C1} is equivalent to half the input voltage.

The value obtained from the equation (4.20) and the data in Table 4.2 yields:

$$C_1 = 40\mu F \tag{4.21}$$

When determining the size of the C_2 capacitor, we refer to the same parameters as in Table 4.2. However, it should be noted that the voltage for the C_2 capacitor is equivalent to half of the output voltage. Nevertheless, the maximum voltage difference that this capacitor can tolerate occurs when the output voltage is at its higher designed level, equivalent to the 1000 V. From this, we derive that the capacitance C_2 is:

$$C_2 = 17\mu F \tag{4.22}$$

The size of the inductor L is calculated by considering Figure 4.10 that displays its waveform. The second switching state shown in the figure, corresponding to the previously mentioned state VI, exhibits the most significant change in the current magnitude. During this period, the current amplitude changes by a factor of $2\Delta i_L$. Using the equation (3.27) that presents the voltage in the inductor, resulting in:

$$2\Delta i_L = \frac{V_{in} - V_{C2}}{L}(\gamma)T \tag{4.23}$$

The obtained value of the inductance L is:

$$L = 1000\mu H \tag{4.24}$$

4.2.2 Control scheme

The control of the wide range impedance network converter is based on a cascade control loop that employs conventional PI controllers. To ensure the correct development of the converter, the parameters of the PI controller are dimensioned for both, buck and boost operation modes separately, as depicted in Figure 4.11.

The output voltage of the converter is regulated by managing the inductor current L. According to the charging algorithm, the BMS defines the reference signals for those control loops, as shown in Figure 4.11. For the control of this converter, the CC-CV charging algorithm is employed. In the begging of the charging process, the BMS sets the current reference, allowing the charging station to function at its standard current. The reference of the inner current controller is maintained until

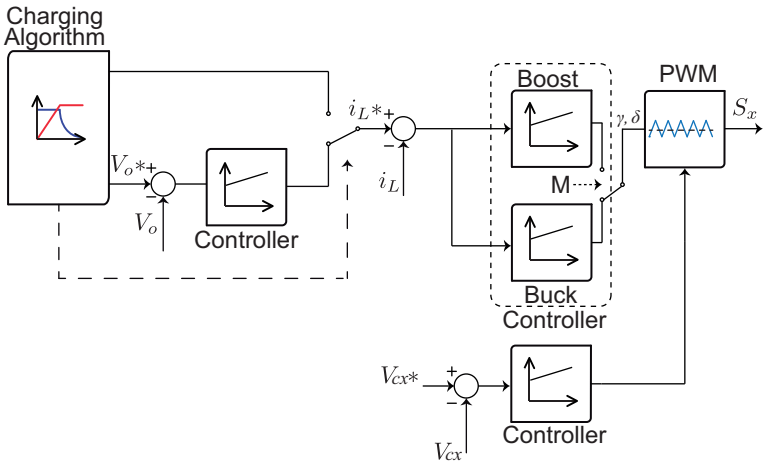

Figure 4.11: Control scheme for the wide range impedance network converter.

the battery reaches a value close to 80% of its SoC, at this point the battery calculates the necessary current for full charge. Consequently, the current controller reference alters the signal from the output of the external voltage controller from this point forward, ensuring the battery voltage remains steady at its nominal value. The external voltage regulator consists of two separate PI controllers. Their operation depends on the converter operation mode, specifically whether it is in buck or boost mode. Each of the capacitors of the proposed converter should be appropriately maintained according to a voltage reference. For this, two independent PI controllers are used. The reference for each capacitor, C_1, and C_2, equals $Vi/2$ and $Vo/2$, respectively [149, 150].

The output signals γ and δ corresponds to the duty cycle signals from the PI controllers for each operation mode, depending on the inverter operating status.

In light of the same principle outlined for the design and stability examination of the converter controller, as depicted in section 4.1.2.1 and 4.1.2.2, the uncompensated closed-loop transfer function for the buck and boost operational modes are:

$$\Upsilon_{ubu}(s) = \frac{1}{7.4e^{-11}s^2 + 2.89e^{-8}s - 1.8e^{-3}} \tag{4.25}$$

$$\Upsilon_{ubo}(s) = \frac{V_o}{\gamma} = \frac{1}{1.90e^{-11}s^2 + 7.51e^{-9}s} \tag{4.26}$$

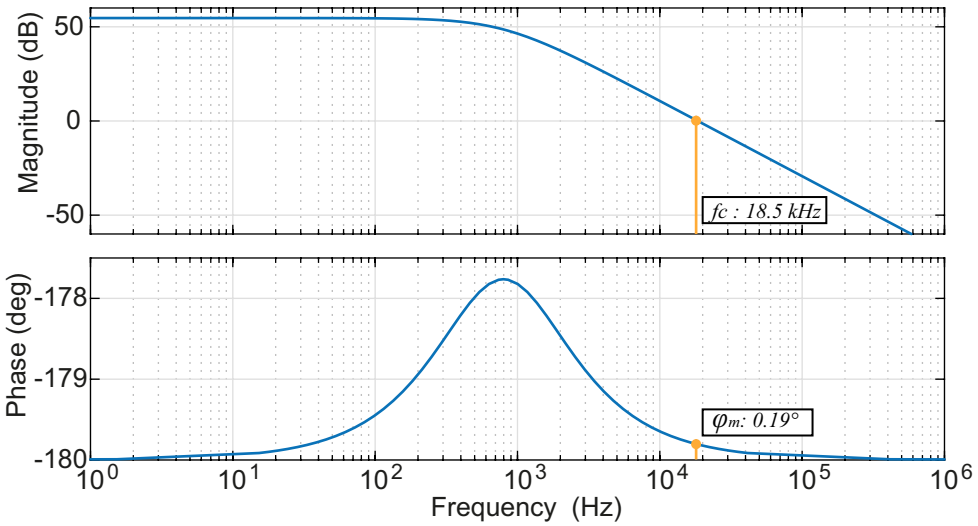

Figure 4.12: Uncompensated close-loop $\Upsilon_{ubu}(s)$ bode plot.

Where $\Upsilon_{ubu}(s)$ represents the uncompensated closed-loop transfer function for the buck operation mode, and $\Upsilon_{ubo}(s)$ is the uncompensated closed-loop transfer function for the boost operation mode.

As depicted in Figure 4.12, the Bode diagram for, $\Upsilon_{ubu}(s)$ reveals a cross-over frequency of 18.5 kHz and a phase margin of 0.192°. Based on the phase-margin stability criterion, the system is on the edge of instability and significantly deviates from the suggested phase margin value. In order to obtain the complete closed-loop transfer function of the system, the above defined $G_C(s)$ needs to be structured as the controller transfer function in the buck operation mode. By employing MATLAB SISOTOOL, the transfer function of the present controller for the buck operation mode is determined as follows:

$$G_C(s) = 8.809\frac{(1+0.00015s)(1+0.0071s)}{s} \tag{4.27}$$

Figure 4.13 presents the Bode graph of the closed-loop transfer function of the system, including the controller. Highlights the updated crossover frequency point at 2 kHz, equating to a tenth of the switching frequency. The phase margin is also established at 57.4°. These parameters guarantee that the output of the system is reactive only to variations in the reference, ensuring its stability.

An equivalent examination is conducted on the voltage at C_1, resulting in the

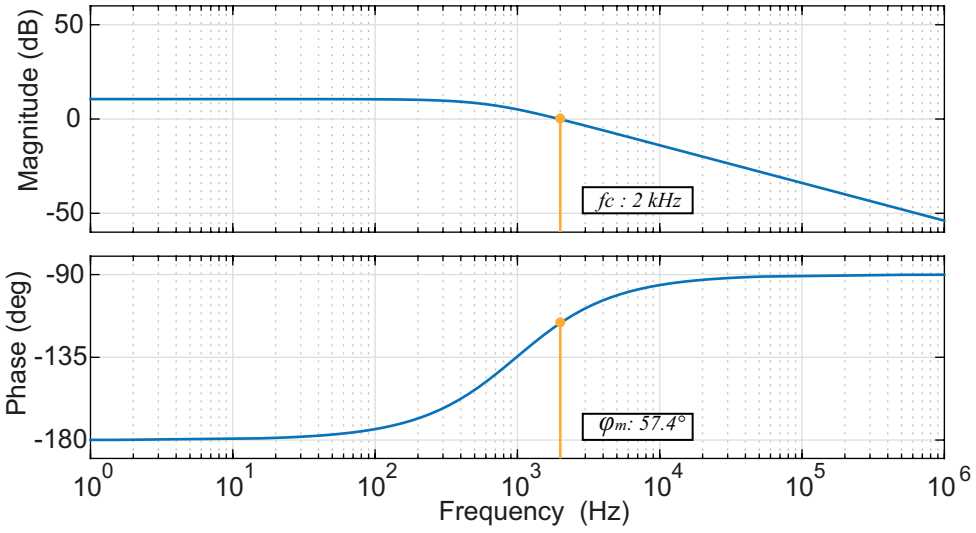

Figure 4.13: Complete closed-loop transfer function Bode plot of the compensated system in buck operation mode.

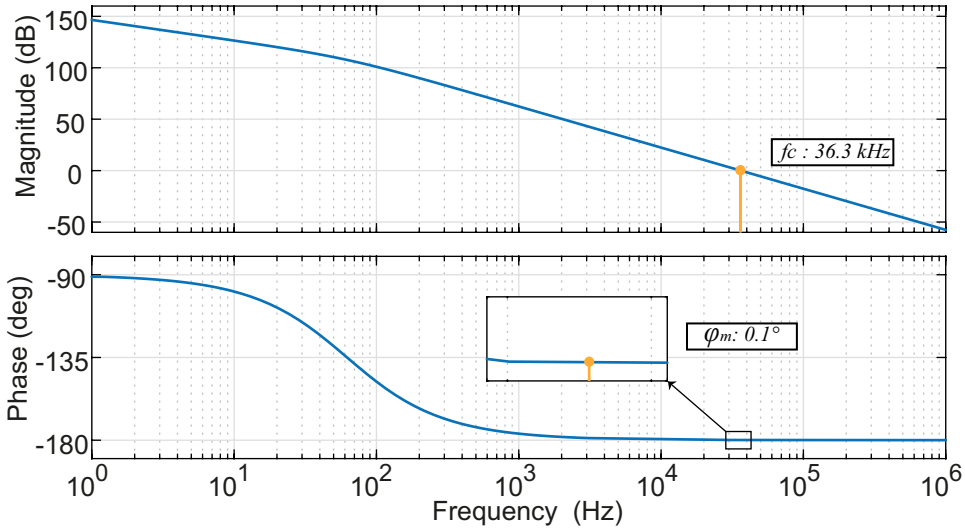

Figure 4.14: Uncompensated close-loop $\Upsilon_{ubo}(s)$ bode plot.

voltage controller, the output of which is combined with the output of the current controller. The transfer function for the voltage controller C_1 (G_{C1}) is given as follows:

$$G_{C_1}(s) = 0.0013(1 + \frac{1.35e^{-4}}{s}) \tag{4.28}$$

In the other hand, the same analysis is performed for the boost operating mode. The bode plot of the uncompensated transfer function of the system (equation 4.26) in this operation mode is depicted in Figure 4.14.

Figure 4.14, shows that the uncompensated system transfer function exhibits a phase margin that is nearly zero, hovering on the edge of instability. Consequently, it is imperative to once again devise a controller that, in conjunction with current regulation, ensures the stability of the system. In other words, the phase margin should exceed zero and fall within the suggested range. The resulting transfer function of the controller G_{Cb} is as follows:

$$G_{Cb}(s) = 0.954\frac{(1 + 0.0005s)(1 + 0.0005s)}{s} \tag{4.29}$$

Figure 4.15, shows the Bode plot of the compensated close-loop transfer function, in which the effect of the compensator on the system can be observed.The new

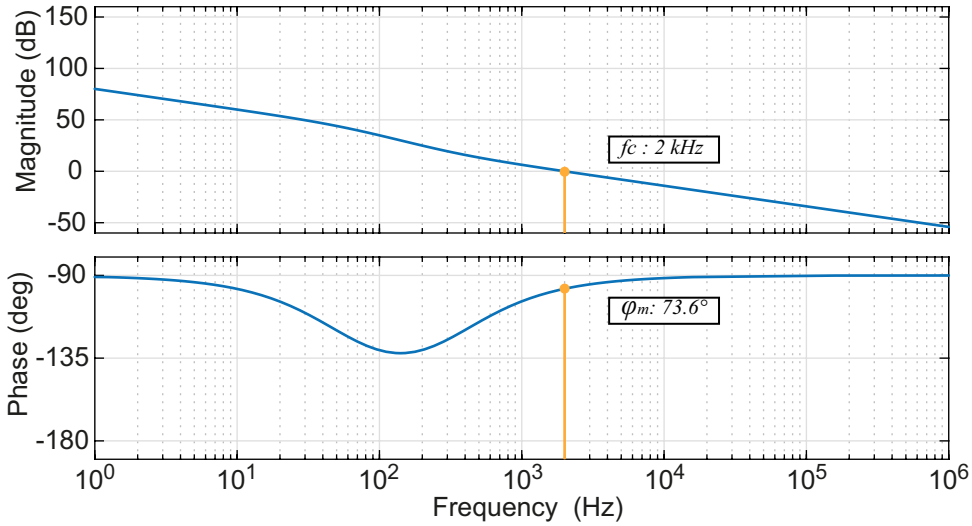

Figure 4.15: Complete closed-loop transfer function Bode plot of the compensated system in boost operation mode.

transmission function sets the crossing frequency at 2kHz, i.e. a value equivalent to one-tenth of the switching frequency. It has also been found that phase margin is now 73.6°, which is within the recommended range and ensures system stability.

With a similar analysis, we derive the voltage controller for the capacitor C_2, and the corresponding transfer function G_{C_2} for this controller is:

$$G_{C_2}(s) = 0.1(1 + \frac{100}{s}) \tag{4.30}$$

The external voltage controller, shown in Figure 4.11, is set to a bandwidth that is one-tenth of the bandwidth used for the internal current controllers. In the CV charging mode, the output of this controller is utilized to supply the current reference needed by the current controllers in all operating modes of the converter. The resulting voltage controller transfer function G_{ce2} is:

$$G_{ce2}(s) = 0.005(1 + \frac{8000}{s}) \tag{4.31}$$

4.2.3 Simulation results

This section demonstrates the validation of the wide output range buck-boost impedance network converter converter functionality through simulations conducted

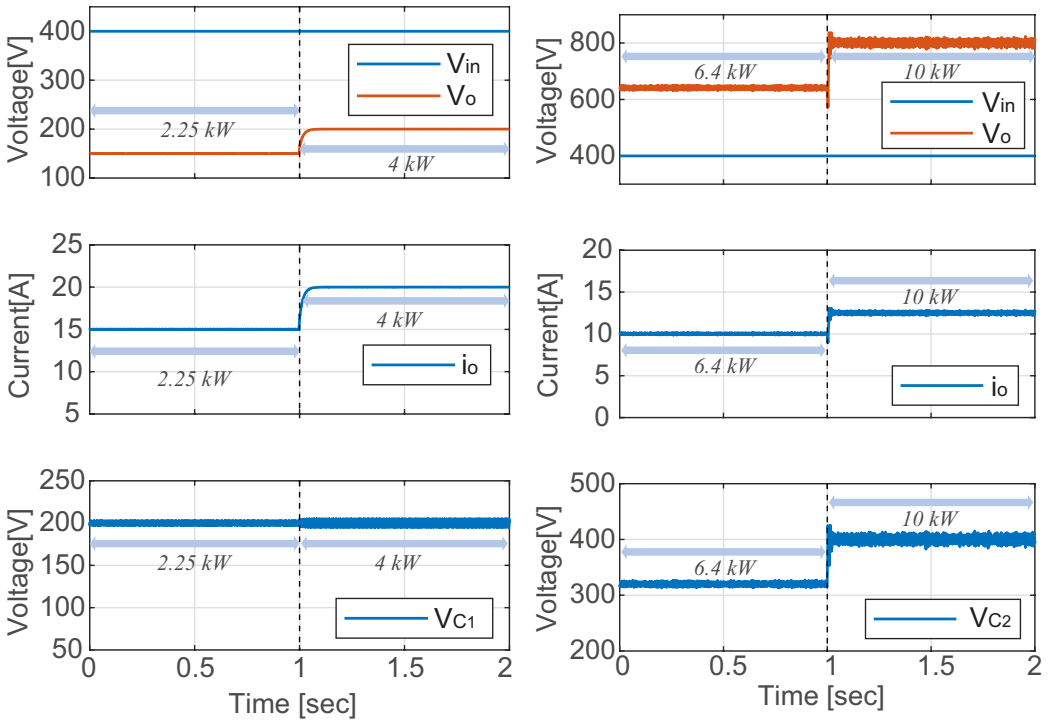

Figure 4.16: Behavior of the converter in operating modes: a) Buck; b) Boost.

in the PLECS software. Figure 4.16 illustrates the voltage characteristics of capacitors C_1 and C_2. It also displays the variations in output voltage and current when there is an increase in the converter output power, in both buck and boost operation modes.

Figure 4.16 a) displays the buck mode simulation outcomes. It starts with an input voltage of 400 V and an initial power of 2.25 kW. At $t = 1s$, the output power shifts to 4 kW. The performance of the system aligns with the predictions, initially, the output voltage stands at 150 V, which rises to 200 V following the power adjustment at $t = 1s$. In the boost operation mode, shown in Figure 4.16 b), the same input voltage of 400 V is applied. Initially, the converter delivers an output power of 6.4 kW, achieving an output voltage of 640 V and a C_2 capacitor voltage of 320 V, which is half the output voltage. At $t = 1$ s, the output power changes to 10 kW. Following this adjustment, the output voltage rises to 800 V, and the C_2 capacitor voltage is adjusted to 400 V, maintaining a consistent half of the output voltage.

A subsequent simulation involves a 60 kWh Li-ion battery, detailed in section 4.1.3, which is used to evaluate the proposed DC-DC converter in a charging

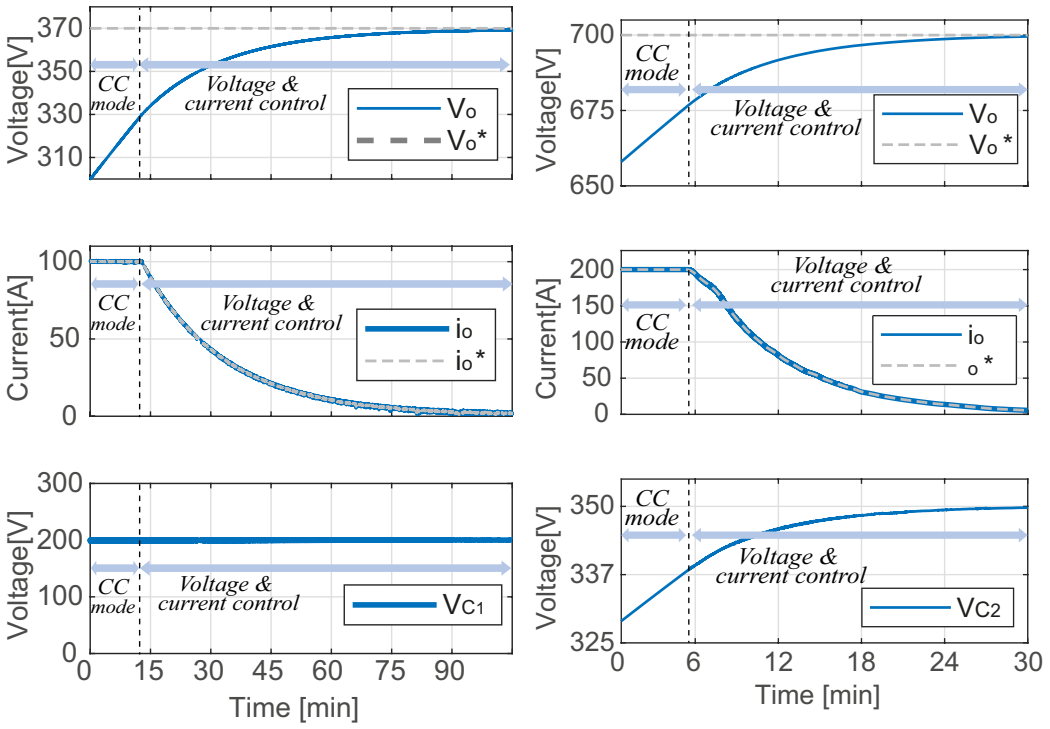

Figure 4.17: Battery charging process for: a) LV battery configuration; b) HV battery configuration.

station that supports both 400 V and 800 V systems. Table 4.2 presents the parameters for simulating the DC-DC converter at the fast-charging station.

Figure 4.17 illustrates the operation of the designed wide output range buck-boost impedance network converter, which serves as the DC-DC converter stage in a charging system for 370 V and 700 V battery setups, via CC-CV charging algorithm. This charging algorithm is divided into two phases. The initial phase is the constant current mode, where the battery receives a steady current until it reaches a specified SoC, around 80%. Following this, the constant voltage phase ensures that the battery is safely charged to 100% SoC. During this phase, a steady voltage, equal to the battery nominal voltage, is maintained across the battery terminals. As the desired voltage level is reached, the current slowly reduces to its lowest level.

In the 400 V system, Figure 4.17 a) illustrates the converter output voltage, output current, and C_1 capacitor voltage alongside their reference signals, demonstrating their adherence to the loading algorithm. The ripple in the inductor current i_o is approximately of 1.7%.Initially, in CC charging mode, the battery is charged

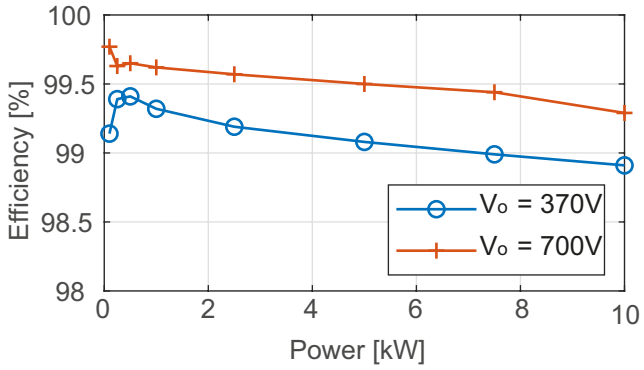

Figure 4.18: Estimated efficiency of the wide output range buck-boost impedance network converter.

with a current of 100 A, reaching a peak power of 33 kW. When the battery reaches an 80% SoC, the charging algorithm switches from CC mode to CV mode. During this phase, the external voltage controller takes over the task of providing the current reference, which progressively decreases as the output voltage approaches its set point of 370 V. Figure 4.17 a) also depicts the voltage across the capacitor C_1, consistently held at 200 V, corresponding to half the input voltage.

For the 700 V battery, Figure 4.17 b) illustrates the voltage output, current output, and voltage across capacitor C_2 of the converter. The operation of the charging algorithm is observed once more; during CC mode, the battery is charged with a current of 200 A, achieving a peak power of 135 kW, which allows the charging process to be accelerated. The battery attains 80% SoC in about 6 minutes, subsequently transitioning to CV mode. In this phase, the current gradually reduces as the output voltage nears its reference value.

A simulation was conducted using the PLECS thermal model component to evaluate the efficiency of the proposed converter. The C3M0025065D MOSFET and the GD2X20MPS12D diode were used. The efficiency results for both operational modes are presented, within a power range between 0 kW and 10 kW. Figure 4.18 illustrates the converter efficiency for both buck and boost modes, The efficiency peaks are for the boost operation mode, when the output voltage approximates the battery voltage in low power operation, reaching up to 99.6%, in the boost mode, the lowest efficiency is observed at maximum power output, specifically at 10 kW, where it is approximately 99.4%. Likewise, in the buck mode, higher efficiency is observed at lower power levels, particularly when the output voltage closely matches the input voltage of the converter, averaging at 99. 45%. As the power level increases, the efficiency decreases, reaching a minimum of 98.9% at a power output of 10 kW.

4.3 Conclusion

In this chapter the theoretical validation through a software simulation of the new step-up transformerless Type I PPC is presented the step-up nature of the converter makes it suitable for use primarily in 800 V battery systems. The topology has been derived from a typical PPC Type I, by replacing the HF transformer by an impedance network capable of connecting voltages in series to the input voltage to boost the output voltage with a nominal gain of 2. The advantage of this proposed converter over traditional boost converters lies in the fact that the voltage blocked by the semiconductors and the passive components of the circuit is equal to the input voltage, which allows them to be sized with lower nominal values, making this a cost-effective solution. In the next section of this chapter, for the wide output range buck-boost impedance network converter; its model and behavior have been validated through simulations. The primary benefit of this converter is its adaptability for charging vehicles, with different battery voltage configurations, enabling it to meet the requirements of both modern and older electric vehicle models.

In the next chapter, the experimental validation of these two converters will be presented.

Chapter 5

EXPERIMENTAL RESULTS

THIS chapter provides an experimental validation of the two converter proposed and developed throughout this thesis.

5.1 Impedance network type I partial power converter

A reduced-scale laboratory prototype based on silicon carbide (SiC) MOSFETs has been built to validate the proposed converter. Figure 5.1 shows the laboratory prototype. For the active H-bridge, the SiC G3R40MT12D MOSFET was used, while for the passive rectifier that is connected to the output inductor, the GD2X20MPS12D diodes were used. The dead time of the H-bridge circuit was considered in the hardware when designing the control boards for the semiconductor gating signals. The parameters used for the experimental results are listed in Table 5.1.

As input of the converter, emulating the DC-link that is generated by the AC-DC rectifier of the charging station, the Chroma 62020H-150S programmable supply has been used. To emulate the EV battery a Chroma 62060-D bidirectional power

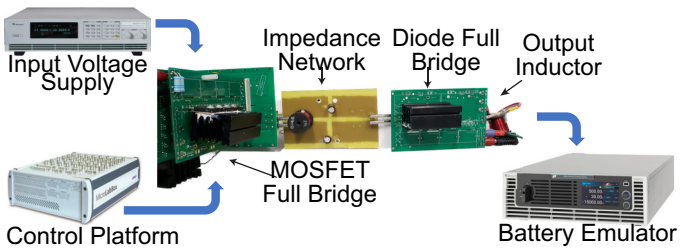

Figure 5.1: Experimental setup for the impedance network type I PPC.

Table 5.1: Experimental parameters for impedance network type I PPC.

Parmeter	Values
Input voltage V_{in}	150 V
Output voltage V_o	300 V
Output current i_o	4 A
Output current (charger mode)	3 A
Output inductor L	0.625 mH
Impedance network inductor L_1	0.625 mH
Impedance network capacitors C_1	10 μF
Impedance network capacitors C_2	10 μF
Switching frequency f_{sw}	10 kHz
MOSFETs	C3M0025065D
Diodes	GD2X20MPS12D

supply has been used as load connected to the output terminals of the proposed converter. It has been configured considering the battery voltage, capacity, and initial SoC. The control of the converter is implemented using the dSpace MicroLabBox platform.

Figure 5.2 shows the validation of the transfer function of the system derived in (3.15), compared to the same curve obtained experimentally. A maximum error of 2% has been achieved between the experimental and theoretical results throughout the range of the phase shift α, validating the analytical derivation of the model of the converter.

To begin operation, the converter needs to be initialized by pre-charging the capacitors of the impedance network. This is achieved by connecting a resistor in series with the converter via relay activation, thereby setting up specific switching signals to charge the capacitors C_1 and C_2 to the input voltage level. After the pre-charge process is completed, the resistor is disconnected, and the converter begins its regular operation.

The main waveforms of the converter are preliminary validated using a purely resistive load ($R = 100\Omega$) connected to the output terminals. This test was carried out in open-loop, and no phase shift is imposed between the primary bridge legs ($\alpha = 0.5$). This results in an output voltage equal to the double the input voltage. This can be appreciated in Figure 5.3(a) where results for an input voltage value of 150 V are shown, including: channel 1 (yellow) corresponds to the output voltage of the converter at twice the input voltage (300 V); Channel 2 (green) shows the C_1 capacitor voltage, and it can be seen that this voltage is always equal to the

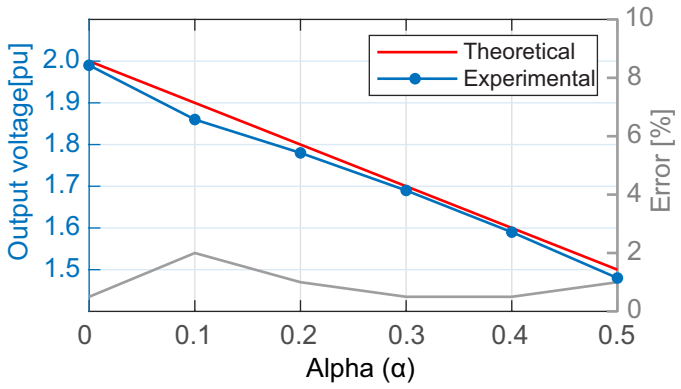

Figure 5.2: Experimental validation of the transfer funcion of the type I impedance network converter.

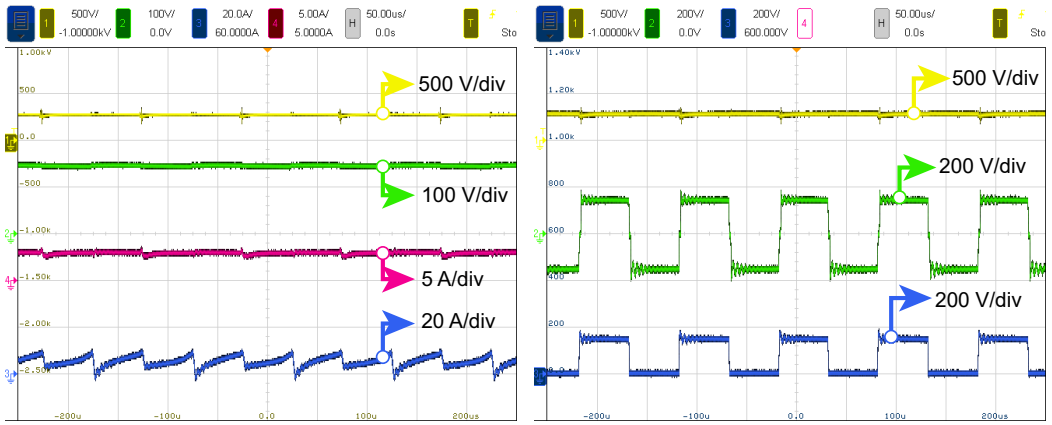

(a) (b)

Figure 5.3: Experimental results with resistive load and $\alpha = 0.5$: a) Ch1: Output voltage V_o, Ch2: Capacitor voltage V_{C_1}, Ch3: Output current i_L, Ch4: Input current i_{in}; b) Ch1: Output voltage V_o, Ch2: Impedance network inductor voltage V_{L_1}, Ch3: switch Sb drain-source voltage.

input voltage; Channels 3 (blue) and 4 (red) display the input and output current measurements respectively. Since it is a boost converter, the output current is lower than the input current. For this case, the value of the output current of 3 A is determined by the resistive load used for the test.

Channel 1 (yellow) of Figure 5.3(b) shows the output voltage of the converter again, while channel 3 (blue) shows the voltage across switch S_b; the maximum voltage that the semiconductors withstands during switching, unlike a traditional boost converter, is equal to the input voltage (it switches between 0 V and 150 V).

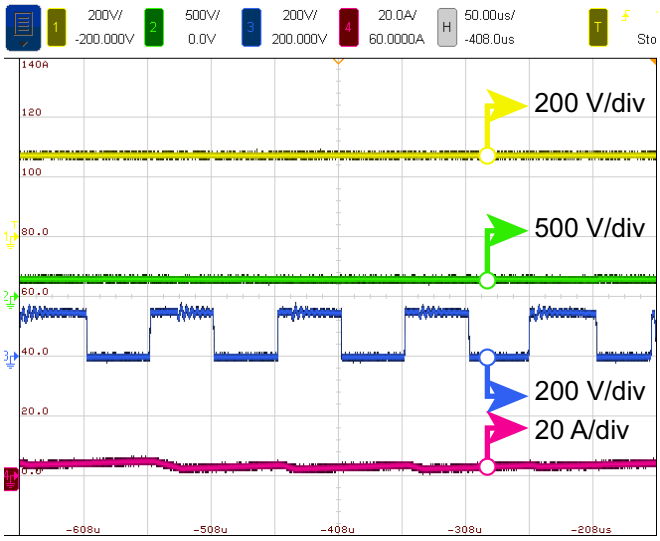

Figure 5.4: Experimental results during battery charging cycle. Ch1: Output voltage V_o, Ch2: Impedance network capacitor voltage V_{C_1}, Ch3: switch S_b voltage, Ch4: Output current i_L.

This feature allows sizing the MOSFETs with nominal values lower than the output voltage. Finally, channel 2 (green) shows the impedance network inductor voltage V_{L1}, switching between -150 V and 150 V as expected.

In addition, a closed-loop battery charging process was tested, using the Chroma 62060-D bidirectional power supply to emulate the battery. The control profile is programmed in the local CPU and interfaced with the converter through a dSpace MicroLabBox. The results of the test are displayed in Figure 5.4, which provides a visual representation of the current and voltage profiles in steady-state operation. In order to speed up an entire charge cycle, the battery is simulated with a reduced capacity, as shown in Table 5.1. The battery emulator used in this test was programmed to operate at 300 V with an initial state-of-charge of 60%. This produced an initial voltage of 264 V. The behavior of the converter during steady-state was captured in a reduced timescale. Channel 1 (yellow) shows the battery voltage, charged with constant current of 3 A, which is shown in channel 4 (red). Channel 2 (green) shows the voltage in capacitor C_1; regardless of the state-of-charge of the battery voltage, the capacitor voltage always equals the input voltage, keeping its value at 150 V. Channel 3 (blue) shows the voltage across switch S_b. In the same way, as for the test carried out with resistive load, the voltage in the semiconductors varies between 0 V and 150 V.

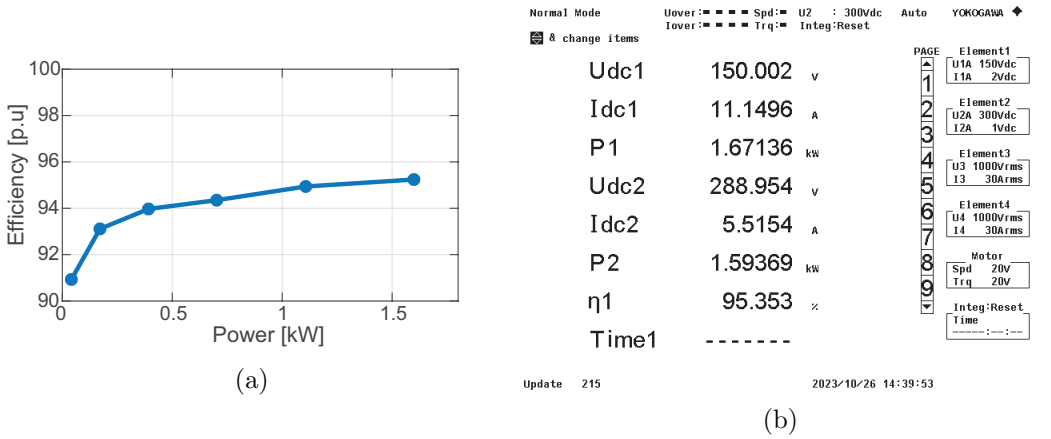

Figure 5.5: Experimental measurements. a) Over 01 kW to 0.5 kW range; b) Measured input and output powers, voltages, currents, and global efficiency of the proposed PPC at 1.6 kW.

Experimental efficiency analysis

An experimental efficiency examination of the converter was conducted using the Yokogawa Precision Power Analyzer WTE3000E with the same parameters of the components listed in Table 5.1.

The results obtained in the efficiency analysis are shown in Fig. 5.5, as well as a screenshot that indicates the measured input and output active powers, voltages, currents, and global efficiency of the proposed PPC. The power range that was studied exhibits the same features as the efficiency curve that was obtained from the simulation. The prototype constructed with a modular characteristic achieved a maximum efficiency of 95.35%, the modular characteristic with which the experimental prototype was built influences the slight difference between the results of Figure 5.5 a) and Figure 5.5 b).

5.2 Wide output range buck-boost impedance network converter

To experimentally validate the wide output range buck-boost impedance network converter, a scaled-down prototype was adapted, as illustrated in Figure 5.6. The semiconductors implemented in the converter include the SiC G3R40MT12D MOSFETs and GD2X20MPS12D diodes.

The DC link connected to the converter is emulated using the Chroma 62020H-150S programmable source, while the batteries configured for LV and HV are simulated using the Chroma 62060-D bidirectional source. The entire control scheme of

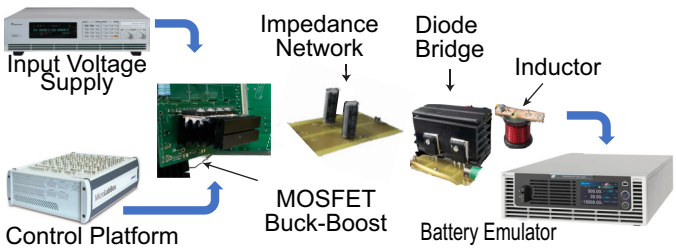

Figure 5.6: Experimental setup for the wide output range buck-boost impedance network converter.

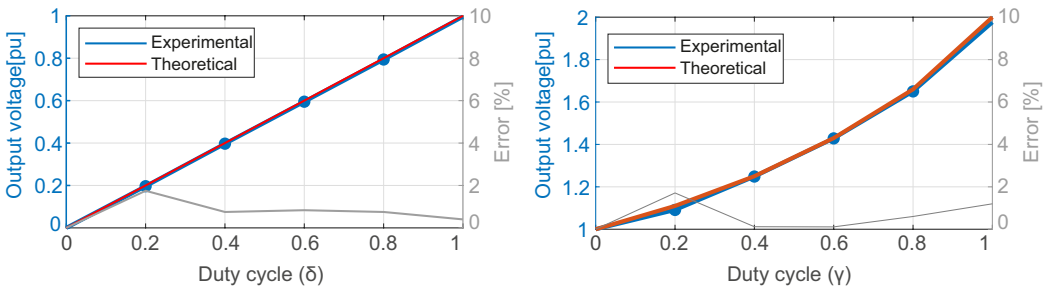

(a) (b)

Figure 5.7: Experimental validation of the wide output range buck-boost impedance network converter: a) Buck operation mode; b) Boost operation mode.

the converter was developed in SIMULINK, and the dSpace MicroLabBox platform was used to transmit the switching signals to the semiconductor devices.

As with the previous converter, it is essential to implement a pre-charge phase for the capacitors in the impedance network before initiating regular converter operations.

Figure 5.7 demonstrates the validation of the converter transfer function in both buck and boost operation modes. Figure 5.7 a) shows the converter gain curve relative to the duty cycle, where the red curve represents the graph of the equation that models the converter transfer function, shown in (3.33). The blue curve shows the converter gain measured at five different duty cycle values, revealing that the error between the two curves peaks at 2% when the output voltage significantly deviates from the converter input voltage. When the converter gain approaches 1, the error percentage falls below 1%. Similarly, low error percentages are observed in the boost mode operation,equation (3.43), as seen in Figure 5.7 b), where the highest error percentage occurs at gain levels close to unity, when the boost mode converter functions with an output voltage close to the input voltage.

Table 5.2: Experimental parameters for wide output range buck-boost impedance network converter in boost operation mode.

Parmeter	Values
Input voltage V_{in}	50 V
Output voltage V_o	90 V
Output current i_o	3 A
Output inductor L	0.625 mH
Impedance network capacitors C_1	100 μF
Impedance network capacitors C_2	100 μF
Switching frequency f_{sw}	10 kHz
MOSFETs	C3M0025065D
Diodes	GD2X20MPS12D

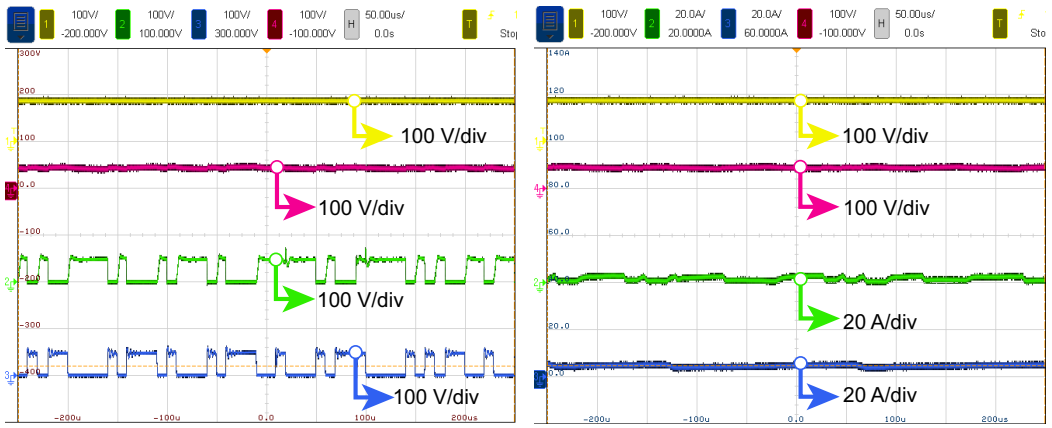

(a) (b)

Figure 5.8: Experimental results for the boost operation mode. (a) Ch1: Output voltage V_o, Ch2: Switch S_c drain-source voltage, Ch3: Switch S_d drain-source voltage, Ch4: Capacitor voltage V_{C_2}; (b) Ch1: Output voltage V_o, Ch2: Output inductor current i_o, Ch3: Input inductor current i_L, Ch4: Capacitor voltage V_{C_2}.

To validate the converter experimentally, the outcomes are categorized into two operational modes. In boost mode, the parameters used to test the converter are displayed in the Table. 5.2. Figure 5.8 presents the experimental results for the converter in boost mode with an input voltage set at 50 V, and the Chroma 62060-D device simulating a 1 kWh battery connected to the output. In Figure 5.8 a), Channel 1 (yellow) shows the output voltage V_o, which corresponds to the voltage of the battery simulator, set at 90 V to maintain the operation of the converter boost mode. Channel 2 (green) illustrates the voltage across the semiconductor S_c, which

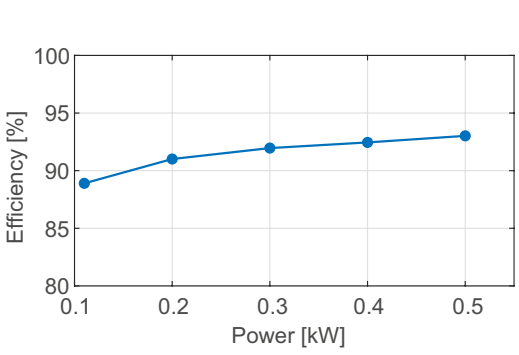

(a)

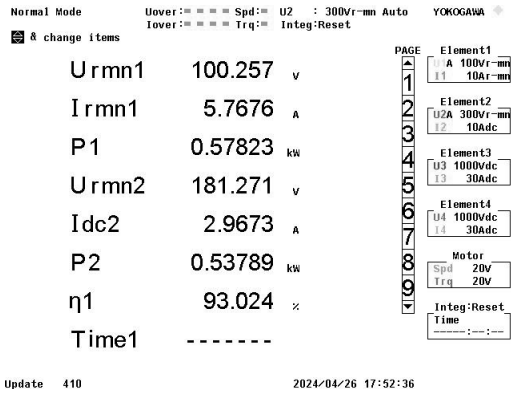

(b)

Figure 5.9: Experimental efficiency measurement of the wide output range buck-boost impedance network converter, boost operation mode: a) Efficiency plot over a 0.5 kW power range; (b) Measured input and output powers, voltages, currents, and global efficiency of the converter at 0.5 kW.

is the same as the converter input voltage, 50 V. Similarly, channel 3 (blue) shows the voltage across the semiconductor S_d, equal to the input voltage of the converter. Channel 4 (red) indicates the voltage on the capacitor C_2, set at 45 V, half of the output voltage. In Figure 5.8 b), channels 1 and 4 (yellow and red) again show the output voltage of the converter and the voltage across the impedance network capacitor C_2. Channel 2 (green) reveals the output current i_o, noted at 3 A in this instance. Finally, channel 3 (blue) displays the current i_L flowing through the inductor L at the input of the converter in this setup.

The efficiency analysis is conducted anew using the Yokogawa Precision Power Analyzer WTE3000E, assessing the converter across a power spectrum from 0.1 kW to 0.5 kW.

Figure 5.9 a) displays the efficiency measurements throughout the specified power range, where the recorded peak efficiency corresponds to the high power point at 0.53 kW, achieving 93.024%. Figure 5.9 presents a screenshot of the power analyzer for the case with the highest reported efficiency.

For the buck operation mode, Table 5.3 presents the pertinent parameters. Figure 5.10 illustrates the experimental results for the proposed converter when connected to the battery simulator, which facilitates its operation in the buck operation mode. The input voltage is established at 150 V, while the output voltage, aligned with the battery simulator settings, is 75 V. In the diagram, channel 1 (yellow) shows the output voltage of the converter V_o set at 75 V. Channel 2 (green) illustrates the

Table 5.3: Experimental parameters for wide output range buck-boost impedance network converter in buck operation mode.

Parmeter	Values
Input voltage V_{in}	150 V
Output voltage V_o	70 V
Output current i_o	4 A
Output inductor L	0.625 mH
Impedance network capacitors C_1	100 μF
Impedance network capacitors C_2	100 μF
Switching frequency f_{sw}	10 kHz
MOSFETs	C3M0025065D
Diodes	GD2X20MPS12D

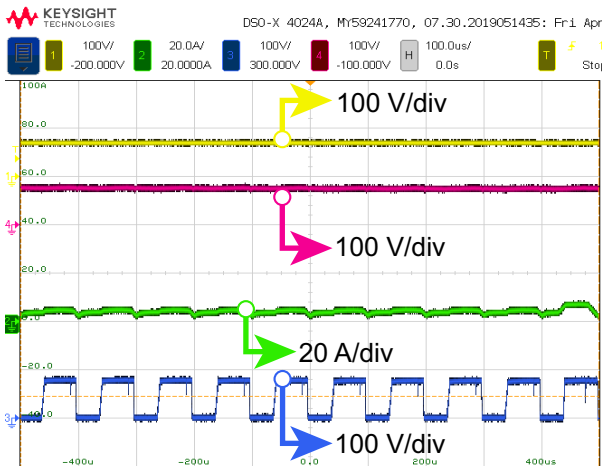

Figure 5.10: Experimental results for the buck operation mode. Ch1: Output voltage V_o, Ch2: Output current i_L, Switch S_a drain-source voltage, Ch4: Capacitor voltage V_{C_1}.

output current i_o, with a current of 3 A being directed injected into the battery for the charging process. Channel 3 (blue) presents the drain-source switch voltage V_{S_a}, consistently maintained at half the input voltage. Channel 4 (red) indicates the voltage on the capacitor C_1, which is controlled to match half the input voltage as depicted, the voltage V_{C_1} is 75 V.

Figure 5.11 shows the efficiency measurements conducted on the converter in its buck operation mode. Figure 5.11 a) presents the efficiency data for five different power levels ranging from 0.1 kW to 0.5 kW, with the highest efficiency recorded at 92. 05%, as shown in the screenshots of the Yokogawa Precision Power Analyzer

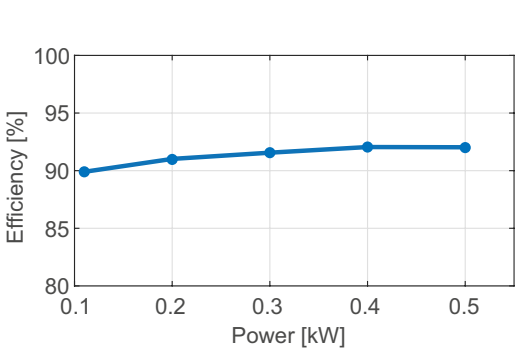

(a)

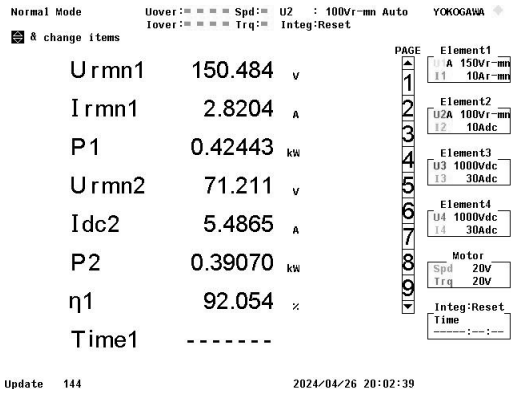

(b)

Figure 5.11: Experimental efficiency measurement of the wide output range buck-boost impedance network converter, buck operation mode: a) Efficiency plot over a 0.1 kW to 0.5 kW power range; (b) Measured input and output powers, voltages, currents, and global efficiency of the converter at 0.4 kW.

WTE3000E shown in Figure 5.11.

5.3 Conclusion

The operating principle, converters waveforms, and converters gain were experimentally validated through two reduced-scale laboratory prototypes, including an emulated battery charging process.

For the type I impedance network PPC, the experimental comparison with the mathematical model showed a maximum error of 2%. In the experimental analysis, it was possible to measure the efficiency of the converter. The peak efficiency achieved of 95.35%, enabling a high efficiency charging process.

In the case of the wide output range dual impedance network converter, the highest error observed in the experimental measurements compared to the mathematical model was also 2%, and the measured peak efficiency was 93. 02%. These results confirm the suitability of the proposed converters as viable options for DC-DC conversion in electric vehicle battery charging systems.

Chapter 6

CONCLUSIONS

IN this work, two novel transformerless converter designs with an impedance network are presented, aimed at the DC-DC conversion stage in EV battery charging stations. These converters operate on the principle of partial power processing, where only a portion of the total power delivered to the battery is managed by the converter. This approach significantly lowers the losses incurred during converter operation while maintaining system functionality and without increasing complexity.

Although traditional type I and type II PPC configurations incorporate HF transformers in their converter topologies, they fail to maintain galvanic isolation. This failure is attributed to the direct connection that allows a portion of the power, bypassing the converter, to directly reach the battery. Consequently, galvanic isolation becomes essential at an earlier stage, using either an LF transformer or an additional unregulated DC-DC stage. Based on these findings, the study has shown that it is feasible to substitute the HF transformer in a PPC with an impedance network without compromising the proper functioning of the converter.

The most significant conclusions derived from theoretical analysis, simulations, and experimental assessments are:

- A variety of tests and assessments have demonstrated that the implementation of the impedance network preserves the converter capability to partially power operation. Furthermore, it has been established that this setup facilitates the ideal control of voltage and current regulation, guaranteeing consistent and dependable operation during the energy conversion process in an EV battery charging process. Hypothesis I is validated by the simulation results showed in Figure 4.8, which illustrate the current regulation of the battery

during the two charging modes following the CC-CV charging algorithm. Furthermore, the experimental findings shown in Figure 5.4 corroborate the converter performance throughout a battery charging cycle. These findings underscore the benefits of the impedance network instead of an HF transformer for battery chargers.

- A comprehensive simulation was carried out to validate the second hypothesis, with the results shown in Figure 4.9. This figure contrasts the efficiency of a type I impedance network PPC with that of a type I PPC incorporating an HF transformer. The data reveal that the use of an impedance network in place of the HF transformer enhances the efficiency of the converter by reducing the associated losses. This approach improves power transfer, presenting a new method for increasing efficiency in EV battery charging applications and opening the door to the development of more efficient DC-DC converters that do not require HF galvanic isolation.

- Achieving a wide output voltage range in a converter has been enabled by utilizing a buck-boost converter implemented with a dual impedance network, validating the third hypothesis, based on the simulated results shown in Figures 4.16 and 4.17, and the experimental results presented in Figures 5.8 and 5.10. Proper voltage regulation within this network facilitates the minimization of the converter passive and active component size while ensuring that the semiconductor voltages remain at half the output and input voltages, whether in step-up or step-down mode. This wide output voltage range makes the converter an effective option for accommodating the diverse voltage requirements of electric vehicle batteries, applicable in both low and high-voltage configurations.

It is important to note that the proposed type I impedance network PPC and the wide output range buck-boost impedance network converter both lack galvanic isolation. They are intended for use as DC-DC converters that provide voltage and current regulation within a charger architecture. This architecture will incorporate an earlier DC-DC stage without voltage and current regulation, which must include HF isolation. The focus of future research will be on this initial DC-DC stage, as its primary feature should be the achievement of very high efficiency. This ensures that the overall efficiency of the system remains unaffected by the adoption of two DC-DC topologies.

A notable aspect of the type I impedance network PPC is its step-up characteristic, which demonstrates a gain confined to a range of 1.5 to 2. This property restricts its use in chargers designed to charge batteries with varying voltage configurations. However, it is a viable choice for chargers meant for fixed voltage configurations, either 400 V or 800 V. Furthermore, these topologies can be used as an additional

step-up stage for existing charging stations that support only 400 V or lower configurations. This upgrade would also allow these stations to also charge the 800 V configurations employed by several modern EV manufacturers.

Finally, the experimental results of both converters were conducted at power levels lower than those used in the simulations, as the aim was to confirm the correct functioning of the proposed impedance network topologies. Similarly, the construction was not optimized, which resulted in a reduction in the achievable maximum efficiency, as indicated by the simulation results. The next phase involves improving the design of the prototypes. This should include an additional analysis of topologies, aiding in enhancing the performance of each impedance network topology and thereby, achieving greater conversion efficiencies.

REFERENCES

[1] Hannah Ritchie, "Sector by sector: where do global greenhouse gas emissions come from?" 2020. [Online]. Available: https://ourworldindata.org/ghg-emissions-by-sector{#}note-3

[2] C. Jung, "Power Up with 800-V Systems," *IEEE Electrification Magazine*, vol. 5, no. 1, pp. 53–58, 2017.

[3] E. D. Kostopoulos, G. C. Spyropoulos, and J. K. Kaldellis, "Real-world study for the optimal charging of electric vehicles," *Energy Reports*, vol. 6, pp. 418–426, 2020. [Online]. Available: https://doi.org/10.1016/j.egyr.2019.12.008

[4] S. Rivera, S. M. Goetz, S. Kouro, P. W. Lehn, M. Pathmanathan, P. Bauer, and R. A. Mastromauro, "Charging infrastructure and grid integration for electromobility," *Proceedings of the IEEE*, vol. 111, no. 4, pp. 371–396, 2023.

[5] S. Rivera, S. Kouro, S. Vazquez, S. M. Goetz, R. Lizana, and E. Romero-Cadaval, "Electric Vehicle Charging Infrastructure: From Grid to Battery," *IEEE Industrial Electronics Magazine*, vol. 15, no. 2, pp. 37–51, 2021.

[6] M. Tavassoli and A. Kamran-Pirzaman, "Comparison of effective greenhouse gases and global warming," in *2023 8th International Conference on Technology and Energy Management (ICTEM)*, 2023, pp. 1–5.

[7] B. K. Bose, "Energy, Global Warming and Impact of Power Electronics in the Present Century," *Power Electronics for Renewable Energy Systems, Transportation and Industrial Applications*, pp. 1–26, 2014.

[8] L. Dickerman and J. Harrison, "A New Car, a New Grid," *IEEE Power and Energy Magazine*, vol. 8, no. 2, pp. 55–61, 2010.

[9] M. Ma, Z. Chang, Y. Hu, F. Li, C. Gan, and W. Cao, "An Integrated Switched Reluctance Motor Drive Topology with Voltage-Boosting and On-Board Charging Capabilities for Plug-In Hybrid Electric Vehicles (PHEVs)," *IEEE Access*, vol. 6, pp. 1550–1559, 2017.

[10] M. Scott, "Ever cheaper batteries bring cost of electric cars closer to gas guzzlers," https://www.forbes.com/sites/mikescott/2020/12/18/ever-cheaper-batteries-bring-cost-of-electric-cars-closer-to-gas-guzzlers/?sh=7439281b73c1, December 2020, accessed on March 12, 2024.

[11] Z. P. Cano, D. Banham, S. Ye, A. Hintennach, J. Lu, M. Fowler, and Z. Chen, "Batteries and fuel cells for emerging electric vehicle markets," *Nature Energy*, vol. 3, no. 4, pp. 279–289, 2018.

[12] BloombergNEF, "Lithium-ion battery pack prices hit record low of $139/kwh," https://about.bnef.com/blog/lithium-ion-battery-pack-prices-hit-record-low-of-139-kwh/, November 2023, accessed on March 12, 2024.

[13] S. Ahmed, I. Bloom, A. N. Jansen, T. Tanim, E. J. Dufek, A. Pesaran, A. Burnham, R. B. Carlson, F. Dias, K. Hardy, M. Keyser, C. Kreuzer, A. Markel, A. Meintz, C. Michelbacher, M. Mohanpurkar, P. A. Nelson, D. C. Robertson, D. Scoffield, M. Shirk, T. Stephens, R. Vijayagopal, and J. Zhang, "Enabling fast charging A battery technology gap assessment," *Journal of Power Sources*, vol. 367, pp. 250–262, 2017.

[14] G. H. Broadbent, G. Metternicht, and D. Drozdzewski, "An analysis of consumer incentives in support of electric vehicle uptake: An Australian case study," *World Electric Vehicle Journal*, vol. 10, no. 1, pp. 1–15, 2019.

[15] I. Aghabali, J. Bauman, P. J. Kollmeyer, Y. Wang, B. Bilgin, and A. Emadi, "800-V Electric Vehicle Powertrains: Review and Analysis of Benefits, Challenges, and Future Trends," *IEEE Transactions on Transportation Electrification*, vol. 7, no. 3, pp. 927–948, 2021.

[16] M. Momayyezan, B. Hredzak, and V. G. Agelidis, "Integrated reconfigurable converter topology for high-voltage battery systems," *IEEE Transactions on Power Electronics*, vol. 31, no. 3, pp. 1968–1979, 2016.

[17] J.-Y. Kim, B.-S. Lee, D.-H. Kwon, D.-W. Lee, and J.-K. Kim, "Low voltage charging technique for electric vehicles with 800 v battery," *IEEE Transactions on Industrial Electronics*, vol. 69, no. 8, pp. 7890–7896, 2022.

[18] H. Sarnago, s. LucÃa, R. JimÃ©nez, and P. Gaona, "Differential-power-processing on-board-charger for 400/800-v battery architectures using 650-v super junction mosfets," in *2021 IEEE Applied Power Electronics Conference and Exposition (APEC)*, 2021, pp. 564–568.

[19] D. Lyu, T. B. Soeiro, and P. Bauer, "Design and implementation of a reconfigurable phase shift full-bridge converter for wide voltage range ev charging

application," *IEEE Transactions on Transportation Electrification*, vol. 9, no. 1, pp. 1200–1214, 2023.

[20] H. Karneddi and D. Ronanki, "Reconfigurable battery charger with a wide voltage range for universal electric vehicle charging applications," *IEEE Transactions on Power Electronics*, vol. 38, no. 9, pp. 10 606–10 610, 2023.

[21] D. Pesantez, H. Renaudineau, S. Rivera, A. Peralta, A. Marquez Alcaide, and S. Kouro, "Transformerless partial power converter topology for electric vehicle fast charge," *IET Power Electronics*, vol. 17, no. 8, pp. 970–982, 2024. [Online]. Available: https://ietresearch.onlinelibrary.wiley.com/doi/abs/10.1049/pel2.12613

[22] S. Rivera, D. Pesantez, S. Kouro, and P. W. Lehn, "Pseudo-Partial-Power Converter without High Frequency Transformer for Electric Vehicle Fast Charging Stations."

[23] ——, "Pseudo-Partial-Power Converter without High Frequency Transformer for Electric Vehicle Fast Charging Stations," *2018 IEEE Energy Conversion Congress and Exposition, ECCE 2018*, pp. 1208–1213, 2018.

[24] S. Rivera, J. Rojas, S. Kouro, P. W. Lehn, R. Lizana, H. Renaudineau, and T. Dragicevic, "Partial-Power Converter Topology of Type II for Efficient Electric Vehicle Fast Charging," *IEEE Journal of Emerging and Selected Topics in Power Electronics*, vol. 10, no. 6, pp. 7839–7848, 2022.

[25] Virta, "Global electric vehicle market," https://www.virta.global/en/global-electric-vehicle-market, 2023, accessed on March 12, 2024.

[26] S. Rivera, S. M. Goetz, S. Kouro, P. W. Lehn, M. Pathmanathan, P. Bauer, and R. A. Mastromauro, "Charging Infrastructure and Grid Integration for Electromobility," *Proceedings of the IEEE*, vol. 111, no. 4, pp. 371–396, 2022.

[27] L. Wang, Z. Qin, T. Slangen, P. Bauer, and T. van Wijk, "Grid impact of electric vehicle fast charging stations: Trends, standards, issues and mitigation measures - an overview," *IEEE Open Journal of Power Electronics*, vol. 2, pp. 56–74, 2021.

[28] M. Scott, "Ever-Cheaper Batteries Bring Cost Of Electric Cars Closer To Gas Guzzlers," 2020. [Online]. Available: https://www.forbes.com/sites/mikescott/2020/12/18/ever-cheaper-batteries\-bring-cost-of-electric-cars-closer-to-gas-guzzlers/?sh=7439281b73c1

[29] S. Srdic and S. Lukic, "Toward Extreme Fast Charging: Challenges and Opportunities in Directly Connecting to Medium-Voltage Line," *IEEE Electrification Magazine*, vol. 7, no. 1, pp. 22–31, 2019.

[30] PadPoint, "Tesla model s," https://pod-point.com/guides/vehicles/tesla/2022/model-s, October 2023, accessed on March 08, 2024.

[31] ——, "Hyundai ioniq 5," https://pod-point.com/guides/vehicles/hyundai/2021/ioniq-5, April 2021, accessed on March 10, 2024.

[32] L. Lu, X. Han, J. Li, J. Hua, and M. Ouyang, "A review on the key issues for lithium-ion battery management in electric vehicles," *Journal of Power Sources*, vol. 226, pp. 272–288, 2013. [Online]. Available: http://dx.doi.org/10.1016/j.jpowsour.2012.10.060

[33] J. Schoch, J. Gaerttner, A. Schuller, and T. Setzer, "Enhancing electric vehicle sustainability through battery life optimal charging," *Transportation Research Part B: Methodological*, vol. 112, no. 2018, pp. 1–18, 2018. [Online]. Available: https://doi.org/10.1016/j.trb.2018.03.016

[34] B. Li, K. Xie, W. Zhong, X. Huang, Y. Wu, and S. Xie, "Operation management of electric vehicle battery swapping and charging systems: A bilevel optimization approach," *IEEE Transactions on Intelligent Transportation Systems*, vol. 24, no. 1, pp. 528–540, 2023.

[35] T. Boonraksa, P. Boonraksa, W. Pinthurat, and B. Marungsri, "Optimal battery charging schedule for a battery swapping station of an electric bus with a pv integration considering energy costs and peak-to-average ratio," *IEEE Access*, vol. 12, pp. 36 280–36 295, 2024.

[36] L. Ran, Y. Wan, J. Qin, W. Fu, D. Zhang, and Y. Kang, "A game-based battery swapping station recommendation approach for electric vehicles," *IEEE Transactions on Intelligent Transportation Systems*, vol. 24, no. 9, pp. 9849–9860, 2023.

[37] S. Jain, Z. Ahmad, M. S. Alam, and Y. Rafat, "Battery Swapping Technology," *2020 5th IEEE International Conference on Recent Advances and Innovations in Engineering, ICRAIE 2020 - Proceeding*, vol. 2020, pp. 0–3, 2020.

[38] Z. Chen, "The combination of battery swapping system and connected vehicles technology in intelligent transportation," *Proceedings - 2020 International Conference on Intelligent Transportation, Big Data and Smart City, ICITBS 2020*, pp. 72–75, 2020.

[39] R. Vaka and R. K. Keshri, "Review on contactless power transfer for electric vehicle charging," *Energies*, vol. 10, no. 5, 2017.

[40] V. Ravikiran, R. K. Keshri, and M. Bertoluzzo, "Efficient Wireless Charging of Batteries with Controlled Temperature and Asymmetrical Coil Coupling," *Proceedings of 2018 IEEE International Conference on Power Electronics, Drives and Energy Systems, PEDES 2018*, pp. 1–5, 2018.

[41] Y. Tian, D. Li, J. Tian, and B. Xia, "A comparative study of state-of-charge estimation algorithms for lithium-ion batteries in wireless charging electric vehicles," *IEEE PELS Workshop on Emerging Technologies: Wireless Power, WoW 2016*, no. 2016, pp. 186–190, 2016.

[42] B. Wang, J. H. Fernandez, and A. Massoud, "A Wireless Battery Temperature Monitoring System for Electric Vehicle Charging," *Proceedings of IEEE Sensors*, vol. 2019-Octob, pp. 1–4, 2019.

[43] A. O. Elmeligy, E. Elghanam, M. S. Hassan, A. H. Osman, A. A. Shalaby, and M. Shaaban, "Optimal planning of dynamic wireless charging infrastructure for electric vehicles," *IEEE Access*, vol. 12, pp. 30 661–30 673, 2024.

[44] Y. Zhang, Y. Wu, Z. Shen, W. Pan, H. Wang, J. Dong, X. Mao, and X. Liu, "Integration of onboard charger and wireless charging system for electric vehicles with shared coupler, compensation, and rectifier," *IEEE Transactions on Industrial Electronics*, vol. 70, no. 7, pp. 7511–7514, 2023.

[45] S. Semsar, Z. Luo, S. Nie, and P. W. Lehn, "Integrated wireless charging receiver for electric vehicles with dual inverter drives," *IEEE Transactions on Power Electronics*, vol. 39, no. 1, pp. 1802–1814, 2024.

[46] H. Tu, H. Feng, S. Srdic, and S. Lukic, "Extreme fast charging of electric vehicles: A technology overview," *IEEE Transactions on Transportation Electrification*, vol. 5, no. 4, pp. 861–878, 2019.

[47] B. Singh and R. Kushwaha, "A pfc based ev battery charger using a bridgeless isolated sepic converter," *IEEE Transactions on Industry Applications*, vol. 56, no. 1, pp. 477–487, 2020.

[48] R. Shi, S. Semsar, and P. W. Lehn, "Constant current fast charging of electric vehicles via a dc grid using a dual-inverter drive," *IEEE Transactions on Industrial Electronics*, vol. 64, no. 9, pp. 6940–6949, 2017.

[49] D. Oulad-Abbou, S. Doubabi, A. Rachid, P. Garcia-Trivino, L. M. Fernandez-Ramirez, F. R. Carlos, A. Garcia-Vazquez, and R. Sarrias-Mena, "Combined control of MPPT, output voltage regulation and capacitors voltage balance for three-level DC/DC boost converter in PV- EV charging stations," *SPEEDAM 2018 - Proceedings: International Symposium on Power Electronics, Electrical Drives, Automation and Motion*, pp. 372–376, 2018.

[50] A. Safaeinasab, H. S. Gohari, and K. Abbaszadeh, "Design and Control of a Novel Multi-port Bidirectional Buck-Boost Converter Suitable for Hybrid Electric Vehicle Charging Stations," *2022 30th International Conference on Electrical Engineering, ICEE 2022*, pp. 1027–1032, 2022.

[51] J. Ma, Y. Deng, S. Wen, and M. Zhu, "Multimode Operation of Buck-Boost Converter for Building Block of DC Fast Charging Station," *Conference Record - IAS Annual Meeting (IEEE Industry Applications Society)*, vol. 2022-Octob, pp. 1–6, 2022.

[52] M. Nassary, E. Vidal-Idiarte, and J. Calvente, "Ac-dc four-switches boost buck converter for ev battery charging," in *2023 IEEE 17th International Conference on Compatibility, Power Electronics and Power Engineering (CPE-POWERENG)*, 2023, pp. 1–7.

[53] M. S. Khan, S. S. Nag, A. Das, and C. Yoon, "Analysis and control of an input-parallel output-series connected buck-boost dc-dc converter for electric vehicle powertrains," *IEEE Transactions on Transportation Electrification*, vol. 9, no. 2, pp. 2015–2025, 2023.

[54] R. Pradhan, N. Keshmiri, and A. Emadi, "On-board chargers for high-voltage electric vehicle powertrains: Future trends and challenges," *IEEE Open Journal of Power Electronics*, vol. 4, pp. 189–207, 2023.

[55] R. W. Erickson and D. Maksimovic, *Fundamentals of Power Electronics*, 2nd ed. Springer, 2012, vol. 1, pp. 501–524.

[56] N. Zanatta, T. Caldognetto, D. Biadene, G. Spiazzi, and P. Mattavelli, "Analysis and design of a partial-power post-regulator based dc/dc converter for automotive applications," in *2022 IEEE 13th International Symposium on Power Electronics for Distributed Generation Systems (PEDG)*, 2022, pp. 1–6.

[57] B. M. Conlon, "How Much Capability Do Electric Vehicles Need to Meet Customer Demands? [Viewpoint]," *IEEE Electrification Magazine*, vol. 5, no. 1, pp. 4–73, 2017.

[58] M. Yilmaz and P. T. Krein, "Review of battery charger topologies, charging power levels, and infrastructure for plug-in electric and hybrid vehicles," *IEEE Transactions on Power Electronics*, vol. 28, no. 5, pp. 2151–2169, 2013.

[59] A. Khaligh and M. Dantonio, "Global Trends in High-Power On-Board Chargers for Electric Vehicles," *IEEE Transactions on Vehicular Technology*, vol. 68, no. 4, pp. 3306–3324, 2019.

[60] H. Wouters and W. Martinez, "Bidirectional onboard chargers for electric vehicles: State-of-the-art and future trends," *IEEE Transactions on Power Electronics*, vol. 39, no. 1, pp. 693–716, 2024.

[61] O. Veneri, *Technologies and applications for smart charging of electric and plug-in hybrid vehicles*, 2016.

[62] M. Alamgir, "Lithium Has Transformed Vehicle Technology: How trends in Li-ion battery technology have developed for vehicle electrification," *IEEE Electrification Magazine*, vol. 5, no. 1, pp. 43–52, 2017.

[63] "BSI Standards Publication Electromagnetic compatibility (EMC)," 2019.

[64] D. Committee, I. Power, and E. Society, "IEEE 519 Recommended Practice and Requirements for Harmonic Control in Electric Power Systems IEEE Power and Energy Society," vol. 2014, 2014.

[65] A. Khaligh and S. Dusmez, "Comprehensive topological analysis of conductive and inductive charging solutions for plug-in electric vehicles," *IEEE Transactions on Vehicular Technology*, vol. 61, no. 8, pp. 3475–3489, 2012.

[66] K. Aditya and S. S. Williamson, "Design considerations for loosely coupled inductive power transfer (IPT) system for electric vehicle battery charging - A comprehensive review," *2014 IEEE Transportation Electrification Conference and Expo: Components, Systems, and Power Electronics - From Technology to Business and Public Policy, ITEC 2014*, pp. 0–5, 2014.

[67] K. Uddin, M. Dubarry, and M. B. Glick, "The viability of vehicle-to-grid operations from a battery technology and policy perspective," *Energy Policy*, vol. 113, no. August 2017, pp. 342–347, 2018. [Online]. Available: https://doi.org/10.1016/j.enpol.2017.11.015

[68] S. Semsar, T. Soong, and P. W. Lehn, "On-Board Single-Phase Integrated Electric Vehicle Charger with V2G Functionality," *IEEE Transactions on Power Electronics*, vol. 35, no. 11, pp. 12 072–12 084, 2020.

[69] C. Wei, J. Shao, B. Agrawal, D. Zhu, and H. Xie, "New surface mount SiC MOSFETs enable high efficiency high power density Bi-directional On-board charger with flexible DC-link voltage," *Conference Proceedings - IEEE Applied Power Electronics Conference and Exposition - APEC*, vol. 2019-March, pp. 1904–1909, 2019.

[70] S. Taghizadeh, M. J. Hossain, N. Poursafar, J. Lu, and G. Konstantinou, "A Multifunctional Single-Phase EV On-Board Charger with a New V2V Charging Assistance Capability," *IEEE Access*, vol. 8, pp. 116 812–116 823, 2020.

[71] J. Yuan, L. Dorn-Gomba, A. D. Callegaro, J. Reimers, and A. Emadi, "A review of bidirectional on-board chargers for electric vehicles," *IEEE Access*, vol. 9, pp. 51 501–51 518, 2021.

[72] H. Ouyang, K. Zhang, P. Zhang, Y. Kang, and J. Xiong, "Repetitive prediction of fluctuating DC link voltage for traction drives," *Diangong Jishu Xuebao/Transactions of China Electrotechnical Society*, vol. 26, no. 8, pp. 14–23, 2011.

[73] H. Zhao, Y. Shen, W. Ying, S. S. Ghosh, M. R. Ahmed, and T. Long, "A Single- And Three-Phase Grid Compatible Converter for Electric Vehicle On-Board Chargers," *IEEE Transactions on Power Electronics*, vol. 35, no. 7, pp. 7545–7562, 2020.

[74] X. Gong and J. Rangaraju, "Taking charge of electric vehicles both in the vehicle and on the grid," *Texas Instruments*, pp. 1–13, 2020. [Online]. Available: http://www.ti.com/lit/wp/szzy007/szzy007.pdf

[75] J. Lu, K. Bai, A. R. Taylor, G. Liu, A. Brown, P. M. Johnson, and M. McAmmond, "A Modular-Designed Three-Phase High-Efficiency High-Power-Density EV Battery Charger Using Dual/Triple-Phase-Shift Control," *IEEE Transactions on Power Electronics*, vol. 33, no. 9, pp. 8091–8100, 2018.

[76] Douglas Cesiel and Charles Zhu, "A Closer Look at the On Board Charger: The development of the second generation module for the Chevrolet Volt," *IEEE Electrification Magazine*, vol. 5, no. 1, pp. 36 – 42, 2017.

[77] H. Bai, M. McAmmond, J. Lu, Q. Tian, H. Teng, and A. Brown, "Design and Optimization of a 98%-Efficiency On-Board Level-2 Battery Charger Using E-Mode GaN HEMTs for Electric Vehicles," *SAE International Journal of Alternative Powertrains*, vol. 5, no. 1, pp. 205–213, 2016.

[78] X. Gong and S. E. M. Powertrain, "Designing 6 . 6kW Bidirectional HEV / EV On- Board-Charger with SiC and Embedded Technologies."

[79] G. Yang, R. Lindseth, and T. Sorsdahl, "Design of High Efficiency High Power Density 10 . 5kW Three Phase On-Board- Design of High Efficiency High Power Density 10 . 5kW Three Phase On-board-charger for Electric / hybrid Vehicles," no. October, pp. 10–12, 2018.

[80] H. Sarnago and O. Lucia, "High power density on-board charger featuring power pulsating buffer," *IEEE Open Journal of Power Electronics*, vol. 5, pp. 162–170, 2024.

[81] Jee Heon Kim, J. Y. Park, Joong Lee, Kyoung Choi, and Dong Jun Lee, "BIDIRECTIONAL POWERING ONBOARD CHARGER , VEHICLE POWER SUPPLY SYSTEM INCLUDING THE SAME , AND CONTROL METHOD THEREOF," 2018. [Online]. Available: https://patentimages.storage.googleapis.com/6a/9e/56/4a20a2df3d5fb0/US10046656.pdf

[82] J. Schmenger, S. Endres, S. Zeltner, and M. März, "A 22 kW on-board charger for automotive applications based on a modular design," *2014 IEEE Conference on Energy Conversion, CENCON 2014*, pp. 1–6, 2014.

[83] C. Jiang, B. Lei, H. Teng, and H. K. Bai, "The power-loss analysis and efficiency maximization of a silicon-carbide MOSFET based three-phase 10kW bi-directional EV charger using variable-DC-bus control," *ECCE 2016 - IEEE Energy Conversion Congress and Exposition, Proceedings*, vol. 2, no. c, pp. 1–6, 2016.

[84] P. M. Johnson and K. H. Bai, "A dual-DSP controlled SiC MOSFET based 96%-efficiency 20kW EV on-board battery charger using LLC resonance technology," *2017 IEEE Symposium Series on Computational Intelligence, SSCI 2017 - Proceedings*, vol. 2018-Janua, pp. 1–5, 2018.

[85] Y. Xiao, C. Liu, and F. Yu, "An Effective Charging-Torque Elimination Method for Six-Phase Integrated On-Board EV Chargers," *IEEE Transactions on Power Electronics*, vol. 35, no. 3, pp. 2776–2786, 2020.

[86] M. Y. Metwly, M. S. Abdel-Majeed, A. S. Abdel-Khalik, R. A. Hamdy, M. S. Hamad, and S. Ahmed, "A Review of Integrated On-Board EV Battery Chargers: Advanced Topologies, Recent Developments and Optimal Selection of FSCW Slot/Pole Combination," *IEEE Access*, vol. 8, pp. 85 216–85 242, 2020.

[87] A. G. Cocconi, "Combined motor drive and battery recharge system. US Patent 5,341,075," 1994.

[88] P. Pescetto, M. F. T. Cruz, F. Stella, and G. Pellegrino, "Galvanically isolated on-board charger fully integrated with 6-phase traction motor drives," *IEEE Access*, vol. 11, pp. 26 059–26 069, 2023.

[89] M. S. Diab, A. A. Elserougi, A. S. Abdel-Khalik, A. M. Massoud, and S. Ahmed, "A Nine-Switch-Converter-Based Integrated Motor Drive and Battery Charger System for EVs Using Symmetrical Six-Phase Machines," *IEEE Transactions on Industrial Electronics*, vol. 63, no. 9, pp. 5326–5335, 2016.

[90] I. Subotic, N. Bodo, E. Levi, and M. Jones, "Onboard Integrated Battery Charger for EVs Using an Asymmetrical Nine-Phase Machine," *IEEE Transactions on Industrial Electronics*, vol. 62, no. 5, pp. 3285–3295, 2015.

[91] I. Subotic, N. Bodo, E. Levi, M. Jones, and V. Levi, "Isolated chargers for EVs incorporating six-phase machines," *IEEE Transactions on Industrial Electronics*, vol. 63, no. 1, pp. 653–664, 2016.

[92] I. Subotic, N. Bodo, and E. Levi, "An EV Drive-Train with Integrated Fast Charging Capability," *IEEE Transactions on Power Electronics*, vol. 31, no. 2, pp. 1461–1471, 2016.

[93] L. De Sousa, B. Silvestre, and B. Bouchez, "A combined multiphase electric drive and fast battery charger for electric vehicles: Topology and electric propulsion efficency analysis," *2010 IEEE Vehicle Power and Propulsion Conference, VPPC 2010*, 2010.

[94] R. A. Taha, W. E. Abdel-Azim, A. Shawier, M. Y. Metwly, A. S. Abdel-Khalik, M. S. Hamad, R. A. Hamdy, S. Gadoue, and S. Ahmed, "Single-phase charging of six-phase integrated on-board battery charger using predictive current control," *IEEE Transactions on Transportation Electrification*, vol. 10, no. 1, pp. 540–552, 2024.

[95] M. S. Abdel-Majeed, A. Shawier, A. Habib, A. S. Abdel-Khalik, M. S. Hamad, S. Ahmed, and N. A. Elmalhy, "A three-phase nonisolated pseudo-six-phase-based integrated onboard battery charger for electric vehicles," *IEEE Transactions on Transportation Electrification*, vol. 9, no. 1, pp. 1300–1310, 2023.

[96] C. Viana and P. W. Lehn, "A Drivetrain Integrated DC Fast Charger with Buck and Boost Functionality and Simultaneous Drive/Charge Capability," *IEEE Transactions on Transportation Electrification*, vol. 5, no. 4, pp. 903–911, 2019.

[97] S. Afshar, P. Macedo, F. Mohamed, and V. Disfani, "Mobile charging stations for electric vehicles A review," *Renewable and Sustainable Energy Reviews*, vol. 152, no. July 2020, 2021.

[98] E. A. Kakillioglu, M. Yildiz Aktas, and N. FesciogluUnver, "Self controlling resource management model for electric vehicle fast charging stations with priority service," *Energy*, vol. 239, 2022.

[99] R. Buckreus, R. Aksu, M. Kisacikoglu, M. Yavuz, and B. Balasubramanian, "Optimization of Multiport DC Fast Charging Stations Operating with Power Cap Policy," *IEEE Transactions on Transportation Electrification*, vol. 7, no. 4, pp. 2402–2413, 2021.

[100] B. S. I. S. Publication, "BSI Standards Publication Electric vehicle conductive charging system Standard IEC 61851-1:2021," 2021.

[101] P. Flow, C. Parks, T. He, S. Member, J. Zhu, and S. Member, "Comparison Study of Electric Vehicles Charging Stations with AC and DC Buses for Bidirectional," pp. 4609–4614, 2007.

[102] J. E. Huber and J. W. Kolar, "Solid-State Transformers: On the Origins and Evolution of Key Concepts," *IEEE Industrial Electronics Magazine*, vol. 10, no. 3, pp. 19–28, 2016.

[103] X. She, A. Q. Huang, S. Lukic, and M. E. Baran, "On integration of solid-state transformer with zonal DC microgrid," *IEEE Transactions on Smart Grid*, vol. 3, no. 2, pp. 975–985, 2012.

[104] X. Yu, X. She, X. Zhou, and A. Q. Huang, "Power management for DC microgrid enabled by solid-state transformer," *IEEE Transactions on Smart Grid*, vol. 5, no. 2, pp. 954–965, 2014.

[105] J. S. Lai, W. H. Lai, S. R. Moon, L. Zhang, and A. Maitra, "A 15-kV class intelligent universal transformer for utility applications," *Conference Proceedings - IEEE Applied Power Electronics Conference and Exposition - APEC*, vol. 2016-May, pp. 1974–1981, 2016.

[106] S. Srdic, C. Zhang, X. Liang, W. Yu, and S. Lukic, "A SiC-based power converter module for medium-voltage fast charger for plug-in electric vehicles," *Conference Proceedings - IEEE Applied Power Electronics Conference and Exposition - APEC*, vol. 2016-May, pp. 2714–2719, 2016.

[107] M. Vasiladiotis and A. Rufer, "A Modular Multiport Power Electronic Transformer With Integrated Split Battery Energy Storage for Versatile Ultrafast EV Charging Stations," *IEEE Transactions on Industrial Electronics*, vol. 62, no. 5, pp. 3213–3222, 2015.

[108] D. Rothmund, G. Ortiz, and J. W. Kolar, "SiC-based unidirectional solid-state transformer concepts for directly interfacing 400V DC to medium-voltage AC distribution systems," *INTELEC, International Telecommunications Energy Conference (Proceedings)*, vol. 2014-Janua, no. January, 2014.

[109] L. Zheng, R. P. Kandula, and D. Divan, "Multiport control with partial power processing in solid-state transformer for pv, storage, and fast-charging electric vehicle integration," *IEEE Transactions on Power Electronics*, vol. 38, no. 2, pp. 2606–2616, 2023.

[110] D. Salomonsson, L. Söder, and A. Sannino, "Protection of low-voltage DC microgrids," *IEEE Transactions on Power Delivery*, vol. 24, no. 3, pp. 1045–1053, 2009.

[111] K. Menno, J. Schijfelen, M. Groninger, and V. Casteren, "BATTERY CHARGER FOR ELECTRIC VEHICLES Patent No US 10 , 166 , 873 B2 Date of Patent : Jan . 1 , 2019," 2019.

[112] J.-P. Krauer, "Charging Efficiency Using Variable Isolation Patent No Date of Patent: US 9.225,197 B2 Dec. 29, 2015," 2015.

[113] S. GÃ¶tz and V. Reber, "Modular power electronics system for charging an electrically operated vehicle," Patent US2018/0 162 229 A1, jun 14, 2018, [Online]. Available: https://patents.google.com/patent/US20180162229.

[114] K. HÃ¤hre, R. Heyne, M. Jankovic, and C. Metzger, "Power electronic module for a charging station and corresponding charging station and electricity charging station," Patent US2019/0 190 390 A1, dec 19, 2018, [Online]. Available: https://patents.google.com/patent/US20190190390A1.

[115] S. Gotz and V. Reber, "MODULAR POWER ELECTRONICS SYSTEM FOR CHARGING AN ELECTRICALLY OPERATED VEHICLE Pub . No US 2018 / 0162229 A1," 2018.

[116] K. Hahre, R. Heyne, M. Jankovic, and C. Metzger, "POWER ELECTRONIC MODULE FOR A CHARGING STATION AND CORRESPONDING CHARGING STATION AND ELECTRICITY CHARGING STATION Pub No US 2019 0190390 A1 United States Pub . Date Jun . 20 , 2019," vol. 1, 2019.

[117] F. Joslowski and L. E. De, "GALVANIC ISOLATION IN THE POWER ELECTRONICS SYSTEM IN A CHARGING STATION OR ELECTRICITY CHARGING STATION Patent No . US 10,759,293 B2 Date of Patent Sep. 1 , 2020," 2020.

[118] R. Venugopal, B. Chandrasekar, A. D. Savio, R. Narayanamoorthi, K. M. Aboras, H. Kotb, Y. Y. Ghadi, M. Shouran, and E. Elgamli, "Review on unidirectional non-isolated high gain dc-dc converters for ev sustainable dc fast charging applications," *IEEE Access*, vol. 11, pp. 78 299–78 338, 2023.

[119] H. Arya and M. Das, "Fast charging station for electric vehicles based on dc microgrid," *IEEE Journal of Emerging and Selected Topics in Industrial Electronics*, vol. 4, no. 4, pp. 1204–1212, 2023.

[120] C. Chou and P. A. Fortin, "LIQUID COOLED CHARGING CONNECTOR Pub . No . US 2019 0291588 A1 Pub . Date : Sep . 26 , 2019," 2019. [Online]. Available: https://patentimages.storage.googleapis.com/2b/df/63/270bc403168a11/US20190291588A1.pdf

[121] R. Button, "An advanced photovoltaic array regulator module," in *IECEC 96. Proceedings of the 31st Intersociety Energy Conversion Engineering Conference*, vol. 1, 1996, pp. 519–524 vol.1.

[122] N. MÃ¼ller, S. Kouro, P. Zanchetta, and P. Wheeler, "Bidirectional partial power converter interface for energy storage systems to provide peak shaving in grid-tied pv plants," in *2018 IEEE International Conference on Industrial Technology (ICIT)*, 2018, pp. 892–897.

[123] S. Muller, M. Deicke, and R. De Doncker, "Doubly fed induction generator systems for wind turbines," *IEEE Industry Applications Magazine*, vol. 8, no. 3, pp. 26–33, 2002.

[124] J. Anzola, I. Aizpuru, A. A. Romero, A. A. Loiti, R. Lopez-Erauskin, J. S. Artal-Sevil, and C. Bernal, "Review of Architectures Based on Partial Power Processing for DC-DC Applications," *IEEE Access*, vol. 8, pp. 103 405–103 418, 2020.

[125] S. Shenoy, "IMPROVING PERFORMANCE, EFFICIENCY, AND RELIABILITY OF DC-DC CONVERSION SYSTEMS BY DIFFERENTIAL POWER PROCESSING," Ph.D. dissertation, University of Illinois at Urbana-Champaign,, Champaign, IL, USA,, 2012.

[126] C. Olalla, D. Clement, M. Rodriguez, and D. Maksimovic, "Architectures and control of submodule integrated dc-dc converters for photovoltaic applications," *IEEE Transactions on Power Electronics*, vol. 28, no. 6, pp. 2980–2997, 2013.

[127] Y.-S. Lee and M.-W. Cheng, "Intelligent control battery equalization for series connected lithium-ion battery strings," *IEEE Transactions on Industrial Electronics*, vol. 52, no. 5, pp. 1297–1307, 2005.

[128] J. Zapata, "Partial power dc-dc converters for two stage photovoltaic energy conversion systems," Ph.D. dissertation, Universidad Tecnica Federico Santa Maria, 2018.

[129] J. R. R. Zientarski, M. L. Da Silva Martins, J. R. Pinheiro, and H. L. Hey, "Series-Connected Partial-Power Converters Applied to PV Systems: A Design Approach Based on Step-Up/Down Voltage Regulation Range," *IEEE Transactions on Power Electronics*, vol. 33, no. 9, pp. 7622–7633, 2018.

[130] E. Agheb and H. K. HÃ¸idalen, "Medium frequency high power transformers, state of art and challenges," in *2012 International Conference on Renewable Energy Research and Applications (ICRERA)*, 2012, pp. 1–6.

[131] E. L. Barrios, A. Urtasun, A. UrsÃºa, L. Marroyo, and P. Sanchis, "High-frequency power transformers with foil windings: Maximum interleaving and optimal design," *IEEE Transactions on Power Electronics*, vol. 30, no. 10, pp. 5712–5723, 2015.

[132] L. Zhou, M. Jahnes, M. Eull, W. Wang, and M. Preindl, "Control design of a 99% efficiency transformerless ev charger providing standardized grid services," *IEEE Transactions on Power Electronics*, vol. 37, no. 4, pp. 4022–4038, 2022.

[133] H. Song, R. Xu, S. Gao, Y. Wang, and D. Xu, "A high-frequency Dual Active Bridge Converter with Partial Power Processing," *PEAC 2022 - 2022 IEEE International Power Electronics and Application Conference and Exposition, Proceedings*, vol. 1, pp. 258–263, 2022.

[134] C. S. Beckmann, C. A. Rojas, H. Renaudineau, S. Kouro, H. Young, R. Opazo, and S. Rivera, "Comparison of Modulation Strategies for a Dual Active Bridge Partial Power DC-DC Converter in EV Powertrains," *IECON Proceedings (Industrial Electronics Conference)*, vol. 2022-Octob, no. c, pp. 3–8, 2022.

[135] H. Renaudineau, D. Pesantez, N. Muller, F. Flores-Bahamonde, S. Kouro, and J. Rodriguez, "Reconfigurable step-up/down partial power converter for pv power optimizer," in *2022 IEEE Energy Conversion Congress and Exposition (ECCE)*, 2022, pp. 1–6.

[136] B. Guo, X. Zhang, Z. Zhang, H. Ma, X. Jin, and Y. Wang, "Design of a 300 kw partial power processing based dc-dc converter for electric vehicles extreme fast charging stations," in *2022 IEEE International Power Electronics and Application Conference and Exposition (PEAC)*, 2022, pp. 423–428.

[137] J. Anzola, J. S. Artal-Sevil, I. Aizpuru, A. Arruti, R. Lopez, A. Alacano, and C. Bernal-Ruiz, "Resonant dual active bridge partial power converter for electric vehicle fast charging stations," in *2021 IEEE Vehicle Power and Propulsion Conference (VPPC)*, 2021, pp. 1–6.

[138] B. N. Alajmi, I. Abdelsalam, M. I. Marei, and N. A. Ahmed, "A three-phase interleaved ac-dc converter based electric-vehicle off-board battery charger station," in *2024 6th International Youth Conference on Radio Electronics, Electrical and Power Engineering (REEPE)*, 2024, pp. 1–5.

[139] S. B. Althurthi, K. Rajashekara, and T. Debnath, "A novel ultra-wide output range dc-dc converter for ev fast charging," *IEEE Journal of Emerging and Selected Topics in Industrial Electronics*, pp. 1–11, 2024.

[140] C.-W. Lin, H.-J. Chiu, M.-S. Tzeng, J.-W. Yeh, and C.-H. Huang, "Novel bidirectional on-board charger for g2v and v2x applications on wide-range batteries," *IEEE Journal of Emerging and Selected Topics in Power Electronics*, vol. 12, no. 2, pp. 2292–2305, 2024.

[141] H. Karneddi and D. Ronanki, "Analysis and design of a wide output voltage range battery charger for e-mobility applications," *IEEE Journal of Emerging and Selected Topics in Industrial Electronics*, pp. 1–10, 2024.

[142] B. O. Aarninkhof, D. Lyu, T. B. Soeiro, and P. Bauer, "A reconfigurable two-stage 11 kw dc-dc resonant converter for ev charging with a 150-1000 v output voltage range," *IEEE Transactions on Transportation Electrification*, vol. 10, no. 1, pp. 509–522, 2024.

[143] S.-T. Wu and Y.-W. Chiu, "Implementation of a bidirectional 400-800v wireless ev charging system," *IEEE Access*, vol. 12, pp. 26 667–26 682, 2024.

[144] A. Elezab, O. Zayed, A. Abuelnaga, and M. Narimani, "High efficiency llc resonant converter with wide output range of 200-1000 v for dc-connected evs ultra-fast charging stations," *IEEE Access*, vol. 11, pp. 33 037–33 048, 2023.

[145] W.-S. Lee, J.-H. Kim, J.-Y. Lee, and I.-O. Lee, "Design of an isolated dc/dc topology with high efficiency of over 97% for ev fast chargers," *IEEE Transactions on Vehicular Technology*, vol. 68, no. 12, pp. 11 725–11 737, 2019.

[146] R. V. Munoz, H. Renaudineau, S. Rivera, and S. Kouro, "Evaluation of dc-dc buck-boost partial power converters for ev fast charging application," in *IECON 2021 - 47th Annual Conference of the IEEE Industrial Electronics Society*, 2021, pp. 1–6.

[147] W. Shen, T. T. Vo, and A. Kapoor, "Charging algorithms of lithium-ion batteries: An overview," in *2012 7th IEEE Conference on Industrial Electronics and Applications (ICIEA)*, 2012, pp. 1567–1572.

[148] O. Tremblay and L. A. Dessaint, "Experimental validation of a battery dynamic model for EV applications," *World Electric Vehicle Journal*, vol. 3, no. 2, pp. 289–298, 2009.

[149] A. El Aroudi, B. G. M. Robert, A. Cid-Pastor, and L. Martinez-Salamero, "Modeling and design rules of a two-cell buck converter under a digital pwm controller," *IEEE Transactions on Power Electronics*, vol. 23, no. 2, pp. 859–870, 2008.

[150] Z. Liao, Y. Lei, and R. C. N. Pilawa-Podgurski, "Analysis and design of a high power density flying-capacitor multilevel boost converter for high step-up conversion," *IEEE Transactions on Power Electronics*, vol. 34, no. 5, pp. 4087–4099, 2019.